THE UNIVERSITY *of* EDINBURGH

First Nuclear Reaction Measurements using the CARME array

Jordan Marsh

Doctor of Philosophy
University of Edinburgh
2023

Abstract

The broad outline of nucleosynthesis is well established; however, our understanding of it is not yet complete. In many cases, advances in astronomical observations have placed the burden of further understanding on an improved understanding of key nuclear physics processes. High precision nuclear physics measurements are required to reduce the uncertainty of these processes which significantly influence a range of astrophysical scenarios. These measurements can be extremely challenging to perform using current methodologies and require new experimental techniques. Storage rings provide one such methodology by performing nuclear reaction studies using stored heavy ion beams on an ultra-thin internal gas-jet target. My PhD project is devoted the installation and commissioning of the CRYRING Array for Reaction Measurements (CARME), which utilises this novel methodology and will aim to address many of the outstanding problems requiring improved nuclear physics inputs.

In this thesis the methodology of using storage rings for nuclear reaction studies is presented in addition to details of the CARME array and its commissioning. The commissioning process includes the extensive vacuum commissioning required for storage ring operations, in addition to the data analysis procedures developed to determine nuclear parameters from an experiment. The first experimental run using the CARME array used a deuteron beam on a nitrogen target at beam energies of 1.5 and 5.5 MeV/u. Several states from the ^{14}N(d, p)^{15}N and ^{14}N(d, α)^{12}C reactions were identified, and the cross sections of these states have been compared to previous measurements. DWBA calculations have been performed to model the angular distribution of the ^{14}N(d, p$_5$)^{15}N reaction, and the spectroscopic factor has been extracted. This spectroscopic factor is in agreement with the spectroscopic factors reported in previous experimental measurements and theoretical calculations.

Lay Summary

Nuclear reactions provide the energy which power many of the phenomena we observe in the cosmos, and are the mechanism by which many of the elements in the Universe are produced. Understanding these reactions can give us insight into the inner workings of stellar phenomena, in addition to how and where the elements we are made of are synthesised. Nuclear reactions are studied on Earth, often at accelerator facilities where intense ion beams are fired at targets to recreate the reactions that occur in stellar sites. These studies have yielded a great understanding of nucleosynthesis in the Universe but many open questions remain. Answering these questions requires further investigation of various nuclear reactions key to certain stellar phenomena, many of which are very difficult to perform using conventional methodologies. This work is focused on the commissioning of a new experimental setup (CARME) using a novel methodology for performing nuclear reaction studies. This methodology involves circulating an ion beam around a storage ring at several hundred thousand revolutions per second. Ions in the beam interact with an extremely thin gas target each revolution, with reaction products detected by silicon detectors. This methodology has the potential to answer many of the open questions in nuclear astrophysics, which cannot be answered using more conventional techniques.

In this thesis, the first experimental measurement using CARME is presented. Details of the experimental procedures are given and the results obtained are compared to previous studies in order to validate the system. Our results are consistent with previous experimental measurements and provide a launching point for the future scientific programme using CARME.

Declaration

I declare that this thesis was composed by myself, that the work contained herein is my own except where explicitly stated otherwise in the text, and that the work has not been submitted for any other degree or professional qualification except as specified.

Parts of this work has been published in [1]

C.G. Bruno, **J.J.Marsh** *et al*, Nuclear Instruments and Methods in Physics Research Section A: Accelerators, Spectrometers, Detectors and Associated Equipment, 1048 (2023)

Acknowledgements

This thesis was completed with the help and support of many people. First I would like to thank my supervisor Carlo Bruno for his guidance during my studies, and making my experience, especially the many trips away from home much more enjoyable. I would also like to thank Phil Woods for his help and guidance throughout my PhD, Tom Davinson, for his expert knowledge in addition to always keeping me well fed with crispy duck, and Peter Black for making work in the lab more amusing and teaching me many skills such as how to sew fibreglass blankets. I also thank all the staff and students in the Edinburgh Nuclear physics group.

I thank Michael Lestinsky, Davide Racano, Oemer Guelsever, Nikos Petridis, Jan Glorius, Yuri Litvinov, Thomas Stoehlker, Angela Braeuning-Demain and the rest of the GSI atomic physics group who have been of invaluable help and guidance during the commissioning and installation of CARME, in addition to Keith Middleman, Paul Hindley, Alex Headspith and Katherine Clarke from the vacuum group at Daresbury laboratory for their support in all things vacuum.

Finally I thank all my friends and family who have supported me during the last few years. In particular, I thank my parents for their constant support, Alex who has read too many drafts of this thesis and lil Ralph, who this thesis is dedicated to.

List of Figures

Contents

Chapter 1

Nuclear Physics, Astrophysics and Experimental Approaches

1.1 Introduction

Nuclear physics processes are one of the driving forces of the stellar evolution in the Universe and the mechanism by which the elements are synthesised. One of the main aims of nuclear astrophysics is the study of these nuclear processes in order to determine the origin of the elements and understand the observed abundances of those elements in the Universe today. The broad outline of nucleosynthesis is well established. The light elements up to lithium were produced during the first few minutes of the Universe following the Big Bang [2]. Elements heavier than lithium are primarily produced in stellar environments, either during the quiescent burning stages within stars or during explosive stellar events [3]. Figure 1.1 shows the stellar production method of the chemical elements in the periodic table according to nucleosynthesis models. The nucleosynthesis pathway is a complex web of competing processes and our understanding of it is not yet complete. Improvement of nucleosynthesis models requires both high precision observations of stellar phenomena and experimental measurements of key nuclear reactions. These key reactions are identified by sensitivity studies which perform nucleosynthesis calculations to determine the main reaction uncertainties governing the production of nuclei in stellar environments. In certain cases, the presence of these nuclei in stellar environments can be observed, either through their decay producing observable gamma-rays or through pre-solar grains found on Earth,

and are useful probes of stellar phenomena. These probes can be crucial to improve stellar models, but high precision reaction measurements are often required to reduce uncertainties. These measurements can be extremely challenging to perform and may require new methodologies. Examples of key probes for core collapse supernova and novae explosions, and the required nuclear physics uncertainties which could be reduced using CARME are presented in the next section.

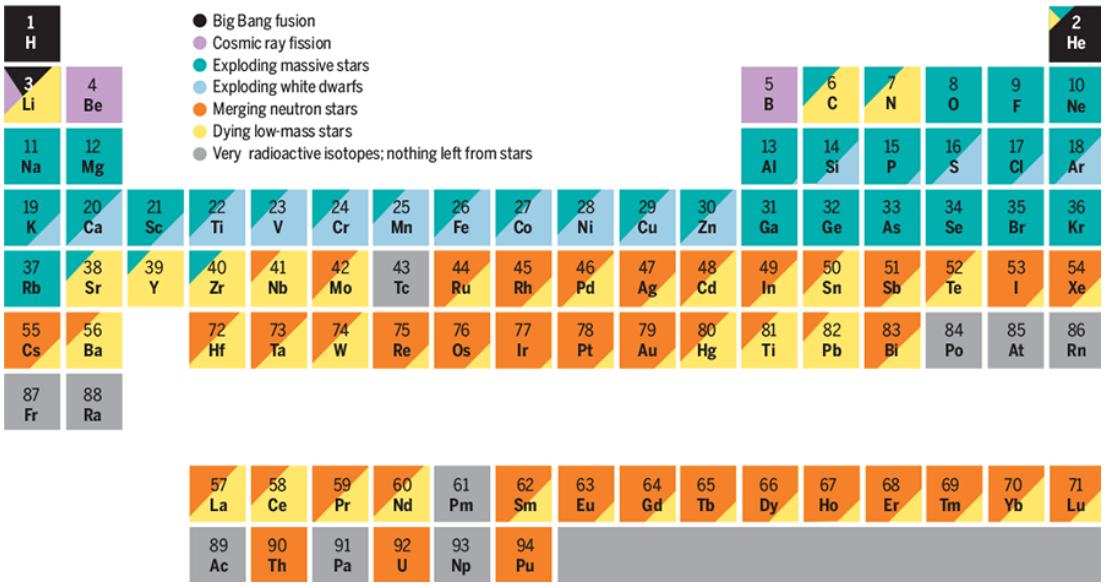

Figure 1.1: Periodic table of the elements in the Solar System. The color of the elements in the table relates to their stellar production method. Multiple production methods are denoted by fractional colors. [4]

1.2 Outstanding nuclear problems

1.2.1 Core collapse supernova

Core collapse supernova (CCSNe) are the explosive end of the life of massive stars ($>8M_{\odot}$) and are key drivers of the enrichment of heavy elements in galaxies. CCSNe are triggered by the gravitational collapse of the star as the outward radiation pressure from fusion reactions in the core is no longer sufficient to prevent collapse [5]. The outer layers of the star fall inwards until the collapse is abruptly halted at the inner core, generating a rebounding shock wave [5]. The initial shock wave is not thought to be sufficient to power the explosion, with its energy dissipated through the photo-disintegration of nuclei in the outer core and large neutrino losses. The large neutrino flux is thought to revive the stalled shock front powering the explosion [5, 6]. This

neutrino flux from CCSNe has been observed in SN1987A [7, 8], but the exact physics of the neutrino interactions which revive the shock front remain uncertain. A review of the current theory of CCSNe and the recent theoretical advances made through simulations is given in reference [6].

The amount of material ejected into the interstellar medium from CCSNe for nuclei synthesised in regions close to the core is dependent on the explosion mechanism. ^{44}Ti is an unstable isotope produced close to the core which makes it an ideal probe of the CCSNe explosion mechanism. The gamma rays from the decay of ^{44}Ti have been detected in the ejecta of the Cassiopeia A [9–11] and SN1987A [12, 13] supernova. The mass of ^{44}Ti in ejecta from these measurements is above the maximum mass predicted by CCSNe models [14, 15]. The difference between the observed and predicted mass of ^{44}Ti in ejecta could be due to deficiencies in explosion models or due to uncertainties in the production or destruction of ^{44}Ti by nuclear reactions. Sensitivity studies have demonstrated that the production of ^{44}Ti is influenced by a handful of key reactions, with the ^{44}Ti(α, p)^{47}V reaction highlighted as the most significant [15, 16].

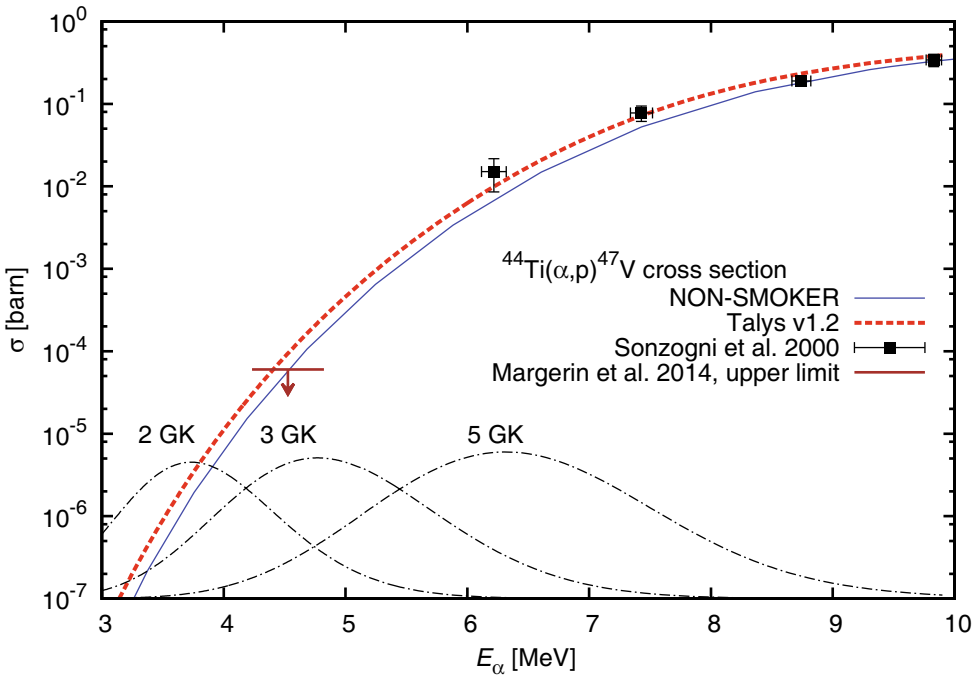

Figure 1.2: Current status of the ^{44}Ti(α, p)^{47}V reaction. Data points represent the measured cross section which are fitted with the NON-SMOKER and TALYS codes. The data point by Margerin *et al* [17] represents an upper limit on the cross section. The Gamow peaks for supernova of different temperatures is shown at the bottom of the plot. More data is required at these lower energies. [18]

The current state of the reaction cross section and the relevant energies for CCSNe is shown in figure 1.2. Two measurements of the ^{44}Ti(α, p)^{47}V reaction have been performed [17, 19]. Only an upper limit on the cross section has so far been determined at energies within the 3 GK Gamow peak [17]. The main difficulty in probing the low energies relevant for CCSNe is in producing sufficiently intense ^{44}Ti beams. A measurement of this reaction in CARME would aim to probe energies at ∼1.5 MeV/u and below, which is just below the peak of the 5 GK Gamow window.

1.2.2 Novae

Novae are recurrent explosions occurring in binary systems, where hydrogen-rich material is accreted onto the surface of a white dwarf from a less evolved companion star. The large gravitational forces on the surface of the white dwarf heat and compress the accreted material, which is under degenerate conditions so that it cannot expand to relieve pressure [20]. The material is further heated by nuclear reactions, initially through the pp chain and then through the CNO and hot CNO cycles. Sufficient temperatures are eventually reached to allow the material to expand and the explosion occurs. The white dwarf remains intact following the explosion, which allows for recurrent novae events. Nucleosynthesis of heavy nuclei is driven by successive proton capture reactions. Mixing between the underlying white dwarf material and the accreted material enhances the hydrogen burning cycles. This provides the required energy and seed nuclei for synthesis to heavier isotopes. The exact mechanism for mixing is not known and several methods have been suggested [21]. The nucleosynthesis pathway is sensitive to the explosion and mixing mechanism, providing a possible probe of novae parameters [22]. More accurate nuclear physics inputs are required in order to make use of nucleosynthesis as a probe of novae.

Pre-solar grains that originate from novae may provide a useful probe of the explosion [22, 23]. Silicon isotopes are of particular interest for O-Ne novae. The large excess of silicon compared with solar abundances can be used to identify grains of nova origin, and different silicon isotopes could potentially be used to deduce the white dwarf mass and peak nova temperature [22]. The Si/H abundance has also been suggested as a promising probe of the mixing of the accreted and white dwarf material [21]. The uncertainty in the ^{30}P(p, γ)^{31}S reaction has been identified as the main uncertainty in the synthesis of silicon isotopes and intermediate isotopes up to calcium [24, 25].

The effect of the uncertainty of the reaction cross section on the production of different isotopes in the mass range 20-40 is shown in figure 1.3 [25].

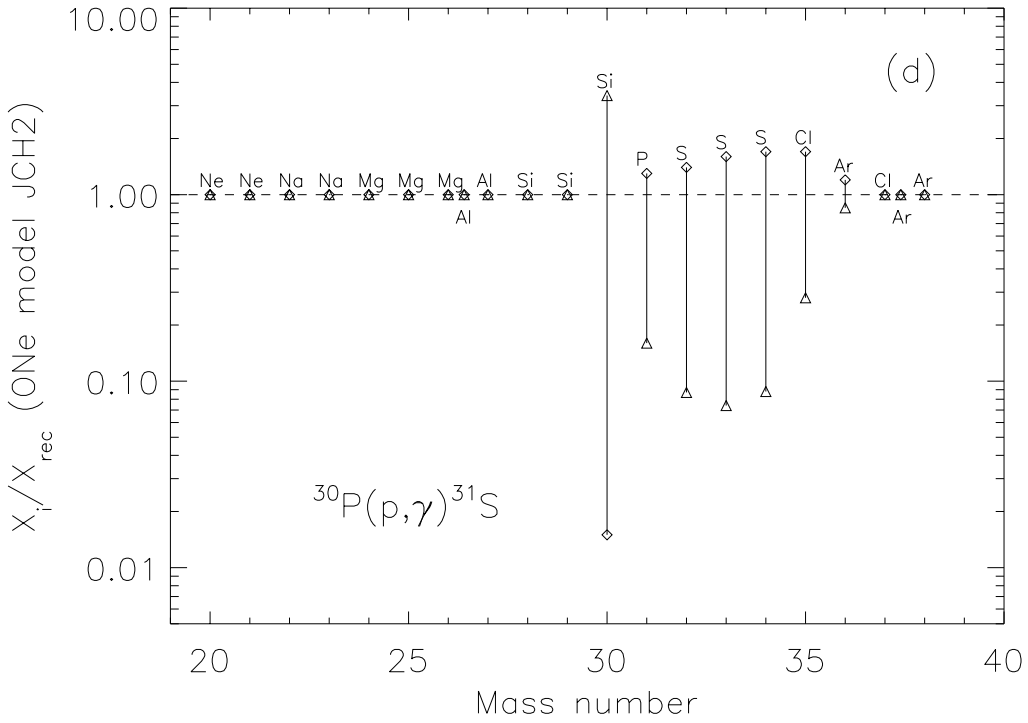

Figure 1.3: Plot of the fractional change in the abundance of isotopes in the mass range 20-40 produced by nova models from varying the ^{30}P(p, γ)^{31}S up or down by present uncertainties (factor 100). Taken from reference [25].

To determine the total reaction rate for the ^{30}P(p, γ)^{31}S reaction, accurate knowledge of individual resonances in the Gamow window are required. Uncertainties arise from a lack of knowledge in the properties of states in the ^{31}S compound nucleus. Direct measurements at the energies relevant for novae have not been possible so far due to insufficient beam intensities. Indirect studies have been utilised to populate excited states in the ^{31}S nucleus or in its stable mirror ^{31}P [26–34]. A summary of the levels in ^{31}S from these experimental measurements is given in reference [33]. In the 0.1-0.17 GK temperature range, the reaction rate is dominated by a resonance state with an excitation energy of 6327 keV, which is reasonably well constrained [31]. The main area of interest is now in resonance states influencing the 0.2-0.4 GK temperature range. The assignment of states in this region is uncertain. Discrepancies exist between different experimental measurements and also between measurements and shell model calculations [35, 36]. One example is the prediction of a 1/2- excited state in ^{31}S by shell model calculations in the energy range of interest for nova burning that has yet

been observed by experimental measurements [33]. The most significant resonance in this temperature regime is the 3/2+ state with an excitation energy of 6390 keV, which is situated in the middle of the Gamow peak [37]. The strength of this state has recently been determined in a study of the beta delayed proton decay of ^{31}Cl [34]. However, the uncertainty on this strength is large. The main uncertainty in the strength of this state is now from the Γ_γ of the level in the ^{31}S compound nucleus which is currently adopted from theoretical calculations [34]. A future measurement using CARME would perform the ^{30}P(d, p)^{31}P reaction in order to identify and measure the analogue states in the ^{31}P mirror nucleus to those of significance in ^{31}S. In particular, measurement of the analogue states of the 6390 keV resonance and the missing 1/2- excited state in ^{31}S would be the primary aims of such a study.

Annihilation gamma-rays resulting from the β^+ decay of ^{18}F are expected to be a powerful probe of nova explosions [38, 39]. The destruction of ^{18}F through the ^{18}F(p, α)^{15}O reaction is currently the dominant uncertainty in the production of ^{18}F in novae [40]. This uncertainty will influence the interpretation of any potential future gamma-ray observations and has been of long standing interest to the nuclear astrophysics community. The reaction rate uncertainty at low nova temperatures (< 0.5 GK), is dominated by the resonances of sub-threshold states with excitation energies of 6132 and 6289 keV in the ^{19}Ne compound nucleus [40]. These resonant states are not isolated, and the interference between the $l = 0$ resonant states contributes significantly to the current uncertainty [40]. Properties of these states such as the spin parity assignment and state widths is required to reduce the uncertainty on the reaction rate. Figure 1.4 shows the S-factor for different spin-parity assignments of these states with the energy regions of interest for novae in the top left of the plot [41]. Direct measurements [42–45] have been unable to reduce the uncertainty at low energies, where the S-factor can vary by an order of magnitude, primarily due to insufficient ^{18}F beam intensities. Indirect studies of the compound nucleus using transfer reactions [41, 46, 47] and resonant scattering [48, 49] have been performed. However, contradictory spin-parity assignments have been suggested and it is suggested there may be unobserved/misaligned states in both ^{19}Ne and its mirror ^{19}F [47]. A key aim for future studies would be to identify the spin-parity of the sub-threshold states and their widths, relevant for the interference between states. In CARME this would be achieved by performing a high resolution measurement of the resonant nuclear excitation function in inverse kinematics. The

resonant scattering of ^{15}O on a helium target could potentially be achieved with an excitation energy resolution of $\sim$ 1 keV FWHM. This could potentially be sufficient to deduce the parameters of states in ^{19}Ne relevant for nova explosions.

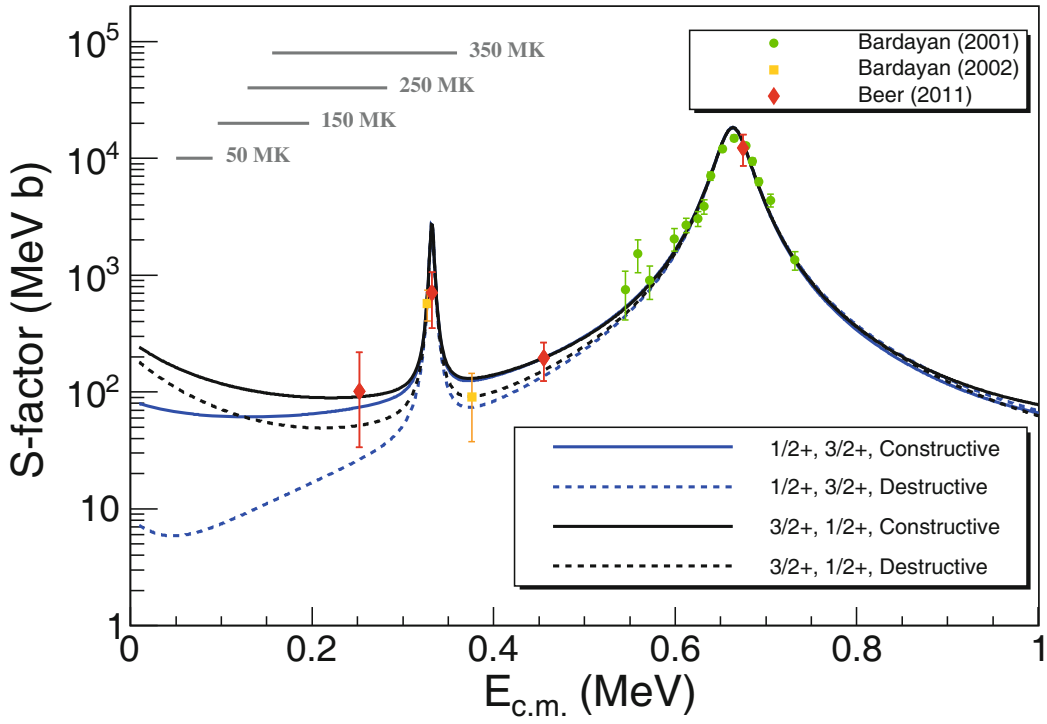

Figure 1.4: Plot of the astrophysical S-factor (defined in the next section) for the ^{18}F(p, α)^{15}O reaction calculated with different spin and interference assumptions. The first spin represents the 6.132 MeV state and the second spin represents the 6.289 MeV state. Data points show the S-factor determined from direct measurements. The energy range of different Gamow peaks is shown in the top left of the plot. [41]

1.3 Nuclear reactions in the laboratory

1.3.1 Reaction cross section

Nuclear reactions are drivers of nucleosynthesis and are the mechanism of energy generation within stars. These reactions are typically studied in the laboratory on Earth by accelerating a beam onto a target. A schematic of a reaction between an incident particle (a) and a target particle (A), in the laboratory frame, which results in the emission of light (b) and heavy (B) reaction products, written as a + A $\rightarrow$ b + B, is shown in figure 1.5. The energy released by the reaction is given by the Q-value

$$Q = (M_{\mathrm{a}} + M_{\mathrm{A}} - M_{\mathrm{b}} - M_{\mathrm{B}})\, c^2 \tag{1.1}$$

where M is the mass of each particle and c is the speed of light. If any excited states are produced, the excitation energy must be subtracted from the Q-value [50]. The probability of a reaction occurring when the two particles interact at the relevant stellar energies is a key parameter for determining the reaction rate. This probability is described by the cross section σ, which is given by

$$\sigma = \frac{N_{\mathrm{R}}}{N_{\mathrm{T}} N_{\mathrm{B}}} \tag{1.2}$$

where $\mathrm{N_R}$ is the number of reactions resulting from the interaction per second, $\mathrm{N_B}$ is the number of beam particles incident on the target per second, and $\mathrm{N_T}$ is the number of target nuclei per unit area. The cross section is usually expressed in units of barns (1 barn = 10^{-24} cm^2) and is dependent on the energy of the interacting nuclei in the centre of mass frame. The energy dependence of the cross section can be parameterised by introducing the astrophysical S-factor [3].

$$\sigma(E) = \frac{1}{E}\, e^{-2\pi\eta}\, S(E) \tag{1.3}$$

where E is the energy of the reaction in the centre of mass frame, $e^{-2\pi\eta}$ is the Gamow factor which represents the transmission probability through the Coulomb barrier, η is the Sommerfield parameter [3] and S(E) is the astrophysical S-factor. In the case of non-resonant reactions, the removal of the energy dependence from the Coulomb

barrier penetration results in an S-factor which varies smoothly with energy. In many cases resonances exist, which results in an S-factor which can vary by orders of magnitude over a small energy range. In stellar environments, resonances, particularly those close to the Gamow peak [3], can dominate the total reaction rate making the study of resonances crucial for experimental measurements. The reaction rate for narrow, isolated resonances is dependent on the resonance energy E_r and the resonance strength $\omega\gamma$. The resonance strength can be defined by [51]

$$\omega\gamma = \frac{(2J_r + 1)}{(2J_1 + 1)(2J_2 + 1)} \frac{\Gamma_1 \Gamma_2}{\Gamma} \tag{1.4}$$

where J_r is the spin of the resonance, $J_{1,2}$ are spins of the target and projectile, $\Gamma_{1,2}$ are the partial widths through the channels 1 and 2, and Γ is the total width of the resonance. The partial widths of a state can be obtained from the single particle width of the state Γ_{sp}, which is the width of a pure single particle resonance at the same resonance energy described by the shell model [51]

$$\Gamma_a = C^2 S \, \Gamma_{sp} \tag{1.5}$$

where C is the Clebsch-Gordon co-efficient and S is the spectroscopic factor. In the remainder of this work C^2S is referred to as the spectroscopic factor.

1.3.2 Transfer reactions

Transfer reactions are a useful probe of states which can be used to determine parameters such as the spin-parity and partial width of the state. Direct transfer reactions are a one step process between the initial and final states [52]. The angular distributions of direct reactions have distinct shapes based on the orbital angular momentum transferred ℓ in the reaction, which can give insight into the spin parity of the final state. The angular distribution of a single particle state can be modelled using Distorted Born Wave Approximation (DWBA) theory [52]. The spectroscopic factor can be extracted by comparing the experimental and DWBA cross sections.

$$\left(\frac{d\sigma}{d\Omega}\right)_{EXP} = C^2 S \left(\frac{d\sigma}{d\Omega}\right)_{DWBA} \tag{1.6}$$

The differential cross section $\left(\frac{d\sigma}{d\Omega}\right)$ is used to examine the angular dependence of the cross section, and is given by

$$\frac{d\sigma}{d\Omega} = \frac{N_{\mathrm{d}}}{N_{\mathrm{B}} N_{\mathrm{T}} \eta d\Omega} \tag{1.7}$$

where $\mathrm{N_d}$ is the number of detected particles across a solid angle coverage of $\mathrm{d}\Omega$ and η is the intrinsic detection efficiency. In many cases, the reaction is not direct, with the formation of a compound nucleus as an intermediate step. Both the compound nucleus and direct mechanisms can contribute to the cross section ($\sigma_{total} = \sigma_{direct} + \sigma_{compound}$). Reactions dominated by the compound nucleus mechanism produce largely flat angular distributions in the centre of mass frame and are modelled using statistical Hauser-Feshbach theory [52].

1.3.3 Reaction kinematics

In the laboratory, a reaction can proceed either using a light projectile, usually protons, deuterons or alpha particles, incident upon a heavier nucleus (normal kinematics) or the reverse with a heavy projectile and lighter target (inverse kinematics). Studies involving radioactive isotope beams (RIBs) are usually conducted in inverse kinematics as the radioactive isotope is often heavier than the target nuclei. The laboratory energy of the light and heavy reaction products emitted at laboratory angles θ and ϕ respectively (see figure 1.5) are given by the following relations, assuming all particles in the interaction have mass [50].

$$E_{\mathrm{b}} = E_{\mathrm{T}} B \left(cos\theta \pm \left(\frac{D}{B} - sin^2\theta \right)^{1/2} \right)^2 \tag{1.8}$$

$$E_{\mathrm{B}} = E_{\mathrm{T}} A \left(cos\varphi \pm \left(\frac{C}{A} - sin^2\varphi \right)^{1/2} \right)^2 \tag{1.9}$$

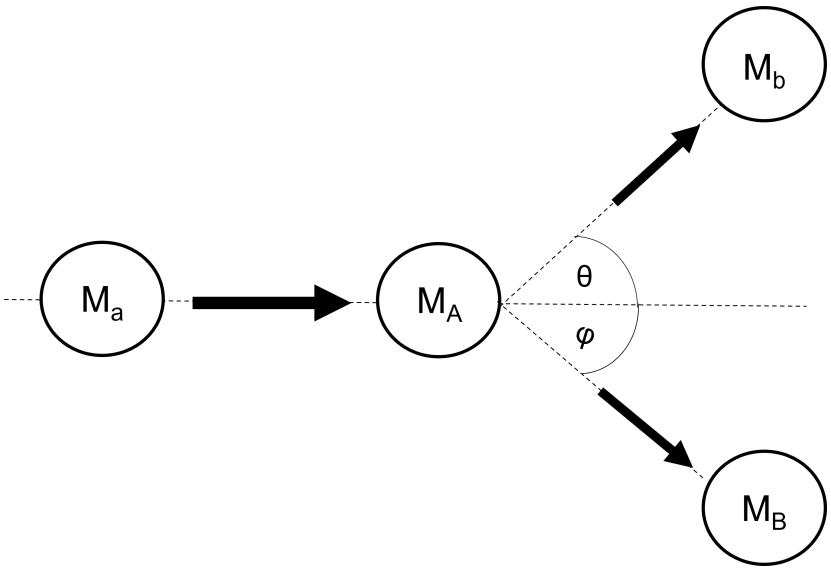

Figure 1.5: Kinematic schematic of the reaction A(a,b)B in the laboratory frame where (a) represents the projectile, (A) the target, (b) the light ejectile and (B) the heavy recoil. The angles θ and φ correspond to the laboratory angles for the light ejectile and heavy recoil reaction products respectively.

E_a is the laboratory energy of the projectile, E_T is the sum of E_a and the Q-value, and the variables A,B,C,D are dimensionless variables which sum to unity. The variables A,B,C,D are given by the following relations.

$$A = \frac{M_a M_B (E_a/E_T)}{(M_a + M_A)(M_b + M_B)} \tag{1.10}$$

$$B = \frac{M_a M_b (E_a/E_T)}{(M_a + M_A)(M_b + M_B)} \tag{1.11}$$

$$C = \frac{M_A M_b}{(M_a + M_A)(M_b + M_B)} \left[1 + \frac{M_a Q}{M_A E_T}\right] \tag{1.12}$$

$$D = \frac{M_A M_B}{(M_a + M_A)(M_b + M_B)} \left[1 + \frac{M_a Q}{M_A E_T}\right] \tag{1.13}$$

Only the positive sign in equations 1.8 and 1.9 are used unless B>D or A>C, in which case the maximum emission angle is given by

$$\theta_{\max} = \sin^{-1}(D/B)^{1/2} \quad \text{and} \quad \varphi_{\max} = \sin^{-1}(C/A)^{1/2} \tag{1.14}$$

In general, if the reaction is exothermic (Q>0) and in normal kinematics, the energy of both the reaction products will have only one value for the energy at each angle in the laboratory frame. If Q< 0, or the reaction occurs in inverse kinematics, the emission of the heavy reaction product can be forward peaked with a maximum emission angle $< 90°$, and have two values for the energy at each angle. As an example, the difference between normal and inverse kinematics for the ^{15}N particles emitted from the ^{14}N(d,p)^{15}N reaction at a centre of mass energy of 0.38 MeV is shown in figure 1.6.

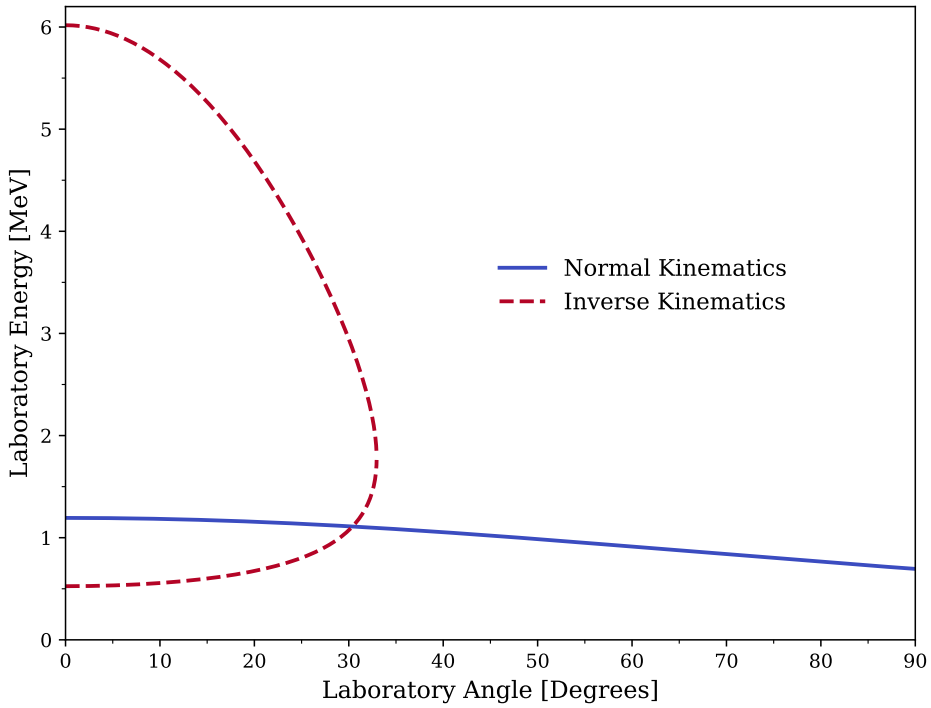

Figure 1.6: Kinematic plots for the ^{15}N recoils emitted from the ^{14}N(d,p)^{15}N reaction in normal kinematics (blue) and inverse kinematics (red). Both plots are for a centre of mass energy of 0.38 MeV. The Q-value is +8.61 MeV. The ^{15}N recoils are emitted across 180 degrees in the lab frame in normal kinematics, however their emission is forward peaked with a maximum emission angle of $\sim$ 35 degrees in inverse kinematics.

Chapter 2

Nuclear Reactions Studies using Heavy-Ion Storage Rings

2.1 A novel methodology for nuclear reaction studies

Heavy-ion storage rings are facilities where ion beams can be stored in a closed loop for long periods of time and present a novel methodology for performing nuclear reaction measurements. Nuclear reaction measurements using storage rings have the potential to overcome some of the difficulties of more conventional methodologies and resolve long standing problems in nuclear astrophysics. This methodology also presents several major challenges. One of the main challenges for performing storage ring measurements is the extreme high vacuum (XHV) conditions ($\sim 10^{-12}$ mbar), which is required to minimise interactions between the stored beam ions and any residual gas particles inside the ring in order to maximise the storage time. This chapter describes the key aspects of nuclear reaction measurements using storage rings including the advantages and challenges of this methodology.

2.2 Storage rings

2.2.1 GSI Helmholtz centre for heavy ion research

The GSI Helmholtz Centre for Heavy Ion Research is a leading accelerator facility located in Darmstadt, Germany. GSI is unique worldwide in the availability to utilise two heavy ion storage rings, of different ion energy ranges, with radioactive beams produced via in flight fragmentation for nuclear reaction measurements. The relevant devices for nuclear reaction measurements at GSI include the UNILAC linear accelerator, SIS18 ring accelerator, FRS fragment separator, and the two heavy ion storage rings, the Experimental Storage Ring (ESR), and the CRYRING. The pathway of ions through each of these devices, starting at the ion source and finishing in the CRYRING is shown in figure 2.1.

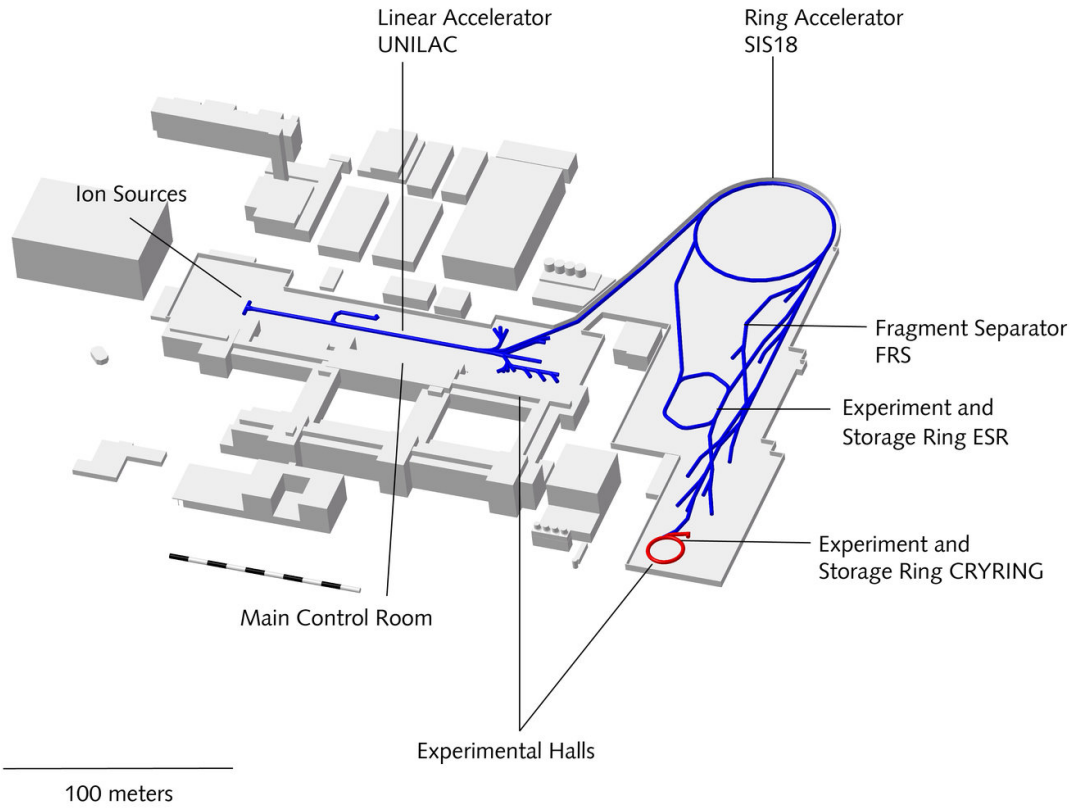

Figure 2.1: The GSI facility with the the pathway of ions throughout the facility, from the initial ion source to injection into the CRYRING, highlighted in blue. The CRYRING is shown in red. [53]

2.2.2 The ESR and CRYRING storage rings

The ESR storage ring is a hexagonal ring with a total path length of 108.4 metres that can store ions from helium to uranium at energies from several MeV/u to the GeV/u level [54]. A schematic of the ESR with key components labelled is shown in figure 2.2. The ESR features a 2 metre long electron cooler which, coupled with stochastic cooling, can reduce the emittance of stored beams to $\sim 0.1\ \pi$ mrad and the momentum spread to $\Delta p/p \sim 10^{-5}$ [54]. Following cooling, the beam diameter is typically less than 5 mm. The ESR also features an internal gas-jet target, that is utilised for atomic physics experiments and more recently for nuclear reaction measurements. One of the key aspects of the ESR is its deceleration capability, with ion energies able to be reduced by several orders of magnitude in a very short timescale. The typical time required to decelerate ions from 400 MeV/u to 3 MeV/u in the ESR, including the cooling time, is $\sim$ 30 s [55].

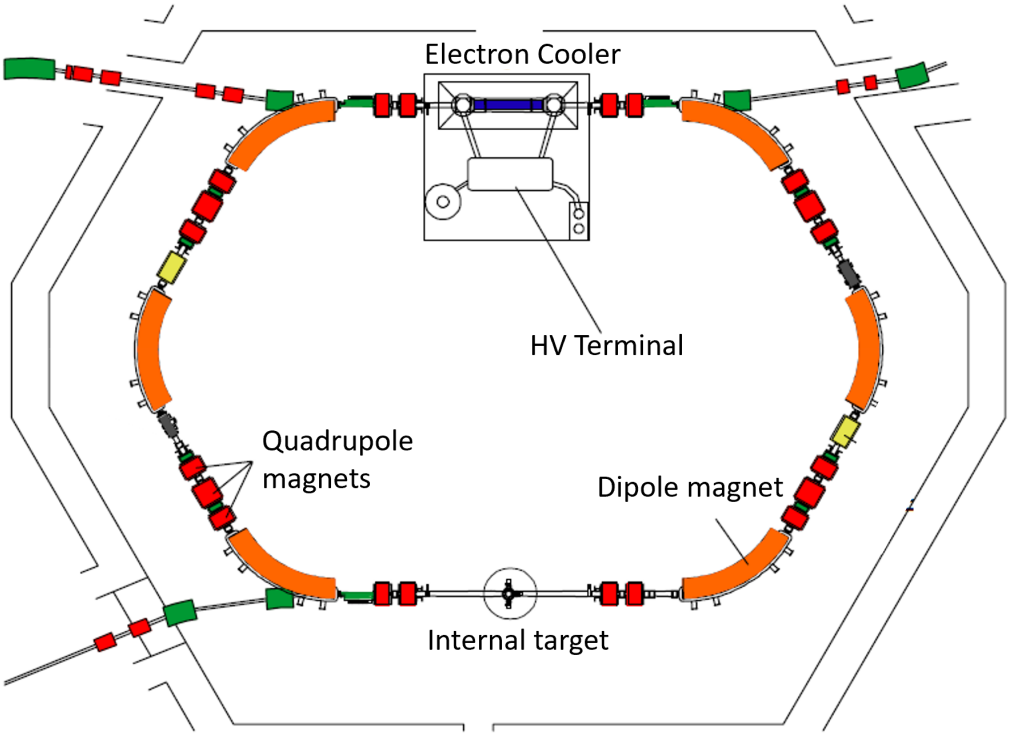

Figure 2.2: The ESR storage ring located at the GSI facility. Key components such as the gas-jet target and electron cooler are labelled. Adapted from from reference [54].

The CRYRING storage ring was originally installed and operated at the Manne-Siegbahn laboratory in Stockholm Sweden before its move to GSI to form part of FAIR phase-0. The CRYRING is a circular ring consisting of 12 straight sections with a circumference of 54.2 metres, half that of the ESR. A schematic of the CRYRING with key components labelled is shown in figure 2.3. The CRYRING is optimised for ion energies from approximately 14 MeV/u down to $\sim$ 100 keV/u, complementary to energies available in the ESR allowing for the transfer of ions between the two rings. The minimum energy ions can be stored within CRYRING is limited by the storage lifetime of the beam.

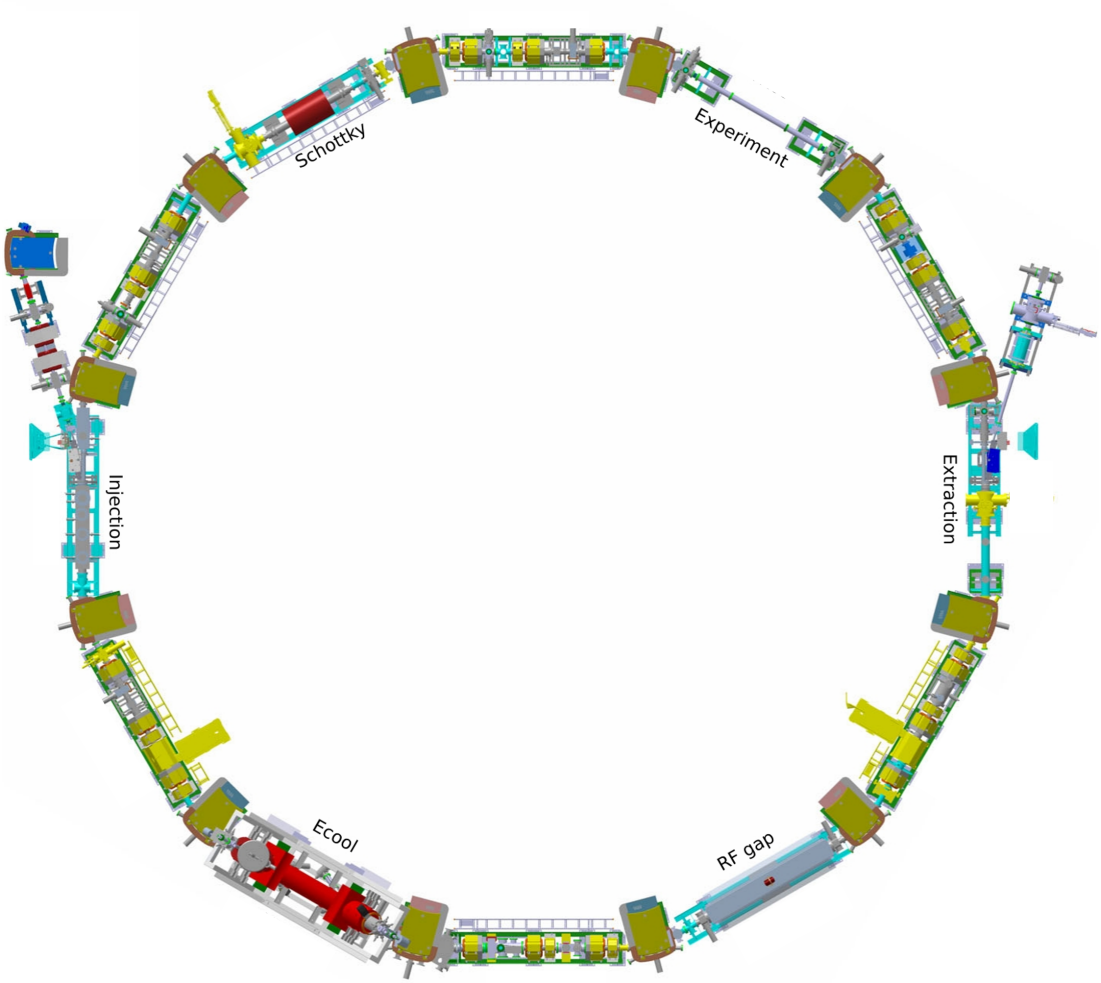

Figure 2.3: The CRYRING storage ring located at the GSI facility. CARME and the gas-jet target are installed in the experimental section (top right). Key components such as the injection section and electron cooler are labelled. Adapted from [56]

2.3 Experimental aspects

2.3.1 Nuclear reaction measurement at the CRYRING - key steps

Nuclear reaction studies can be performed at the CRYRING using ions injected into the ring from a local ion source or by injection of (radioactive) ions from the ESR. Radioactive isotopes are produced via fragmentation by impinging ions, accelerated in the SIS18, onto a thin target. These isotopes are then separated in the FRS before injection into the ESR. The beam is then decelerated and cooled before injection into the CRYRING. This pathway of radioactive ions from production in-flight to injection into the CRYRING is shown in figure 2.4. The deceleration and transfer of ions between rings is not 100% efficient with beam intensity losses incurred at each stage. The beam intensity can be increased by the continual injection and accumulation of ions within the ring before a measurement is performed in a process called stacking [57]. Stacking can be utilised in the ESR, during an ongoing measurement in the CRYRING, to increase the number of ions available to be injected into the CRYRING.

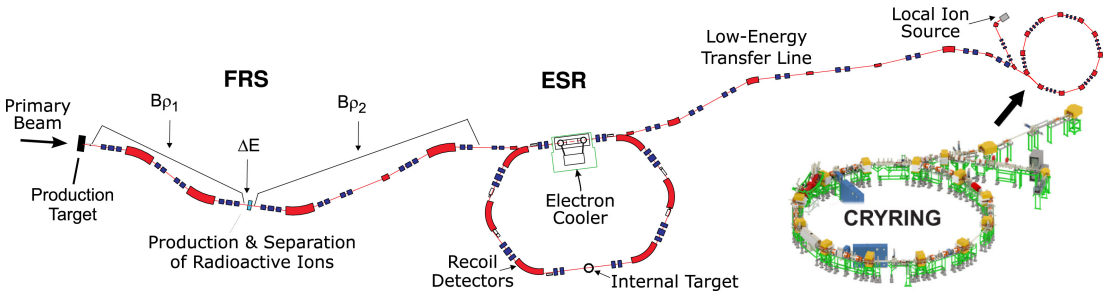

Figure 2.4: A detailed pathway of a radioactive ion beam from production of radioactive ions in-flight to injection into the CRYRING. Key components of the FRS and ESR are labelled. [55]

When the beam is injected into the ring it typically has a large emittance. Beam emittance is the volume in phase space occupied by particles in the beam. The longitudinal emittance refers to the momentum spread and the transverse emittance refers to the position and angular spread [58]. The longitudinal and transverse emittance are reduced by electron cooling of the beam (see section 2.3.3). The electron cooler also maintains the beam at a constant energy and emittance, compensating for any intra-beam interactions or interactions of ions with the gas-jet target. Ions are circulated within the CRYRING at a frequency of several hundred kHz and are incident on a windowless, ultra-thin (10^{11}-10^{14} particles/cm^2) gas jet target. The target is required to be ultra-thin as any interactions (both nuclear and non-nuclear processes) between

the beam ions and the target lead to a loss of beam ions over time. The loss of ions from the beam over time reduces the luminosity. When the luminosity has decreased to a certain threshold, it is more efficient to dump the beam from the ring and re-inject at the initial beam intensity. The characteristic time scale before re-injection is required is known as the beam lifetime (see section 2.3.2), however higher luminosities may be achievable by maintaining the beam in the ring for shorter or longer periods of time. Nuclear reaction products are measured by silicon detectors in the CARME array, which is detailed in chapter 3.

2.3.2 Beam lifetime

One of the main limiting factors for reaction studies in storage rings is the amount of time that ions can be stored in the ring. The beam lifetime refers to the characteristic timescale ions in the beam can circulate around the ring before they are lost due to interactions with either residual gas molecules remaining within the ring or with molecules within the internal gas target. The main interactions which cause beam losses within the ring are multiple and single Coulomb scattering, and charge exchange interactions such as electron capture and electron stripping. To reduce the probability of an interaction, extreme high vacuum (XHV) conditions must be maintained in the ring. When there is no internal target, the beam lifetime is determined by interactions with residual gas molecules. The partial beam lifetime from interactions with residual gas molecules t_{rg} is given by [57, 59]

$$t_{rg}^{-1} = \sigma\rho\beta c \tag{2.1}$$

where σ is the relevant interaction cross section, ρ is the density of residual gas molecules [particles/cm^3], and $\beta = v/\mathrm{c}$, where v is the ion velocity and c is the speed of light. When the internal target is on, interactions with the target typically become the dominant source of beam losses. The partial beam lifetime from interactions with atoms in the target t_{tar} is given by

$$t_{tar}^{-1} = \sigma n_{\mathrm{t}} f_0 \tag{2.2}$$

where n_t is the target thickness [atoms/cm^2] and f_0 is the revolution frequency. A balance between a higher target density to maintain the nuclear reaction rate and a lower target density to maintain the storage lifetime is required.

Interactions between the ion beam and electrons in the electron cooler, such as radiative and dielectronic recombination also cause beam losses. The lifetime associated with radiative recombination in the electron cooler t_{ec} is given by [57]

$$t_{ec}^{-1} = n_e \left(\frac{C}{l_{eff}} \right) \alpha_{rec} \tag{2.3}$$

where n_e is the cooler electron density, C is the circumference of the ring, l_{eff} is the effective length of the cooler and α_{rec} is the recombination coefficient which is defined in reference [57].

The total beam lifetime from all interactions in the ring can then be expressed as [59]

$$t = \left(t_{rg}^{-1} + t_{tar}^{-1} + t_{ec}^{-1} \right)^{-1} \tag{2.4}$$

Interactions

The beam lifetime is a key parameter for low energy nuclear reaction measurements and is dependent on the cross section of the specific interaction in question. The interaction cross section is typically dependent on the projectile energy and the charge of the target and beam ions. At the low energies of interest for nuclear reaction studies on the CRYRING ($\sim$ MeV), electron capture is typically the dominant beam loss mechanism. Electron capture is the capture of an electron onto an ion in the beam, changing its charge state such that it is lost from the beam. An electron capture cross section from a universal scaling rule for all ions was determined for the reduced energy range $10 < \tilde{E} < 1000$ keV by Schlachter *et al* [60]. The reduced energy is described by the relation $\tilde{E} = E \,/\, (Z_{gas}^{1.25}\, q^{0.7})$ where E is the projectile energy per nucleon (keV/u), Z_{gas} is the atomic number of the gas target and q is the charge state of the projectile. The best fit to the data was given by

$$\sigma_{EC} = \frac{1.1 \times 10^{-8}}{\tilde{E}^{4.8}} \left[1 - \exp\left(-0.037 \tilde{E}^{2.2} \right) \right] \left[1 - \exp\left(-2.44 \times 10^{-5} \tilde{E}^{2.6} \right) \right] \tag{2.5}$$

At the higher range of reduced energies considered by Schlachter, the cross section asymptotically approaches the relation

$$\sigma_{\mathrm{EC}} = 1.1 \times 10^{-8} \frac{q^{3.9}\, Z_{gas}^{4.2}}{E^{4.8}} \tag{2.6}$$

For the majority of nuclear reaction measurements to be performed in the CRYRING, the reduced energy is such that the cross section in equation 2.6 can be used. The electron capture cross section has a large dependence on the atomic number of the gas the ion interacts with. In the case of interactions with a gas target, the gas species is well known. In the case of an interaction with residual gases in the ring, many different molecules may be present. How the cross section is calculated for a residual gas and for molecules with a mix of elements is covered in reference [59]. Typical beam lifetimes from target and residual gas contributions for electron capture are calculated at various energies in table 2.1. The target density used for calculations is $1{\times}10^{11}$ atoms/cm^2. The beam lifetime from residual gas interactions is determined using the CRYRING calculator which assumes a pressure of $5{\times}10^{-11}$ mbar and typical residual gas constituents. The effect of the pressure on the beam lifetime in the CRYRING can be visualised in figure 1 of the CARME technical paper [1].

Projectile	Target	Beam Energy [MeV/u]	Target Lifetime [s]	Residual Gas Lifetime [s]
$^{30}P^{15+}$	^{2}H	8.0	180000	2800
$^{2}H^{+}$	^{14}N	1.5	1442	1500
$^{2}H^{+}$	^{1}H	0.2	884	80
$^{15}O^{8+}$	^{4}He	1.0	15	80
$^{44}Ti^{22+}$	^{4}He	1.5	1.6	20
$^{6}Li^{3+}$	^{1}H	0.1	0.62	6

Table 2.1: Calculated values for the beam lifetime of different beam and target combinations at different energies. The beam lifetime from interactions with the target is calculated considering electron capture interactions. The target thickness used for all calculations is $1{\times}10^{11}$ atoms/cm^2. The beam lifetime from residual gas interactions is calculated using the CRYRING calculator, which assumes a residual gas pressure of $\sim 5{\times}10^{-11}$ mbar

Other interactions which can contribute to beam losses include electron stripping and Coulomb scattering. Electron stripping is the second charge exchange mechanism, in which an electron is lost from a partially stripped ion. To avoid these losses and reduce the effect of electron screening on the cross section [61], the majority of nuclear reaction studies at the CRYRING will utilise fully stripped ions. The electron stripping contribution to the beam lifetime is therefore not considered further in this work. Multiple and single Coulomb scattering cause beam losses by scattering ions outside of the momentum range (acceptance) that ions can be kept circulating by the magnets in the ring. Multiple Coulomb scattering, either between beam ions or between beam ions and molecules in the target increases the emittance of the beam over time. If the emittance grows larger than the acceptance of the ring, ions are lost from the beam. Single Coulomb scattering events deflect ions by large angles. If the ions are deflected by an angle above the maximum acceptance angle for the ring, the ion is lost from the beam. The electron cooler maintains the beam emittance (see section 2.3.3) and at low energies ($\sim$ MeV) the beam lifetime is dominated by electron capture so that the Coulomb scattering processes are not considered further here. Full equations for the interaction cross sections for all beam loss interactions and a good comparison between the beam lifetime expected from Coulomb scattering and electron capture processes is given in reference [57].

2.3.3 Electron cooling

Electron cooling is the reduction in the emittance of an ion beam via collisions with a mono-energetic electron beam. The electron beam is merged with the ion beam at an equal velocity to the average velocity of the ion beam. Ions in the beam undergo Coulomb interactions with the electrons transferring momentum to them. The electron beam is constantly renewed so that the ion beam temperature (velocity spread) tends to the electron beam temperature over time. Figure 2.5 shows the interaction of the ion beam (red) with a cold mono-energetic electron beam (blue). The physical size of the beam and the momentum spread are reduced by electron cooling. An example of the reduction in the beam width following electron cooling at the TSR storage ring is shown in figure 2.6 [57]. The momentum spread in the ESR and CRYRING following electron cooling is of the order of $\Delta p/p \approx 10^{-5}$ [56, 62]. Due to the small size of the target, the reduction in the beam width increases the percentage of ions in the beam

which can interact with the target. This has the effect of increasing the luminosity of the measurement. Electron cooling reduces the phase space occupied by the beam [63], which is required to inject further ions into the beam during the stacking procedure.

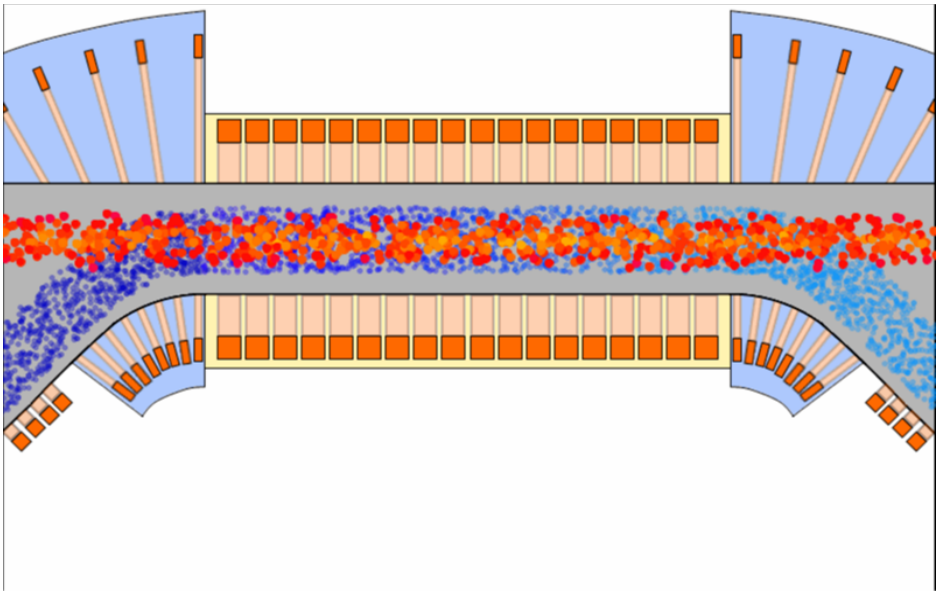

Figure 2.5: Image of the basic principle of an electron cooler. A 'hot' ion beam (red) is cooled by a 'cold' electron beam (blue) running parallel with the ion beam. The electron beam is constantly renewed so that the ion beam temperature tends towards the electron beam temperature. Figure taken from reference [64]

The beam emittance reduces over time with a cooling rate λ [55, 57, 63]. The inverse of this rate is the cooling time which is proportional to

$$\tau_C \propto \frac{1}{\eta n_e} \frac{A}{q^2} \tag{2.7}$$

where A is the atomic mass number, q is the charge state of the ion, n_e is the electron density and η is the ratio of the cooler length to the circumference of the ring. A complete description of electron cooling and definition can be found in reference [63]. In reference [63] a calculation for the cooling time for a proton beam using 'standard cooler parameters' is detailed. Inserting the CRYRING electron cooler length and ring circumference, for a proton energy of 1 MeV, the cooling time is estimated to be approximately 2 seconds.

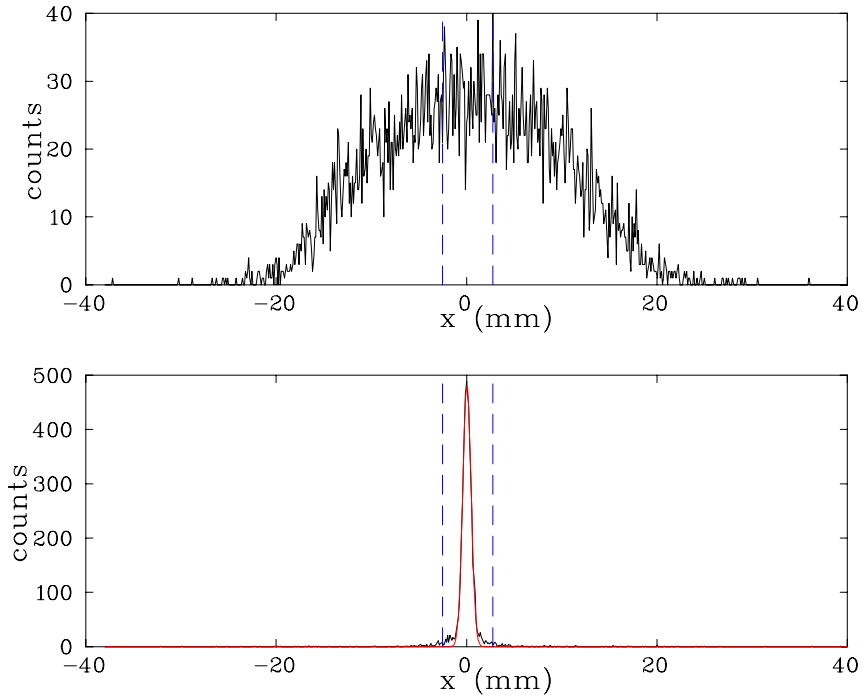

Figure 2.6: Profile of injected and cooled beam at the TSR storage ring. The blue dotted line refers to the 'cooled region' which encompasses the region -6σ_{cool} to +6σ_{cool}. The time difference between beam profiles is approximately 2 seconds [57]

2.3.4 Achieving XHV vacuum

To reduce beam losses from interactions with residual gases, pressures in the 10^{-12} mbar regime must be maintained across the ring. The process of evacuating a vacuum chamber installed on the ring to the XHV regime follows three main stages which are shown in figure 2.7. In the first stage, gases that occupy the chamber volume are removed. Gas molecules, either adsorbed onto internal chamber surfaces or absorbed and diffused into the chamber walls, remain. These molecules are released from the surface over time in a process called out-gassing. The second and third stages involve the removal of these molecules as they out-gas over time. Pressure reductions in each successive stage take incrementally longer and are more difficult to achieve. In the XHV regime, the ultimate pressure achievable can be approximated as [65]

$$P \approx \frac{Q}{S} \tag{2.8}$$

where P is the pressure in the chamber [mbar], Q is the outgassing rate [mbar l s^{-1}] and S is the pumping speed [l s^{-1}] of the vacuum pumps.

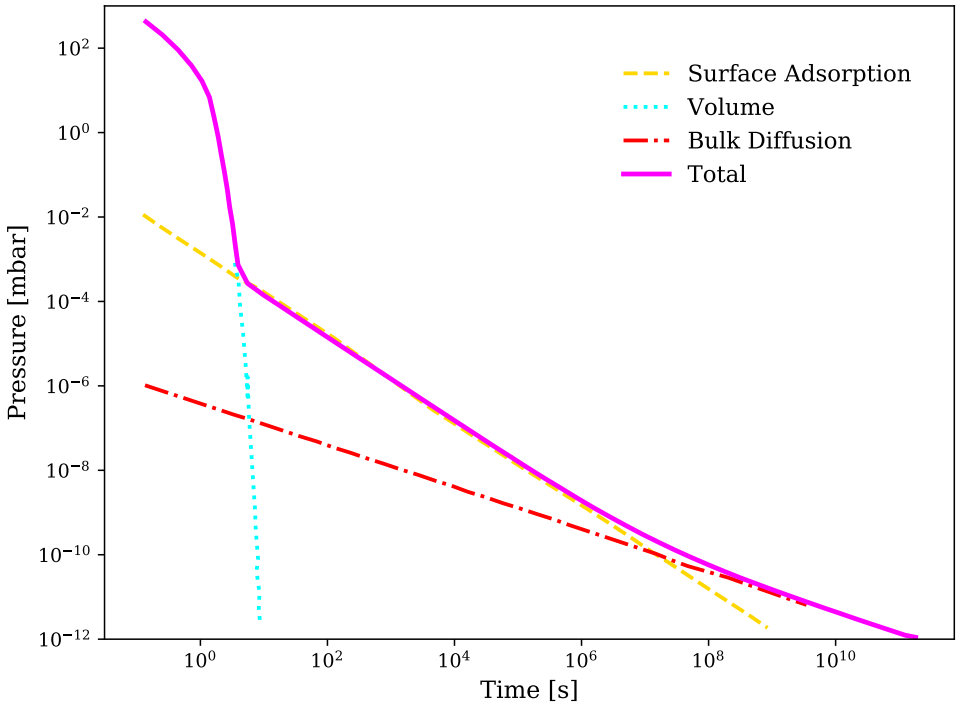

Figure 2.7: A typical pump-down plot for an XHV vacuum chamber. The different sources of pressure within the chamber are labelled with the total pressure in magenta. Initial stages of the pump-down (volume) reduce the pressure by orders of magnitude in a short amount of time. In subsequent stages (surface adsorption and bulk diffusion) the reduction in pressure over time is much slower. Modified plot to that in reference [65]

The lowest vacuum pressure is attained when the out-gassing rate is minimised and the pumping speed on the chamber is maximised. The pumping speed can be increased by increasing the size and number of vacuum pumping systems on the chamber. However, limited space and the expensive cost of XHV vacuum pumps limits the number of systems that can be installed. As a result, the pumping speed can generally only be increased by a maximum of three orders of magnitude ($\sim 10^{1}$-10^{4} l/s). The out-gassing rate can vary over a greater range of up to 10 orders of magnitude ($\sim 10^{-4}$-10^{-14} mbar l/s) depending on the materials and the treatment of those materials when placed under vacuum [65]. Therefore, to achieve XHV, it is more beneficial to focus time and resources on reducing the out-gassing load than additional vacuum pumps.

Initial Pumping Stage

The first stage of the pump-down is achieved by a combination of roughing pumps and turbo-molecular pumps. A roughing pump reduces the pressure to approximately 10^{-2} mbar. For XHV applications a scroll pump is used because of its lack of hydrocarbon back-streaming into the vacuum. A scroll pump consists of two spirals called 'scrolls', one fixed in place and one able to move eccentrically against the other. Gas enters the open end of the scrolls, is compressed and forced into the centre of the scrolls by the movements of the non-fixed scroll. When it reaches the centre, the gas is expelled from the pump by a valve. Due to the nature of its operation, scroll pumps only work at higher pressures in the viscous gas flow regime. In the viscous gas flow regime the gas behaves as a single continuum with many collisions between molecules [66]. Below 10^{-2} mbar, collisions between gas molecules are infrequent, with the motion of molecules independent of other molecules in the chamber (molecular flow regime) [66]. Turbo-molecular pumps operate in the molecular flow regime and are made up of several stages of fast rotating angled blades. Individual molecules collide with the fast rotating blades of the pump, which transfers momentum to the molecules in the preferred direction out of the chamber. In XHV applications magnetically suspended rotors are preferred to traditional ball bearings, to reduce the possibility of vacuum contamination produced by the mechanical wear of the bearings.

Adsorption

In the molecular flow regime, the pressure in the chamber is dependent on the outgassing of molecules adsorbed to surfaces within the chamber. When molecules collide with a surface, they can stick to and become bound to the surface [66, 67]. Molecules can be bound to chamber surfaces either by Van der Waals dipole forces (physisorption), or by chemical bonding (chemisorption) [65, 66]. Surface desorption is the process where molecules bound to surfaces are released under vacuum, and contribute to the chamber pressure. If the kinetic energy of the bound molecule is greater than the binding energy to the surface it can escape. The number of particles that meet this criterion is given by the Boltzmann expression such that the surface-desorption flux is given as [66]

$$j = \frac{dn}{dt} = v_0 n \exp\left(-\frac{\mathrm{E}}{\mathrm{RT}}\right) \tag{2.9}$$

where n is the number of adsorbed molecules per square centimeter, T is the temperature [Kelvin], E is the binding energy [J/mol], R is the molar gas constant, and v_0 is the oscillation frequency of bound molecules. Once released from the surface, the molecule can be removed from the chamber by the turbo pump or can undergo multiple collisions with chamber surfaces in which there is a possibility of re-adsorption. The mean time a molecule remains in the chamber and can contribute to the vacuum level, considering re-adsorption, is given by [68]

$$\tau = \frac{1}{v_0} \exp\left(\frac{\mathrm{E}}{\mathrm{RT}}\right)\left(1 + \frac{v}{4}\frac{\mathrm{s}}{\mathrm{S/A}}\right) \tag{2.10}$$

where S is the pumping speed, A is the internal chamber surface area, v is the average molecular velocity and s is the probability of a molecule sticking to the surface upon collision. The sticking probability tends to increase at lower pressures as more sites are free for molecules to bind to [68]. The outgassing rate can be modelled as the sum of the out-gassing rates of molecules of different binding energies which reduces over time following the relation

$$\mathrm{Q} = \sum_{i=1}^{n} \frac{\mathrm{Q}_{i,0}}{\tau_i} \tag{2.11}$$

where $\mathrm{Q_{i,0}}$ (initial out-gassing rate) and τ_i are for molecules with specific binding energies. Figure 2.8 shows the total out-gassing rate over time and the contribution of molecules with different binding energies at room temperature. Molecules with binding energies below 70 kJ/mol have a mean residence time in the chamber of < 1 hour, so do not contribute to the long term out-gassing rate in the chamber. The outgassing rate of molecules with binding energies >100 kJ/mol is so low that they also have a negligible effect on the total out-gassing rate. Molecules with binding energies between these two limits contribute significantly to the chamber pressure over long time scales. Water molecules typically bind to chamber surfaces with energies between 80 and 105 kJ/mol [66], and represent the main out-gassing load within vacuum systems. In figure 2.8 molecules with binding energies up to 105 kJ/mol require $>10^7$ seconds (100 days) to

remove from the chamber. This timescale is not practical and the pressure must be reduced much more rapidly. The rate of outgassing has an exponential dependency upon the temperature, which can be used to significantly reduce the number of molecules within the chamber. Temporarily increasing the temperature of the chamber, in a process called baking, increases the out-gassing rate so that the majority of surface adsorbed molecules are removed from the chamber.

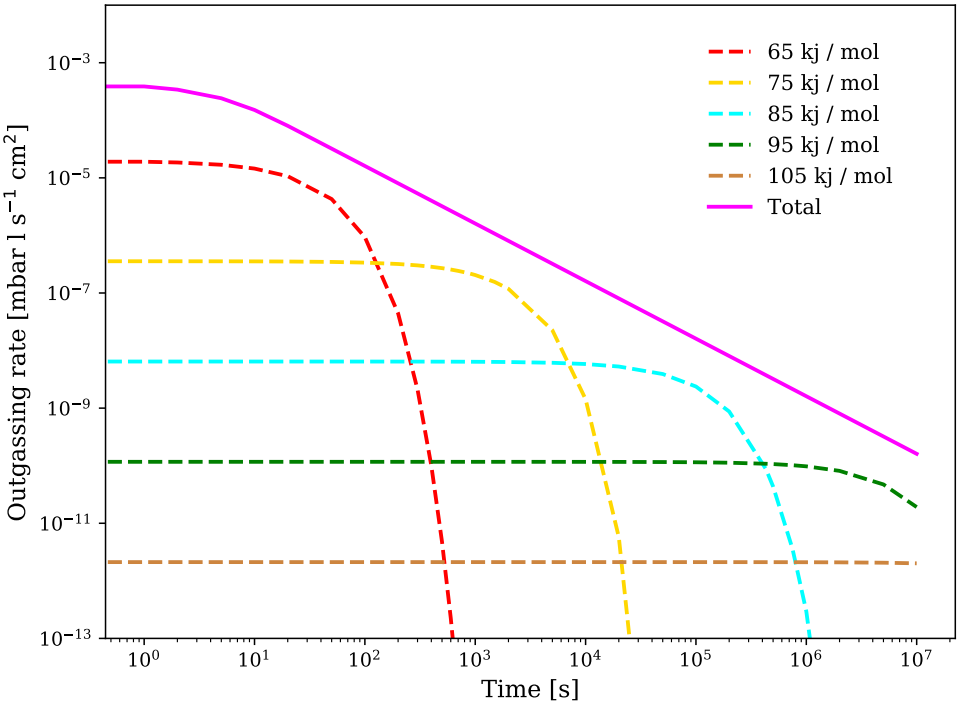

Figure 2.8: Plot of outgassing rates for water molecules of desorption energies ranging from 60-120 kJ/mol at room temperature (300 K). The CARME chamber internal surface area of 2.9 m^2 and turbo pump pumping speed of 300 l/s are used. The sticking probability is assumed to be constant and is equal to 0.1, an estimate based on probabilities stated in reference [68].

When the temperature is reduced back to room temperature, the out-gassing rate is significantly reduced. The baking procedures used to achieve XHV conditions with the CARME chamber are detailed in section 4.3. Typically XHV pressures can be achieved following 2-3 weeks of baking at $\sim 125^\circ$ C.

Diffusion

Diffusion refers to the movement of molecules within the bulk material of the vacuum chamber or components within the chamber to the surface, where they are released into the vacuum space [67]. Out-gassing from diffusion occurs at a lower rate than from adsorbed molecules, but over a much longer time period, and can dominate the out-gassing of baked vacuum chambers at low pressures. The main source of molecules which out-gas through the diffusion process is from H_2 molecules which have been dissolved into the stainless steel of the vacuum chamber during production. The diffusion flux rate is expressed as [65, 66]

$$\frac{dn}{dt} = \mathrm{D}\frac{d^2n}{dx^2} \tag{2.12}$$

where the diffusion coefficient (D) is given by $\mathrm{D}_0 \exp\left(-\frac{\mathrm{E_D}}{\mathrm{RT}}\right)$, the diffusion constant D_0 is material specific, $\mathrm{E_D}$ is the diffusion energy and $\frac{d^2n}{dx^2}$ is the particle flow rate within the solid. Similar to adsorption, the out-gassing rate for diffusion has an exponential dependence on the temperature. Unlike adsorption, the process of re-absorbtion of molecules into the bulk is very slow and once molecules have been removed, diffusion does not significantly contribute to the vacuum level. Vacuum chambers are vacuum fired, baked at $\sim 950^\circ$ C under a vacuum, to reduce the number of absorbed molecules within the bulk of the chamber. Once vacuum fired, the dominant source of outgassing will be from any non-metallic materials within the vacuum chamber which cannot be baked at such high temperatures. Plastic materials are a particularly significant material for out-gassing because of the high water concentration that can be absorbed, and the difficulty in heating to high temperatures. Plastic out-gassing rates are limited by the rate of diffusion and therefore represent a long term out-gassing load.

2.3.5 Advantages and challenges of storage ring measurements

Reaction measurements using storage rings can provide many benefits compared to conventional techniques and have the potential to address many open questions in nuclear astrophysics. However, these measurements can be challenging to perform.

Ultra-thin target and electron cooler

The target density of the internal gas-jet target is typically in the range of 10^{12} to 10^{15} atoms/cm^2. This offers the advantage of minimal beam energy losses, typically only several electron-volts per revolution. Any energy losses are compensated for by the electron cooler, which maintains a constant and precise interaction energy. This is in contrast to more conventional measurements using thick targets, in which beam energy losses within the target can be of the order of several tens to hundreds of keV, resulting in reactions occurring over a range of energies throughout the target. Precise knowledge of the interaction energy is crucial for an accurate determination of the reaction cross section. This is as the cross section can have a strong dependence on the energy of the interaction, either from tunneling through the Coulomb barrier at low energies, or from resonances present in the cross section. Reaction products also experience minimal energy losses ($\sim$ eV) in the ultra-thin target, which allows all reaction products to escape the target and potentially be detected. This is particularly advantageous for reactions at low energies or with a negative Q-value, where reaction products can have low kinetic energies and may not escape the target in conventional thick target measurements. The luminosity achievable with a thin target is reduced compared to thicker targets due to the decreased target density. However, recirculation of the beam in the ring and the use of the stacking procedure to increase the beam intensity means relatively high luminosities can still be achieved while maintaining the benefits of an ultra-thin target.

Beam and target purity

In conventional measurements, beam ions can interact with contaminants in the experimental setup and give rise to beam induced background. This background can produce signals which overlap with those produced by the reaction of interest. Contaminants can be present within a target, condensed on surfaces in the setup such as target windows or present within the beam itself. The number of contaminant particles

may be very small compared to the number of target or beam nuclei. However, the interaction mechanism by which contaminants produce a background signal may be orders of magnitude greater than that of the reaction of interest. The minimal number of contaminants present in storage ring measurements offers another advantage over more conventional measurements. The magnets in the ring are tuned so that ions must have a specific A/Q ratio to remain circulating in the ring. Ions with a different A/Q ratio are eventually lost from beam, resulting in a high purity ion beam. The lack of contaminants in the beam, in addition to a pure, windowless gas target, eliminates the majority of the beam induced background that may be present in other experimental techniques.

Detection efficiency

Measurements on storage rings often utilise a hydrogen or helium target with a heavy projectile (inverse kinematics). The heavy recoil nuclei produced in such a reaction are focused at low laboratory angles (see figure 1.6). This focusing effect requires detectors to cover a much reduced area to detect a large proportion of the reaction products. The high detection efficiency of these heavy recoil nuclei, which may not even escape the target in conventional measurements, presents another benefit of storage ring measurements. Coverage of a large proportion of the products angular range not only allows for very high detection efficiencies, but also accurate determination of the angular distribution if the detectors used are highly segmented.

Radioactive isotope beams

The benefits of the electron cooler, recirculation of the beam in the ring, in addition to the purity of the beam and ultra-thin target are even more pronounced for reactions involving radioactive isotope beams. Radioactive isotope beams have allowed many reactions involving unstable nuclei to be performed. The production of RIBs for exotic isotopes far from stability presents several major challenges including; low production cross sections, production of unwanted nuclei, and the short half lives of nuclei of interest [69]. The production of RIBs fall broadly into two main categories; isotope separator on line (ISOL) [70] and in-flight production [58]. ISOL beam production is dependent on the physical and chemical properties of the isotope of interest, and some exotic nuclei cannot yet be produced at sufficient intensities for nuclear reaction

studies. The major benefit of in-flight production is that nuclei from across the nuclear chart can be produced with no chemical restrictions, however the beam emittance and energy spread can be poor [58]. The emittance can be decreased by reducing the angular acceptance of the fragment separators, but this can result in lower beam intensities. These limitations make studies of certain exotic isotopes prohibitively difficult with traditional techniques. Utilising storage rings, reaction studies involving beams of radioactive isotopes previously inaccessible due to low beam intensities can be performed with minimal contaminants, low beam emittance and high detection efficiencies.

Challenges

Several challenges are present for performing reaction measurements at storage rings which make such measurements difficult and for some reactions not feasible. The main technical challenge for an experimental setup is the XHV vacuum level required. Achieving XHV pressures requires ultra-clean conditions and vacuum compatible materials and equipment. This includes any silicon detectors and the accompanying cabling placed under vacuum. The extensive vacuum commissioning required to produce a detector array compatible with XHV conditions is covered in chapter 4. Other challenges relate to specific reactions and the feasibility of those reactions. The beam lifetime presents a limitation on the energy reactions can be performed at. In the CRYRING, the beam lifetime restricts energies to $\sim$ 100 keV/u, this is dependent on the specific reaction. Reactions at low energies with very low beam lifetimes, especially for exotic beam nuclei which may require several deceleration, cooling and transfer cycles to produce may be prohibitively difficult to perform. The beam intensity achievable also presents a limitation to certain reaction measurements. Storage rings will allow some reactions involving previously inaccessible exotic radioactive beams to be performed, but the deceleration and transfer efficiency between the ESR and CRYRING is still uncertain. This requires further investigation for some reactions involving exotic nuclei.

2.3.6 Previous measurements using storage rings

Storage rings have been a useful tool for experimental physics for decades, however direct nuclear reaction measurements at storage ring facilities have only recently become an active area of research. This methodology has been pioneered at the ESR with proton and alpha scattering measurements using a complex array of Si(li) pad detectors under ultra high vacuum (UHV) and detectors outside of UHV by the EXL collaboration [71]. Commissioning of the setup was performed using ^{136}Xe at an energy of 350 MeV/u incident on a hydrogen target, before subsequent measurements of ^{56}Ni(p, p)^{56}Ni [72–74] and ^{58}Ni(α, α)^{58}Ni [75, 76]. A similar measurement of ^{58}Ni(p, p)^{58}Ni has also been performed at the cooler storage ring (CSR) [77]. Proton capture reactions have also been studied at the ESR with a setup of silicon detectors placed behind the dipole magnets of the storage ring. Reaction products are separated by their charge to mass ratio from the un-reacted beam and steered onto the detectors by the dipole magnets. This setup was commissioned using the ^{96}Ru(p, γ)^{97}Rh [78] reaction, with the detectors installed in pockets which were not directly exposed to UHV, before subsequent measurements of the ^{124}Xe(p, γ)^{125}Cs [62] and ^{118}Te(p, γ)^{119}I [79] reactions utilising silicon detectors installed directly under UHV. A measurement of ^{20}Ne(p, d)^{19}Ne as a proof of principle for future transfer reaction studies has also been performed at the ESR [80].

Chapter 3

CARME

3.1 Nuclear measurements using CARME

The CRYRING Array for Reaction Measurements (CARME) is a charged particle detection array mounted in the experimental section on the CRYRING storage ring. Nuclear reaction studies utilising CARME differ from previous storage ring measurements by the movement and high segmentation of the detectors, in addition to XHV conditions of the CRYRING. The detectors are positioned at low angles, close to the circulating beam ($\sim$ mm) and installed directly under XHV pressures with no windows or pockets. The detectors are able to move, which is required to avoid un-cooled beam which can have a beam diameter of several centimetres when first injected into the ring. When the beam has been cooled, the beam diameter is typically < 5 mm and the detectors are moved closer to the circulating beam. High detection efficiencies and high resolution angular distributions can be attained in inverse kinematics, due to reaction products being focused at the low angles covered by the CARME detectors. The measurement follows a cycle synchronous to the storage ring cycle. Detectors are moved out of the beam path during injection of beam. When the beam has been decelerated and cooled, detectors are moved close to the beam and the internal target is turned on. The measurement proceeds until the luminosity has decreased to the extent where it is more favourable to dump the beam and re-inject at a higher beam intensity. The detectors are moved out of the beam path before the beam is dumped and remain out until the re-injected beam has been cooled.

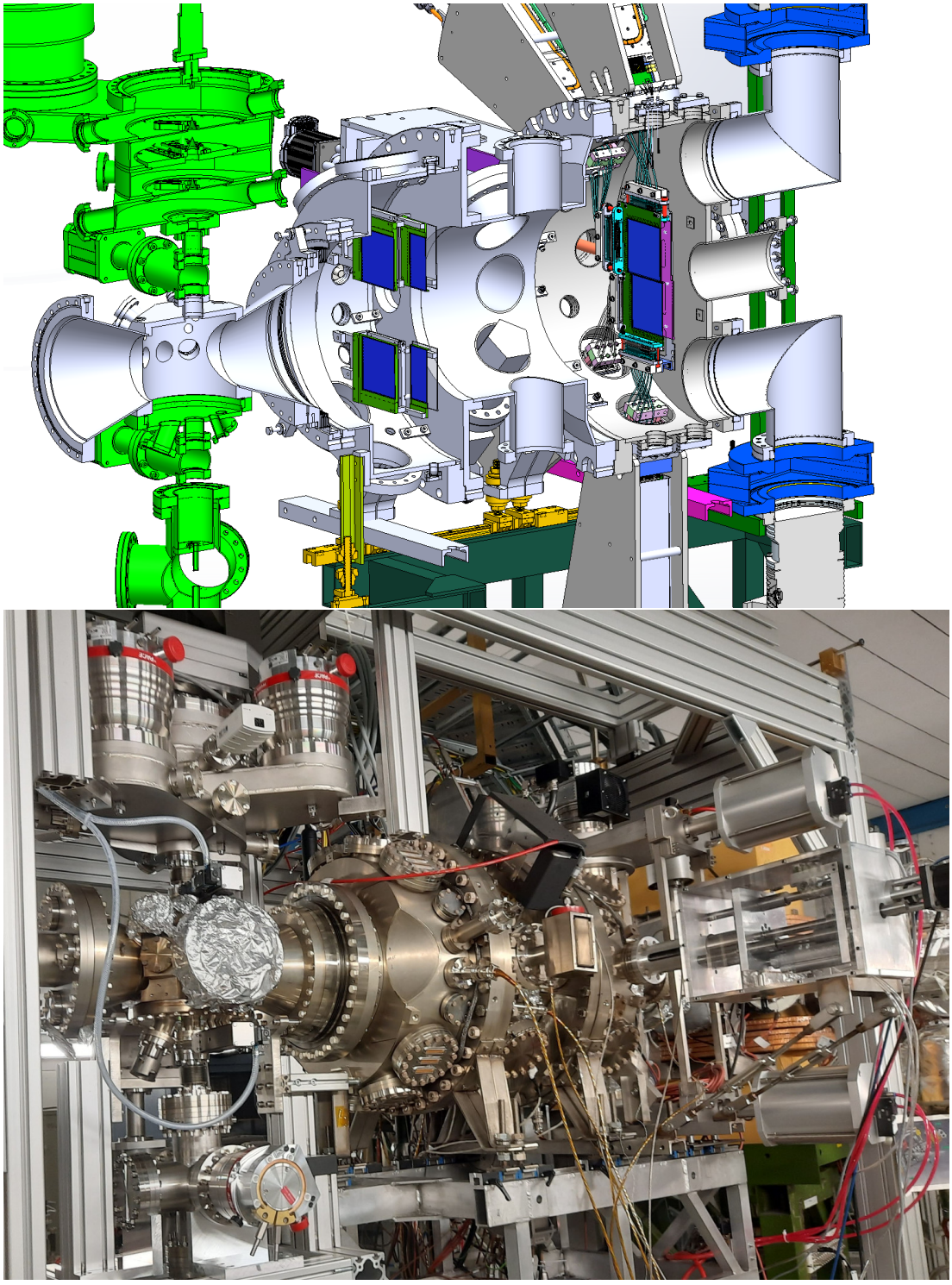

Figure 3.1: CAD model render of the CARME chamber (top). The components of the gas-jet target (green) are mounted above and below the interaction chamber (grey). A bank of static detectors (blue) are mounted close to the interaction chamber with the moving detectors (blue) located further from the interaction chamber. Image of the CARME experimental setup mounted on the CRYRING (bottom). Beam circulates from left to right in both images.

3.2 Experimental setup

The CARME experimental setup is described in reference [1]. It is comprised of a cryogenic gas-jet target station [81] (green in figure 3.1) mounted above and below an interaction chamber (grey in figure 3.1) with a main detection chamber (grey in figure 3.1) capable of housing up to six static and four moving XHV compatible double sided silicon strip detectors (DSSDs, blue in figure 3.1). The cryogenic gas-jet target is similar to that utilised for previous nuclear reaction measurements in the ESR. The gas-jet target was installed and commissioned on the CRYRING during the same beamtime as the commissioning of the CARME setup. The CARME detection chamber can be mounted up and/or downstream of the target. The interaction chamber provides ± 20 degrees line of sight from the gas jet target to the detectors. The interaction chamber and CARME detection chamber have multiple ports to which vacuum, diagnostic or measurement equipment can be mounted. The data acquisition is handled by front end electronic (FEE) modules which are mounted on the outside of the detection chamber. In September 2021, the CARME detection chamber was mounted downstream of the target in CRYRING. Two of the moving silicon detectors were mounted for the commissioning beam time.

3.2.1 Vacuum chambers

The CARME detection chamber consists of three separable sub-sections referred to here as the far, intermediate and wall sections. The sub-sections are sealed by a custom copper wire seal (Pfeiffer, DN600) to maintain vacuum between sections. A CAD model render of the wall and far sub-sections, which house the static and moving detectors respectively, is shown in figure 3.2.

The wall sub-section is closest to the target and is connected to the interaction chamber by a set of custom XHV compatible bellows. The wall has mounting points for six static DSSDs located $\sim$ 480 mm from the interaction point, covering laboratory angles from $\sim$ 5-17 degrees. No DSSDs were installed in this section for the commissioning of CARME. The wall sub-section is the ideal position for vacuum gauges as it is the section closest to the gas-jet target, representing the highest pressure in the chamber. Two IE514 vacuum gauges and four NEG pumps were installed internally in the wall sub-section. The remaining ports were occupied by the Allectra 3×72 way feed-through

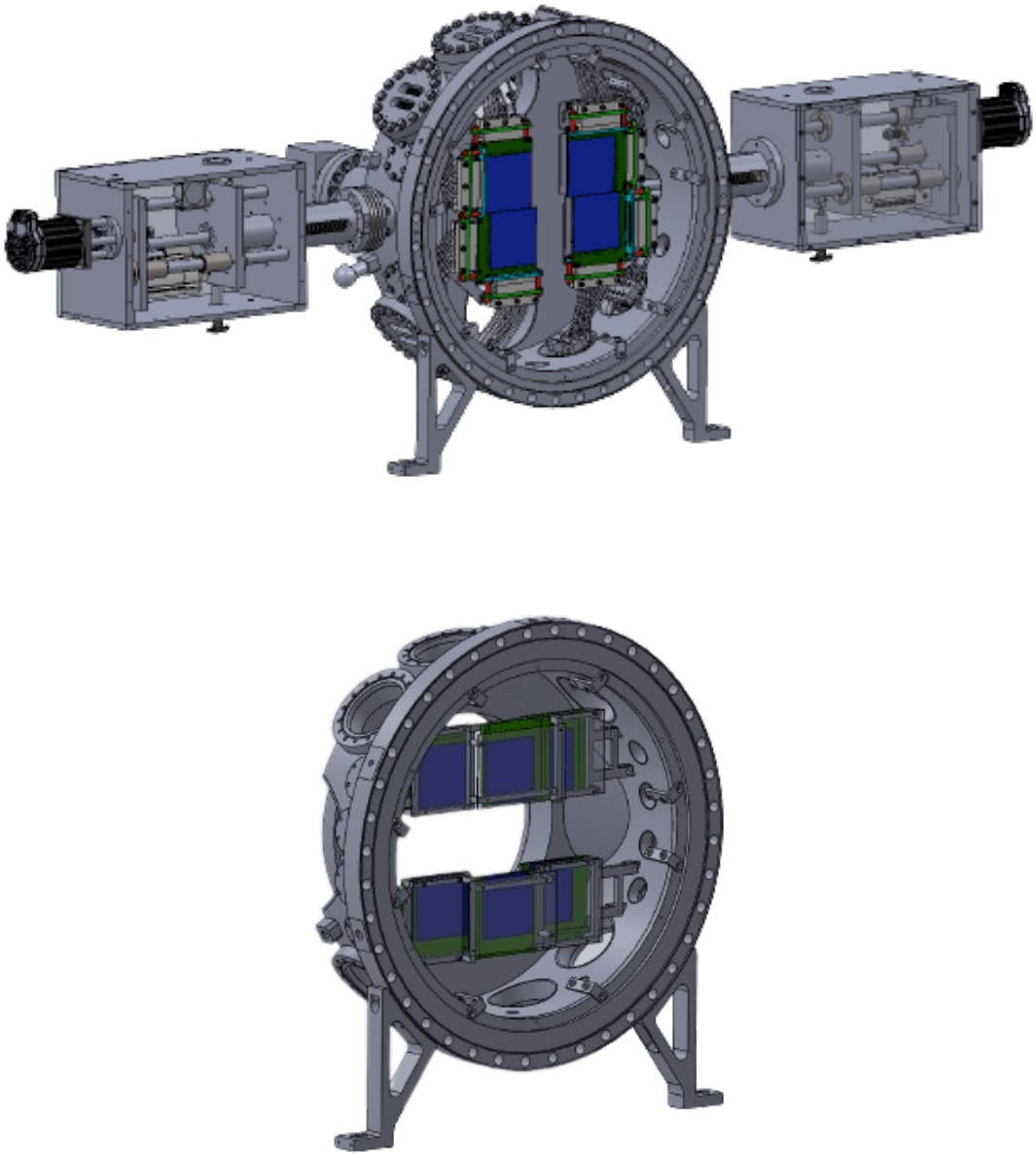

Figure 3.2: CAD model renders of the far sub-section (top) and the wall sub-section (bottom). The detectors in each section are coloured blue. The XHV motors which actuate the motion of the moving detectors are also shown in the top image

flanges which provide electrical connections for the DSSDs not yet installed.

The intermediate chamber section does not support any DSSDs but has multiple flanges available for vacuum, diagnostic or measurement equipment. During the commissioning beam time, the intermediate sub-section space was occupied by vacuum pumps. Two D2000 NEG-ion pumps are mounted on DN100 flanges, in addition to four NEG pumps installed in the sub-section. An additional ion pump supplied by GSI was mounted but not activated.

The far sub-section is devoted to the four moving silicon detectors and equipment necessary for their operation. When detectors are positioned closest to the circulating beam, the laboratory angular range covered by detectors is $\sim$ 0.5-7 degrees. The detectors are mounted on actuator arms whose movement is actuated by a set of XHV motors (see section 3.2.3). The XHV motors connected to the far sub-section can most clearly be seen in figure 3.2. The majority of ports on the far sub-section are occupied by the Allectra 2$\times$72 way feed-through flanges which provide electrical connection for the moving detectors. FEE data acquisition modules are mounted to the top of the feed-through flanges. A thermo-couple feed-through flange is mounted at the top of the far sub-section for monitoring of internal temperatures during bake-out of the chamber. Two all metal VAT valves mounted on L shaped flanges are installed on the downstream end of the far sub-section. VAT valves separate the turbo pumps from the chamber and can be closed to prevent any back-streaming from the turbo-pump in the XHV pressure regime. Two turbo pumps can be mounted, above and/or below the chamber. A small bellows section connects the back of the section to the CRYRING beam line. The total surface area of all sub-sections together is $\sim$ 3 m^2.

The CARME detection chamber is mounted on a steel frame (dark green in figure 3.1). Curved stainless steel feet mounted on the chamber are secured to steel studs mounted on slide-able carriages. The carriages are able to slide along a rail fixed to the steel frame (yellow in figure 3.1). Mechanical stoppers secured either side of the carriages prevent any movement. The steel frame is mounted on four large 'elephant feet' structures which secures the frame to the floor in the CRYRING. The height of the chamber on the frame can be altered by loosening or tightening the nuts which secure the feet to the studs. The position of the chamber was aligned using laser alignment. The modular design of the CARME detection chamber allows individual

sub-sections to be lifted out, which allows for greater access to the remaining sections during installation and maintenance phases.

Interaction chamber

The interaction chamber is where the beam interacts with the gas-jet target. The target station is mounted above and below the interaction chamber. The target station is detailed in section 3.3. The interaction chamber mounted on its stand prior to installation on the ring is shown in figure 3.3. Multiple in-plane ports across the main body of the chamber are available for installation of equipment such as vacuum gauges, CCD cameras or gamma ray detectors. The number and size of ports available, in addition to possible x-ray detectors which could be installed on the interaction chamber are given in the CARME technical design report [82]. The internal surface area of the interaction chamber is ~ 0.58 m^2.

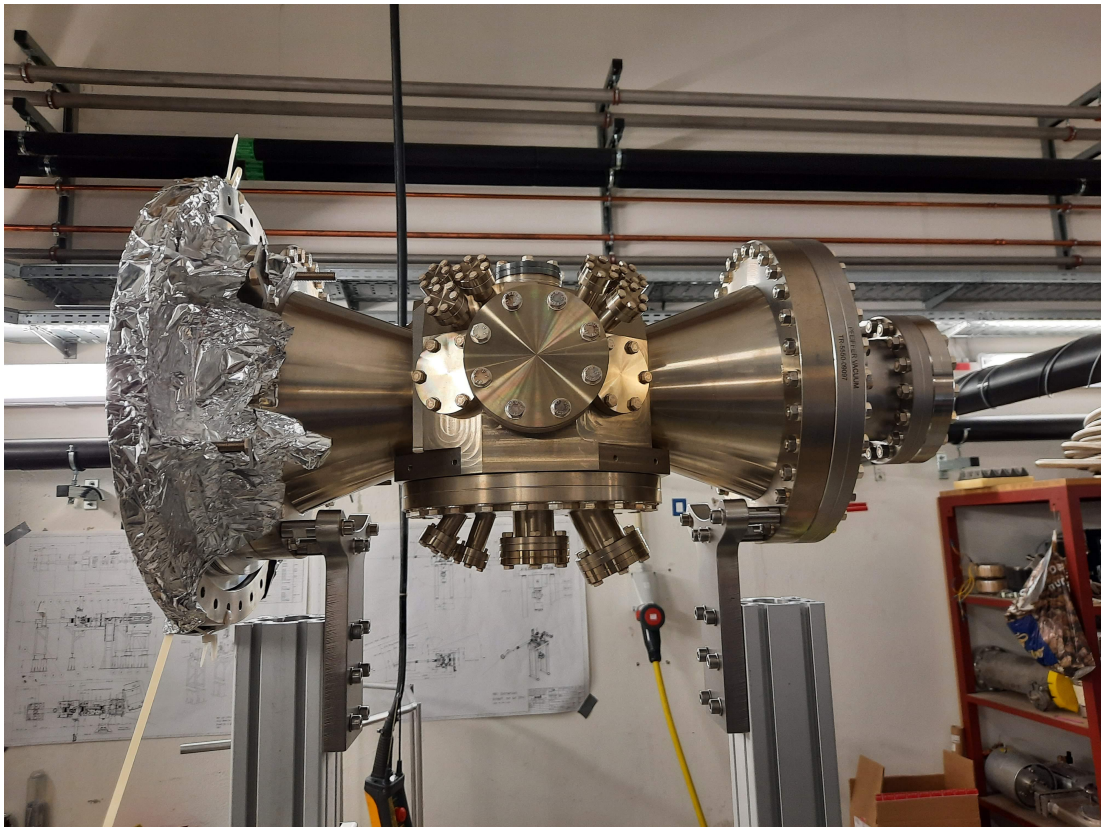

Figure 3.3: Interaction chamber mounted upon its frame prior to installation on the ring. When installed beam travels from right to left with remaining ports on the chamber available for diagnostic or measurement equipment. Aluminium foil covers one end of the chamber to maintain cleanliness during the installation procedure.

3.2.2 Detectors and data acquisition

Silicon detectors are employed in CARME to detect the charged particles resulting from the interaction. The detectors are 10×10 cm, double sided silicon strip detectors (DSSDs) with wafer thicknesses of 1 mm. Each side (x and y) of the DSSDs have 128 strips, with a strip pitch of 738 μm, for a total of 16384 individual pixels. The silicon wafers are mounted in ceramic transmission carriers using UHV-rated silver loaded epoxy glue. The contact pads on the silicon wafers are ultrasonically bonded to contact pads on the carriers. Kapton wires run from the carrier contact pads to the carrier vias. The individual strips and bond wires on each DSSD are visible in figure 3.4. The Detectors are mounted upon a stainless steel plate, secured to an actuator rod whose movement is actuated by the motors system. Ceramic shields are mounted behind the detectors on the plate to protect them against excessive heating from D2000 NEG pumps located behind the detectors. Cable harnesses constructed in Edinburgh relay the signal from the detector carrier to the signal feed-through flanges. The cable harnesses connect to the detector carrier and feed-through flanges by MACOR D-connectors.

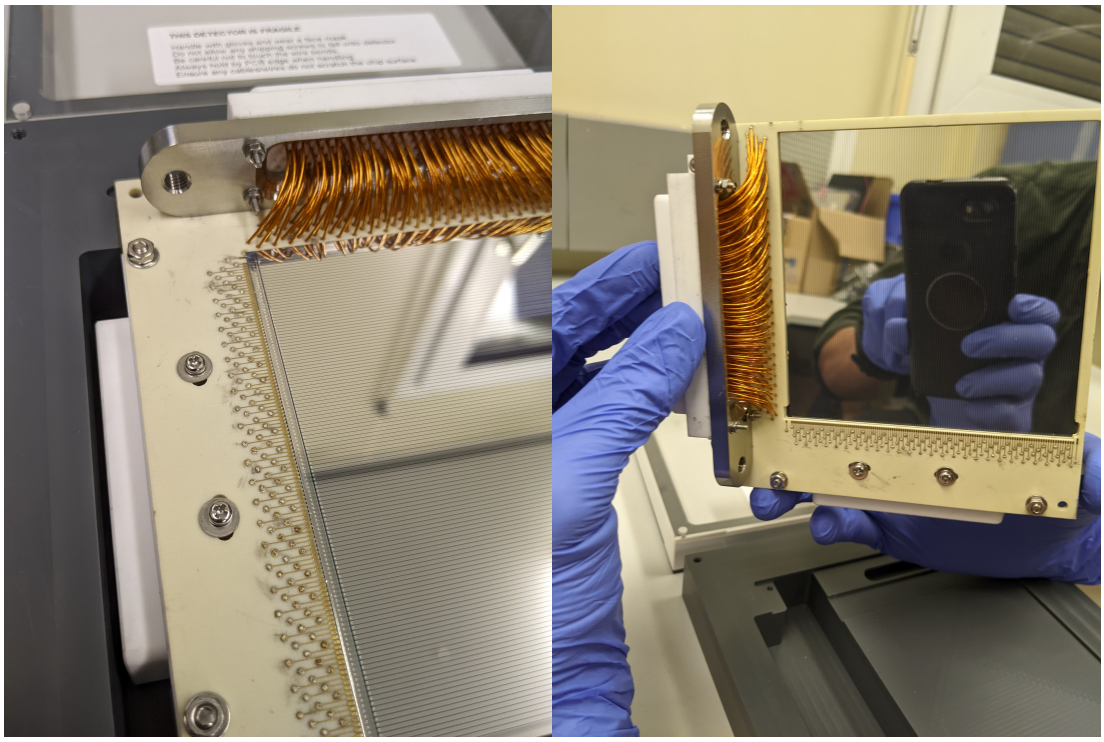

Figure 3.4: Close up view of the DSSDs employed in the CARME array. Individual strips of pitch 738 μm can be seen on the silicon wafer in addition to the bond wires connections on the ceramic carrier.

Wires in the cable harnesses are 0.75 mm outer diameter (OD) kapton coated, silver plated copper wires. The wires have been specifically selected due to their UHV vacuum compatibility, further details of the vacuum effect of the cabling are given in chapter 4. The detectors, cable harnesses and MACOR connectors installed in CARME are shown in figure 3.5. The cable lengths are either 225 mm or 285 mm, dependent on the proximity of the side of the detectors to the feed-through flanges. Cables are subject to constant stresses, due to the movement of the detectors, which may limit the lifetime of cables. The most likely point of failure from excessive stresses is from wires close to the D-connectors of the cable harnesses. Strain reliefs were mounted to the cable harnesses, close to the D-connectors, to restrict the cable motion and extend the lifetime of cables. Strain reliefs consists of a ceramic clamp which cables are fed through in bundles of 8-10 wires. Stainless steel funnels in the strain reliefs further restrict the motion of the cables. An image of one of the ceramic strain reliefs mounted on a cable harness is shown in figure 3.6 and an image of the connection of the cable harness to the detector carrier with no strain relief mounted in shown in fig 3.7. Stress testing of the cabling has been performed in Edinburgh, under vacuum conditions for up to 10,000 repetitions.

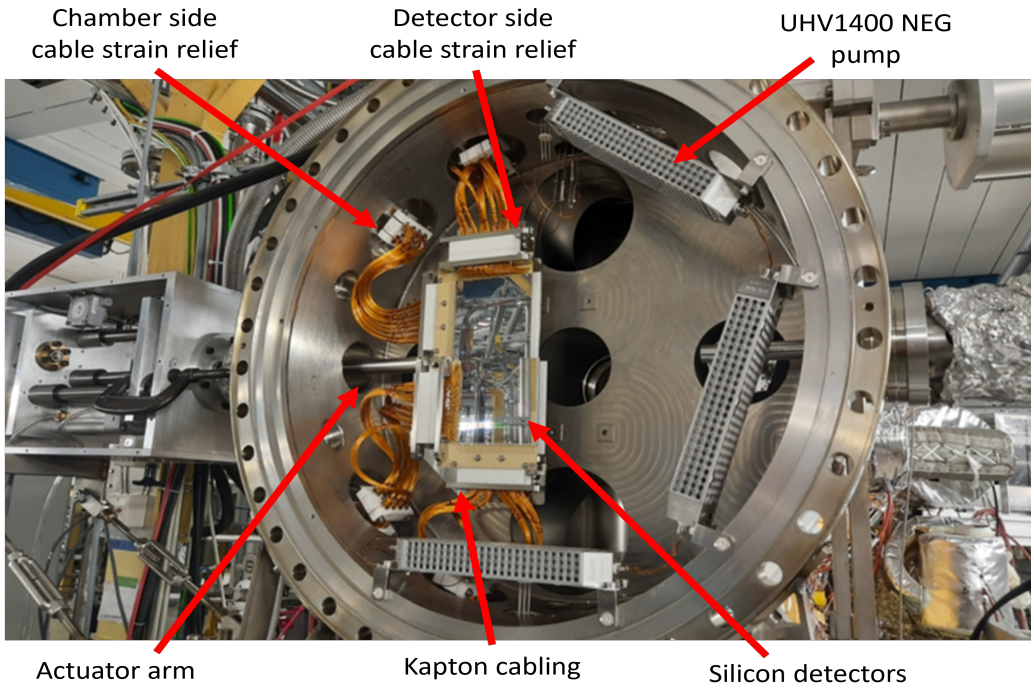

Figure 3.5: Two silicon detectors mounted within the CARME chamber. Kapton cables transfer output signals from the detectors to feed-through flanges on the chamber. MACOR cable strain reliefs are mounted to cable connections to the chamber and to the detector. Three NEG modules are mounted on the edge of the sub-section, two more NEG modules were temporarily removed to aid in the detector installation.

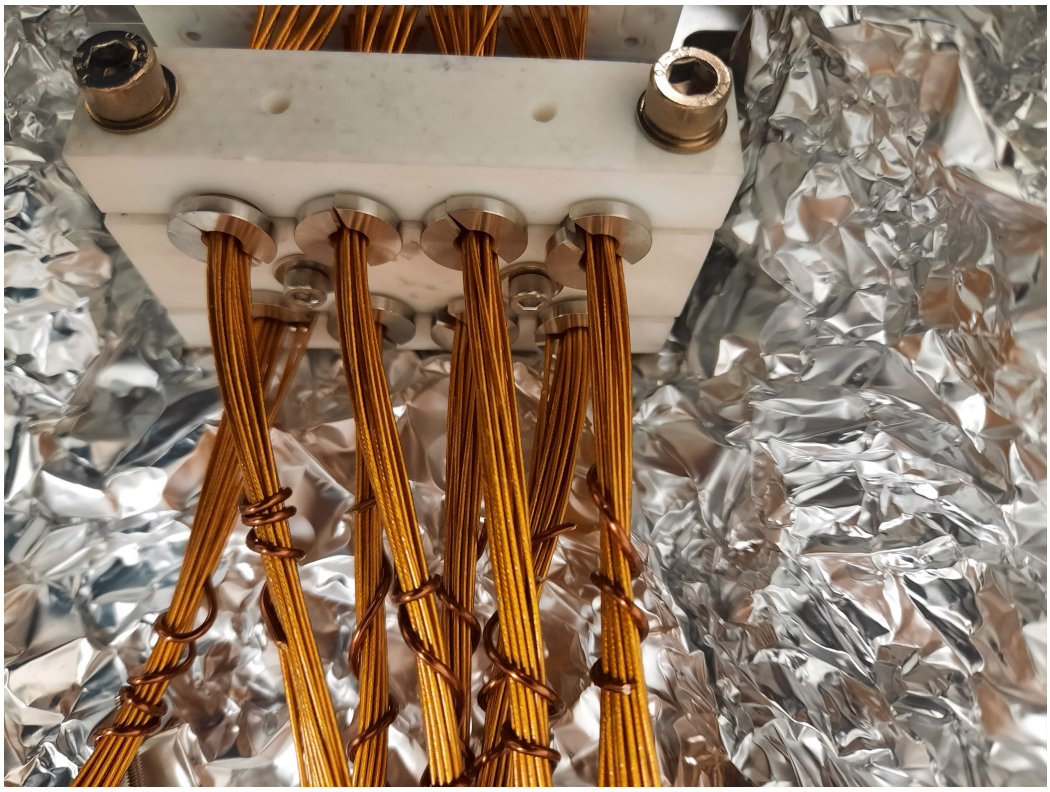

Figure 3.6: Close up view of the MACOR strain reliefs mounted to the cable harnesses. Kapton cables are separated into bundles of 8-10 wires to be fed through strain relief. Additional stainless steel funnels were placed within strain reliefs to reduce cable stress.

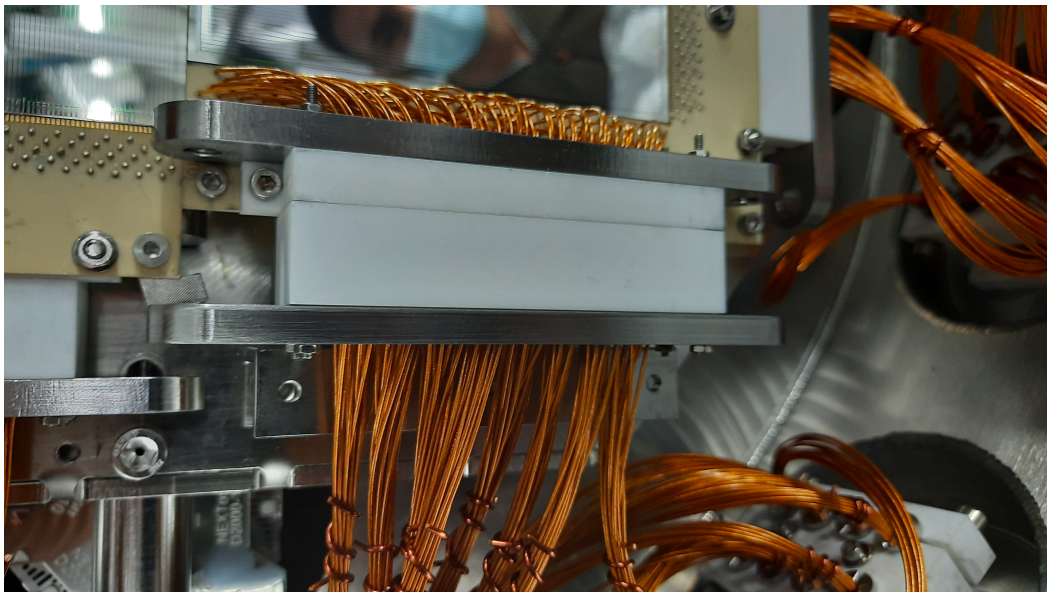

Figure 3.7: Close up view of the cable harness connecting point to the detector carrier. D-connectors are brought together by tightening silver plated screw into the jacking plate of the detector carrier.

Data acquisition

CARME uses the advanced implantation data acquisition (AIDA) system [83, 84] to process signals from the detectors. The AIDA data acquisition system was developed for beta decay applications with high rates and detection of particles over a wide range of energies ($\sim$ MeV-GeV). The event rate of the AIDA system ($\sim$ 10 kHz per channel) is ideal for CARME where high rates of Rutherford scattering are expected. Signals from the detectors are carried along the cable harnesses to the signal feed-through flanges. Adaptor boards (air side) plug into feed-through flanges and relay the output signal to the front end electronics (FEE) modules which process the signals and act as independent data acquisition modules. The FEE modules are placed in isolating holders mounted to the feed-through flanges on the CARME chamber. An image of the FEE modules placed within their holders is shown in figure 3.8. Data is output from the FEE modules via a gigabit Ethernet cable. The data acquisition system is controlled through an online server using the MIDAS data acquisition system graphical user interface (GUI).

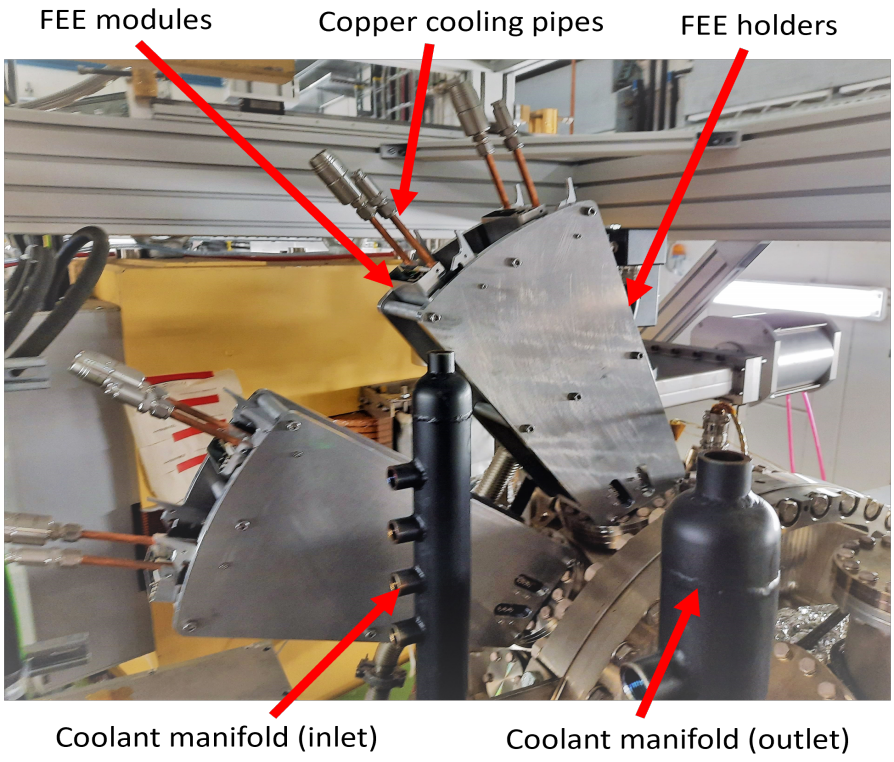

Figure 3.8: FEE modules within their holders mounted on top of the CARME chamber. Copper coolant loops protrude from the FEE modules, which are fed by the coolant manifolds. Wired connections to the modules plug into FEE modules close to the copper coolant loops.

The adaptor boards relay the signal from the feed-through flange to the FEE modules and also act as a connection point for grounding, bias and test input signals through LEMO cables (see figure 3.9). Ground connections are made from the body of the FEE module to the adaptor board, and then from each adaptor board to the local CRYRING grounding point. Ground connections from the CARME detection chamber and steel frame are also made to the same local CRYRING grounding point.

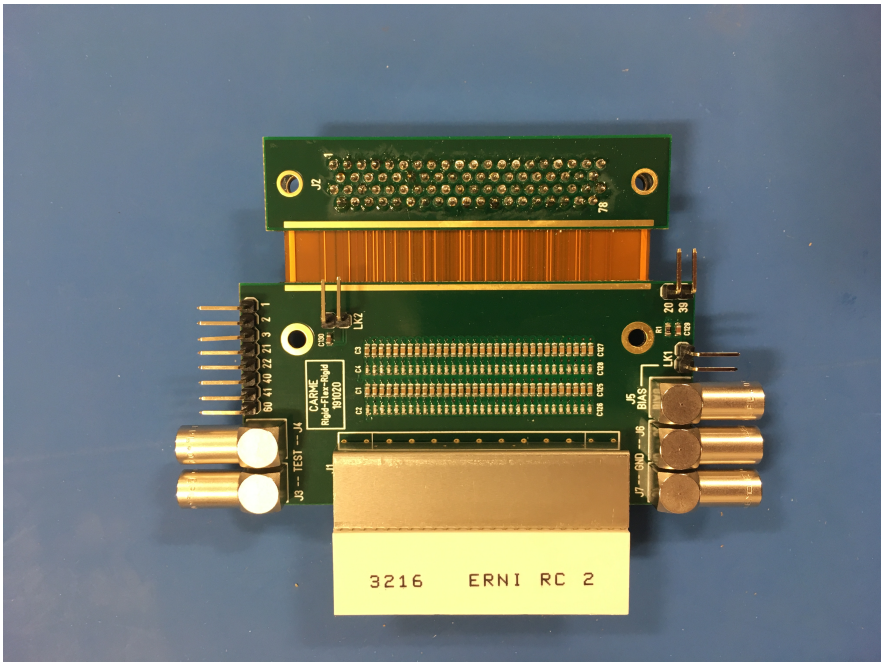

Figure 3.9: Adaptor board for connecting FEE module to feed-through flanges. Top of adaptor board plugs into feed-through flange, ERNI connector provides connection to FEE module. LEMO connections provide connection for 2× test inputs (bottom left - J3 and J4), bias (top right - J5) and 2× grounding (bottom right - J6 and J7). Jumper pins (lk1 and lk2) allow for further grounding

The FEE module consists of four application specific integrated circuits (ASIC), grouped on a mezzanine PCB, connected to an electronics board for processing data. The processing of data and control of the FEE module is handled by the field programmable gate array (FPGA) running custom firmware by STFC Daresbury. The FEE electronics board and ASICs are cooled by an aluminium heat sink block on one side of the board which dissipates heat to a water cooled loop. Two coolant manifolds mounted to the CARME frame (black pipes in figure 3.8), one inlet and one outlet, supply water to the loop at 20° C.

The ASIC has 16 channels, with each FEE module able to handle signals from 64 channels, corresponding to half of the strips for one side (x or y) of the detector. Four FEE modules are required for the operation of one 128×128 strip detector. Each ASIC channel has two pre-amplifiers, shaping amplifiers and discriminators. One of the pre-amplifiers has a selectable gain for low/medium energy applications with a full scale range (FSR) up to 20 MeV/1 GeV and one for high energy applications with a FSR up to 20 GeV. The high energy pre-amplifier is disconnected from the circuit and is only active when the low/medium energy channel becomes saturated. Details of the ASICs can be found in references [83, 84].

Low energy nuclear reaction applications ($\lesssim$ MeV/u) in CARME will primarily utilise the high gain, low energy pre-amplifier for the energy range up to 20 MeV. Selection of the low energy pre-amplifier, maximises the energy resolution in the energy range of primary interest to low energy nuclear reactions. The output of each ASIC is connected to a 32:1 multiplexer with valid ADC data sequentially read out via the multiplexer [83, 85]. Timing information in the form of a partial timestamp relative to the FEE internal clock, a range indicator, channel and FEE number, in addition to the ADC value are stored in the ADC data item using the GREAT data format [86]. Reconstruction of the full timestamp is completed when the data from individual FEE modules is merged into a single data-stream. Synchronisation information data items are input into the data-stream containing the remainder of the timestamp from an external clock. Information data items are also used to store other information such as signals for movement of the detectors. The external common clock for the SYNC information data items are input into each FEE module from custom NIM (MACb) modules by a mini HDMI connection. Each MACb module can support four FEE modules. Applications with more than four FEE modules require multiple MACb modules, which need to be ordered hierarchically. CARME requires 16 FEE modules to operate the four moving detectors, requiring five MACb modules. The ordering of MACb modules is detailed in reference [85].

The data acquisition is controlled through several online MIDAS servers. The status of the FEE modules and DAQ is monitored and controlled from the main control server. ASIC parameters such the energy thresholds can be set, with live wave-forms and histograms for each channel viewable in a separate tab on this server. Live histograms were utilised during the initial calibration of the DAQ and are a useful tool for monitoring throughout an experimental period. A second server merges the data from each

FEE and writes the data to disk. An online sorting code (CARME-SORT), running in a third server, is also active during data taking to monitor data from the experiment in real time. The CARME-SORT code unpacks the raw data, builds events for further analysis and outputs various histograms. Events are built by combining ADC data which are separated by less than 2 μs, the time between readouts of the AIDA multiplexer. The energy of the event is then calculated using parameters for each detector strip determined during the energy calibration procedure (see section 5.3.1). The x and y position of the event is determined by applying the DSSD geometry. The CARME-SORT code is adapted from the AIDA-SORT code, further details of which are given in reference [85]. One of the key outputs during monitoring is an energy histogram of events in the last 10 seconds. The Rutherford scattering peak in this histogram was used by GSI beam handlers to align the beam with the gas-jet target. The Rutherford scattering rate is also used to safely set the detector position during early experimental runs.

3.2.3 XHV motors

The moving detectors are mounted on actuator arms facilitating their movement. The relative position of the actuator arms have a precision of 0.1 mm measured by a string potentiometer, whose resistance is proportional to its extension. A labelled image of the motors system is shown in the top image of figure 3.10. The silicon detectors are mounted on a stainless steel mounting plate attached to a metal shaft. The metal shaft passes through a set of custom XHV bellows from vacuum to air. The motion of the metal shaft is actuated by the combination of a pneumatic cylinder and a servo motor. Mechanical shock to detectors is limited by buffers fitted to the pneumatic cylinder which limit the acceleration at the end of each movement. The XHV bellows are rated for 1 million cycles in their lifetime, sufficient for one cycle every ten seconds continuously for more than 100 days.

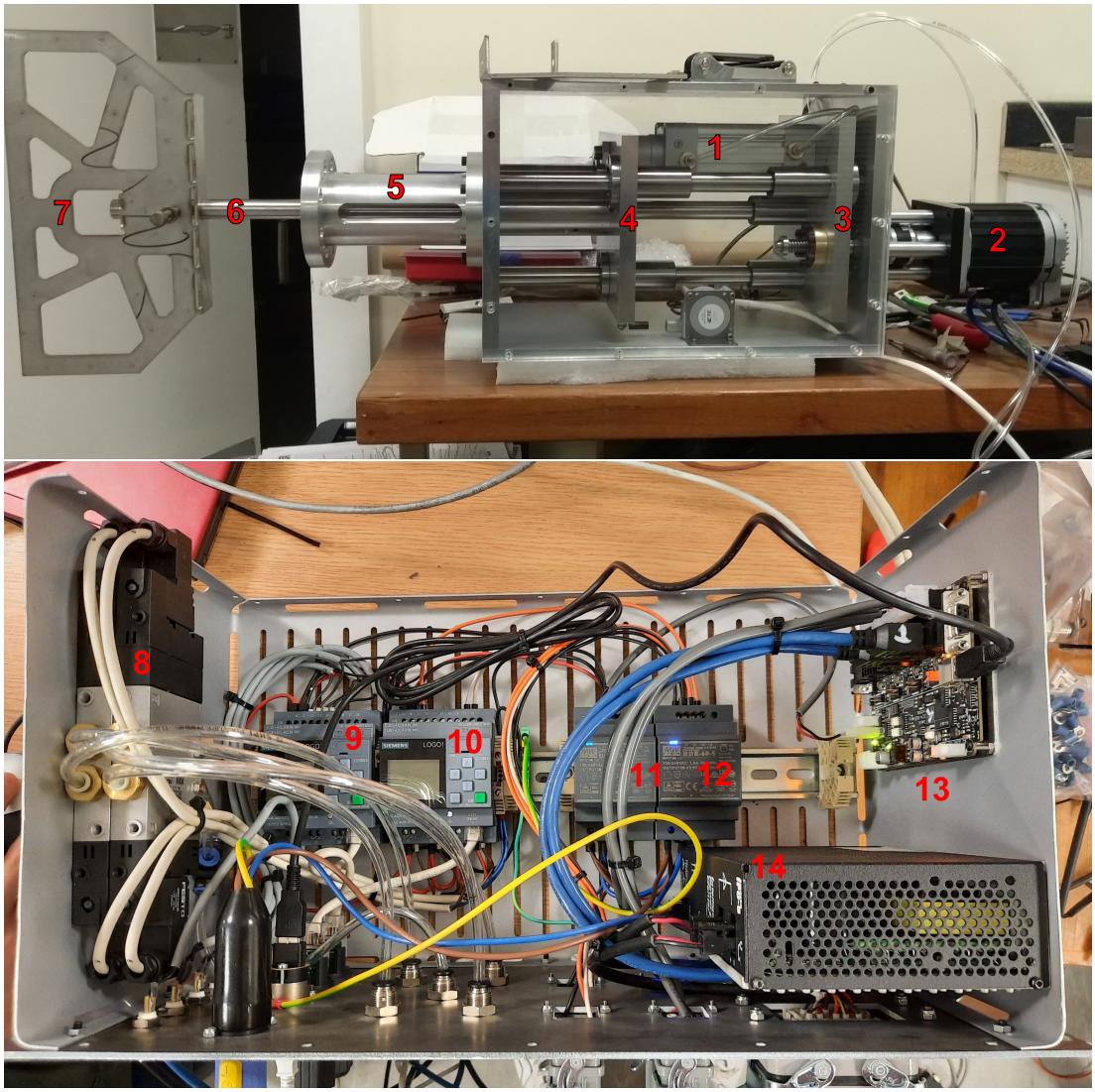

Figure 3.10: Image of the motors system during testing in Edinburgh (top). 1=Festo Pneumatic Cylinder 50 mm Bore, 50 mm Stroke, 2=Teknic CPM-SCSK-3432P-ELSA servo, 3=moving plate, 4=second moving plate, 5=space for XHV bellows not pictured, 6=316L metal shaft, 7=316L mounting plate for silicon detectors. Image of internal components within the motors control box (bottom). 8=Festo 5/3 solenoid pilot valve, 9=Siemens Logo! PLC for ring I/O, 10=Siemens Logo! PLC for motor control, 11+12=Mean well HDR-30 DIN rail power supply for PLCs (36 W, 24 V DC), 13=Teknic SC4-HUB (communication hub), 14=Teknic IPC-5 power supply (75 VDC output, 350 W DC)

The motors system is controlled by a program running on a Raspberry Pi. Motion can be manually controlled or automated using a set of commands. Automated motion can be based on signals specifying the current status of ring operation, such as beam injection or cooling. The current maximum range of motion is $\sim$ 55 mm which is completed within $\sim$ 1-2 seconds. The interface between the Raspberry Pi and the motors is controlled by electronics in the motors box. A labelled image of the motors box is given in the bottom plot of figure 3.10. If the motion is automated based on signals from the ring, then the motion is initiated by the following electronics chain. A signal from the storage ring, such as injection of beam, is received by the programmable logic controller (PLC) for ring input/output (I/O) (9 in figure 3.10) which relays the signal to the Raspberry Pi. The Raspberry Pi instructs the PLC for motor control (10 in figure 3.10) which opens or closes the compressed air valve (8 in figure 3.10) allowing movement of the pneumatic motor. The PLC for motor control also sends movement commands to an electronics board (13 in figure 3.10) which controls the servo motor. Limit switches from the motors instruct the servo electronics board on the maximum allowed range of motion. If the motors reach this limit, the switch is triggered and no further motion is permitted. The motors remain in position at the end of the movement cycle until a new command from the Raspberry Pi is received.

3.2.4 Vacuum equipment

The CARME detection chamber and the interaction chamber must be in the XHV pressure regime to operate on the CRYRING. In order to do so, the out-gassing rate must be minimised and sufficient pumping power must be installed so that the pumping speed is equivalent or exceeds the out-gassing rate of both the vacuum vessel and in-vacuum instrumentation. The largest source of out-gassing is the total of 261 metres of 0.75 mm OD, Kapton wires in the cable harnesses. Plastics are usually avoided in UHV and XHV vacuum systems, however Kapton is a low outgassing material, which if properly treated is viable for XHV applications. The final out-gassing rates depend on the cleaning and bake-out procedures which requires experimental testing, as no literature existed before this thesis for substantial amounts of Kapton placed under XHV conditions. The procedures used to minimise outgassing from materials and calculations of the outgassing rates are detailed in chapter 4.

Two 300 litres per second (l/s) turbo-molecular pumps (Leybold MAG W 300i), with rotors suspended by magnetic bearings can be mounted above and below the far sub-section. All-metal (VAT) gate valves are installed between the turbo-molecular pumps and the vacuum chamber, with an oil-free scroll pump (Edwards nXDS 15i) connected to the backing line of the turbo. This combination of vacuum pumps is sufficient to achieve UHV pressures down to $\sim 10^{-8}$ mbar. Turbo-molecular pumps are not sufficient to further decrease the pressure to the low UHV/XHV vacuum regime. A combination of NEG and ion pumps in addition to bake-out of the vacuum chambers is required. 13 Non Evaporable Getter (NEG) pumps (UHV1400 SAES Getters, see figure 3.11) and 4 NEG/Ion combination pumps (NEXTorr D2000 SAES Getters, see figure 3.11) are installed in the CARME detection chamber. Feed-through flanges allow for electrical connections between power and control modules (in air) and the NEG pumps under vacuum. UHV1400 NEG modules are connected in groups of 2-3 modules in series inside the chamber by kapton coated copper wires. Groups of modules are then connected to the feed-through flanges. The combined pumping speed of molecular hydrogen of the UHV1400 and D2000 pumps is 26,200 l/s. The pumping speed varies dependent on the gas species. Molecular hydrogen comprises the majority of the residual gas present following bake-out, so pumping speeds are expressed using the H_2 rate. Two Hot Cathode gauges (Leybold Ionivac IE514) are installed on the wall sub-section chamber which are capable of measuring pressures down to 2×10^{-12} mbar.

NEG pumps work by capturing residual gas molecules via adsorption on the surface of the getter [68]. Reactive gases chemically bind to the surface and dissociate, producing an ion layer which diffuses into the bulk of the getter over time. Hydrogen molecules react with the getter surface and dissolve into the bulk. Un-reactive gases, such as noble gases, do not react with the surface and are not pumped by NEG pumps. NEG pumps are passive once in operation, but require activation at high temperatures as the surface becomes saturated and un-reactive in non UHV conditions. NEG pumps are activated by heating the NEG modules to $\sim 550^{\circ}$ C to remove the dissolved hydrogen within the bulk and increase the diffusion of the surface ion layer into the bulk. This process activates the surface for the capture of gases [66]. NEG pumps can be re-activated multiple times under vacuum to increase pumping speed. Ion pumps capture gas molecules by ion implantation. Residual gas molecules are ionized within the pump cell and then accelerated towards the cathode in the pump. The ions will either be

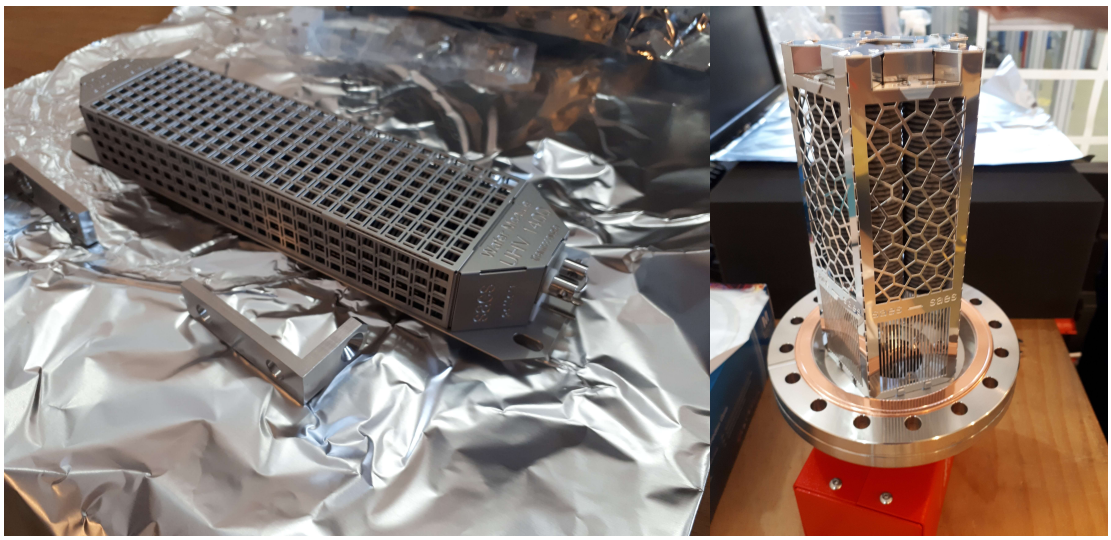

Figure 3.11: Image of the SAES UHV1400 NEG pump (left) and SAES NEXTOR D2000 NEG-ion combination pump (right). Stacked getter disks provide the NEG pumping power of 1400 and 2000 l/s (H_2) respectively. UHV1400 pumps are electrically connected in groups of 2-3 modules. Integrated into the D2000 pump is an ion pump providing additional pumping power.

buried below the cathode surface or sputter reactive cathode material, usually titanium, onto surrounding surfaces which acts as a getter to remove reactive residual gases [66]. The pumping speed of ion pumps are typically much lower than that of NEG pumps. The D2000 combination NEG-ion pumps used in CARME have a 2000 l/s NEG pumping speed and a 10 l/s (Ar) ion pumping speed. A combination of NEG and ion pumps is used in CARME due to the limitations of each type of pump. The challenge of removing un-reactive gases from the chamber is particularly challenging with the use of gas targets such helium or argon. Additional ion pumps in CARME and additional turbo molecular pumps in the target dump section may be required for heavy noble gas species.

3.3 Gas-jet target

The CRYRING gas-jet target is a specially designed system for producing an XHV compatible, ultra-thin gas target for use on storage rings. The target station is similar to the ESR gas-jet target [81] and the CRY-JET [87] target originally installed on the CRYRING in Sweden. The target was commissioned simultaneously with the CARME detector array. The target section consists of three major components; the injection system consisting primarily of the cryostat and target nozzle, an inlet system of skimmers (collimators) in four differentially pumped chambers and a dump section consisting of three chambers. A labelled 3D render of the target station is shown in figure 3.12. Gas is fed into the system at high pressure ($\sim$ 10s of bar) and cooled by the cryostat to temperatures as low as 4 K by liquid nitrogen. The target nozzle is trumpet shaped with a pinhole orifice of diameter ranging from 10-30 μm. Gas flows through the orifice at high pressure and low temperature (close to the critical point for the gas species). Passing through the nozzle, the gas expands isentropically (entropy is conserved). No energy or mass transfer occurs with the surroundings such that the expansion reduces the temperature and pressure of the gas rapidly, and produces a directed gas jet [81, 88]. The rapid reduction in pressure and temperature can lead to a phase transition facilitating the formation of clusters within the gas jet. The molecular clusters can consist of particles ranging in size from the nanometer to the micrometer scale [89]. For lower source temperatures, the produced jet can be in a liquid state with a higher density than a similar gas jet. To reduce the divergence of the jet and reduce the vacuum load to the ring, the jet is passed through several skimmers located in differentially pumped chambers. In the CRYRING target, the distance between the first skimmer and the interaction point is $\sim$ 40 cm. The skimmer diameters from the first stage closest to the nozzle are 0.2, 0.3, 0.8 and 1.5 mm. The first two skimmer stages determine the target profile, with the third and fourth skimmer stages primarily for the reduction of the vacuum load to the ring. This combination of skimmers is expected to produce a target interaction width (Δ x) of $\sim$ 1 mm [90]. The target nozzle is mounted on a translator system which is used to align the target nozzle with the skimmer positions. An image of the target nozzle and the production method of the gas jet is shown in figure 3.13.

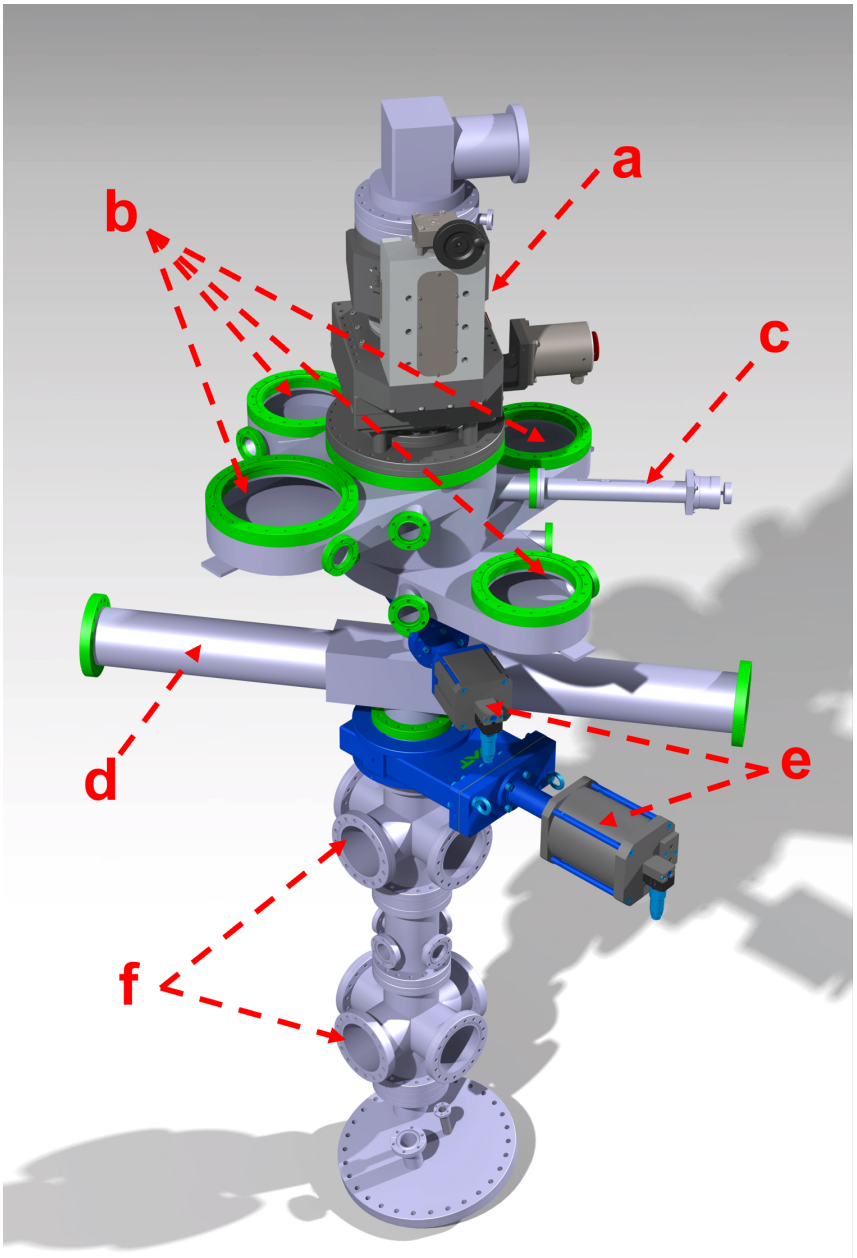

Figure 3.12: 3D render of the Gas-jet target taken from reference [90]. The cryohead and xyz translational stage (a) are mounted on top of the inlet chamber. The four differential pumping stages are labelled (b) with a linear manipulator to allow different skimmer to be used for the second differential stage is (c). The interaction chamber is modelled by a blank pipe (d) in the 3D model. Two valves (e) protect ring vacuum in case of target malfunction. Stages of the target dump section are labelled (f).

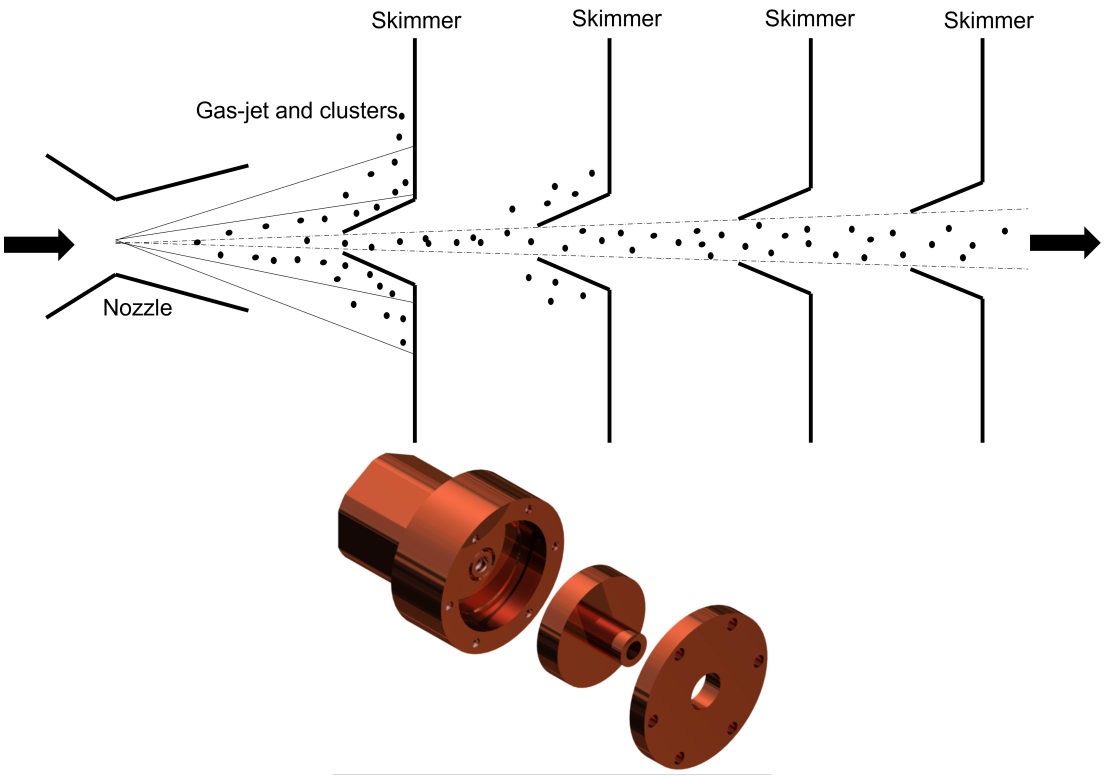

Figure 3.13: Sketch of the principle for the formation of the gas jet and clusters within the jet (top). The divergence of the jet is reduced by skimmers in differential pumping stages before target reaches the interaction chamber. Sketch adapted from figures in references [81, 88, 89]. CAD model render of the pinhole orifice and nozzle for the CRYRING target (bottom)[90]

Turbo-molecular pumps are used to evacuate the differential pumping stages. A 800 l/s turbo pump is equipped to the first stage with 700 l/s turbo-molecular pumps utilised for the remaining three stages closest to the ring. The target particles pass downward through the interaction chamber and into the dump section where they are pumped out of the system. The target dump consists of three chambers, two with 300 l/s turbo-molecular pumps and one with a 1600 l/s turbo-molecular pump. It is assumed all target particles that pass through the interaction point reach the dump chambers due to the geometry of the target. The target area density can therefore be calculated by considering the mass flow through the turbo-molecular pumps in the dump sections [88]

$$n = \frac{4}{\pi k T} \frac{1}{v \Delta x} \sum_{i=1}^{n} (S_{\mathrm{i}} \Delta p_{\mathrm{i}}) \tag{3.1}$$

where n is the target area density, Δx is the target width, T is the temperature of the dump chamber (300 K), ΔP_i is the partial pressure increase in each dump section compared to the baseline value, S_i is the pumping speed in each dump section and v is the velocity of the target particles. The velocity of the target particles is dependent on their state of matter. A complete description of the characteristics of internal targets employed within storage rings is given in reference [88].

Chapter 4

Vacuum Commissioning

4.1 Achieving XHV in CARME

XHV pressures are required for performing nuclear reactions studies on storage rings and achieving XHV represents one of the main challenges for such studies. The process of achieving XHV is complex and requires many different vacuum systems and procedures. The initial stage of the vacuum pump-down is the reduction in pressure from atmospheric pressure (1000 mbar) to approximately 1 mbar. In CARME, this is typically achieved after approximately 40 minutes. Turbo-molecular pumps are activated when the pressure is below 1 mbar. Pressures of $\sim 10^{-6}$ mbar are typically achieved following 24 hours of turbo pump operation in CARME. The decrease in the chamber pressure has been observed to be influenced by the vacuum conditioning of the chamber. When the chamber has recently been at a low vacuum pressure, the reduction in pressure has been quicker than when the chamber has been at atmospheric pressure for a significant amount of time. The decrease in pressure will take significantly longer or stall if vacuum leaks are present on the chamber. Leaks can be located in any of the large number of vacuum flanges on the CARME chamber. The wire seals between chamber sub-sections were found to be the most probable location of leaks during vacuum commissioning. Following approximately one week of turbo pump operation, the pressure in CARME is typically reduced to $\sim 10^{-8}$ mbar . To further reduce the pressure, the chamber is baked at $\sim$ 125°C for 1-2 weeks (see section 4.3). NEG pumps inside the chamber are activated at temperatures of 400-500°C near the end of the bake-out period. When the NEG pumps have been activated, the bake-out

temperature is slowly reduced back to room temperature. XHV pressures in CARME have typically been achieved several hours after the baking system has cooled to room temperature. The following sections in this chapter describe the vacuum commissioning of the CARME vacuum vessels and procedures used to achieve XHV. Further details of the vacuum commissioning process are given in the CARME technical paper [1].

4.2 Cleaning and vacuum firing

All components placed under high vacuum out-gas over time, and this contributes to the final vacuum level achievable. To reduce the out-gassing rate, components are cleaned and baked prior to installation. Cleaning is required as any contaminants will out-gas under vacuum and may contribute significantly to the vacuum level. The cleaning of components was conducted by the vacuum division at STFC Daresbury laboratory. The cleaning procedures utilised are outlined in reference [91]. To reduce the out-gassing from diffusion (see section 2.3.4) all components which could be, were vacuum fired. Vacuum firing is the process of baking at temperatures up to 950°C for 2-4 hours under vacuum ($<10^{-5}$ mbar). Heating to these temperatures increases the diffusion rate, and significantly reduces the number of molecules, primarily hydrogen, within the bulk material which can out-gas under vacuum. The interaction chamber and all vacuum flanges (excluding the signal feed-through flanges) were vacuum fired during commissioning at STFC Daresbury. Figure 4.1 shows the reduction in the out-gassing rate for all molecular species in RGA scans of the interaction chamber before and after vacuum firing. Components which could not be vacuum fired due to maximum temperature limitations, such as the cable harnesses, were vacuum baked at a lower temperature (approximately 200°C) for a several days.

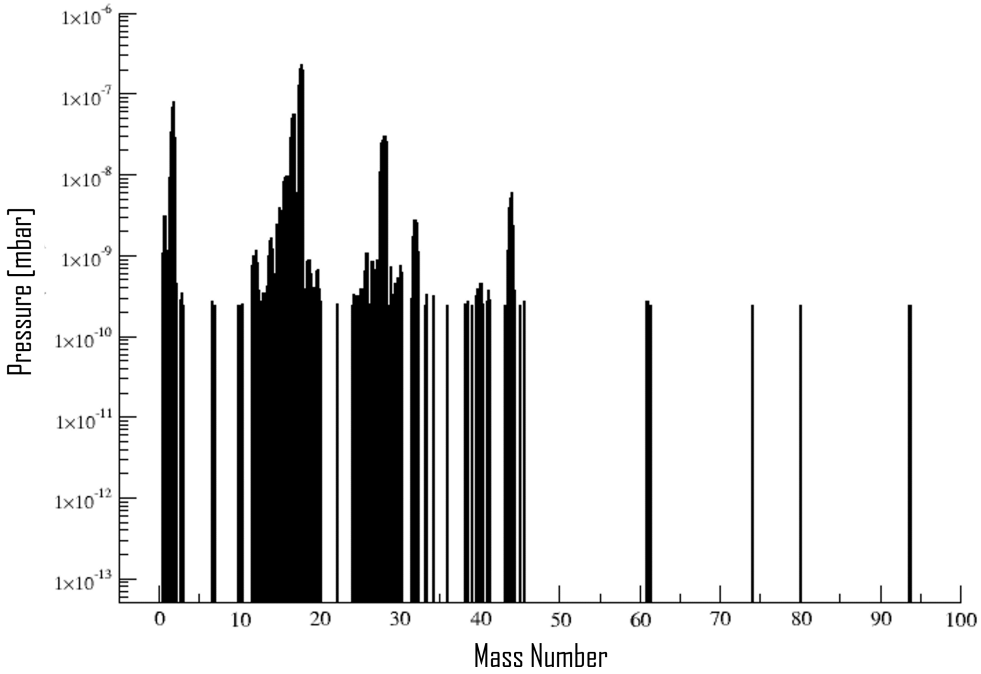

(a)

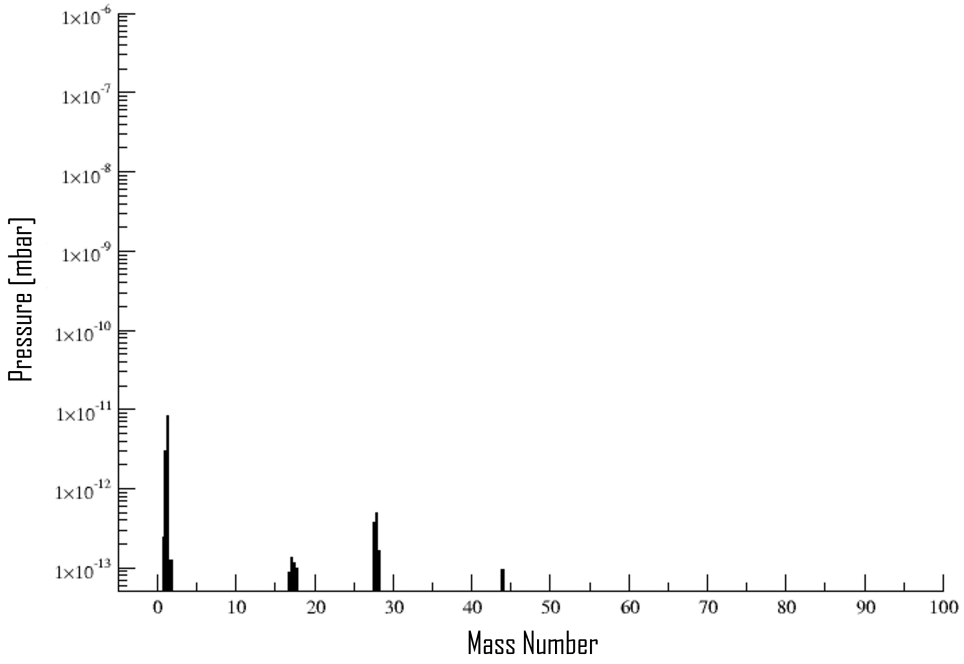

(b)

Figure 4.1: RGA scans of the interaction chamber pre (a) and post (b) vacuum firing. Vacuum firing consists of baking at temperatures up to 950°C for 2-4 hours under vacuum. The out-gassing of all molecules is significantly reduced post processing, with the out-gassing from many species below the sensitivity of the RGA probe. Out-gassing at a significantly reduced rate is still observable for H_2, N_2 and H_2O species.

4.3 Bakeout

Baking of the vacuum chamber during commissioning was conducted at pressures below 10^{-6} mbar range. The maximum temperature of the bake-out when detectors were installed in the chamber was limited to 125°C. The baking setup consists of a custom insulating jacket that encloses the CARME vacuum chamber and heating elements which are placed below the chamber. The air within the baking volume is heated to a temperature of 125°C by twelve ceramic heating elements with powers varying from 250 to 500 W for a total of 5 kW. The natural convection of the hot air within the baking volume acts to bake all parts of the chamber at a similar temperature, minimising thermal gradients. Large thermal gradients can produce thermal stresses, damaging vacuum seals leading to vacuum leaks. Due to the exponential temperature dependence of the out-gassing rate (see section 2.3.4), sections of the chamber baked at a lower temperature dominate the out-gassing rate of the chamber at room temperature. To maximise the effectiveness of the bake-out procedure, all parts of the chamber must therefore be baked at a similar temperature.

The insulating jacket is composed of multiple sections mounted above and below the chamber to completely enclose it. The insulating jacket partially mounted around the CARME detection chamber is shown in figure 4.2. The jacket is constructed of 10 mm thick fibreglass needle mat felt insulation within a polyurethane coated fibreglass cloth. An external layer of 0.45 mm aluminium coated fibreglass cloth provides further insulation. A final layer of thin aluminium metal sheets secures the insulating layers in place (see figure 4.2). Gaps in the insulating layers allow non bake-able equipment, in particular the motors and XHV vacuum valves, to protrude from the baking volume. The ceramic heating elements are placed below the chamber as shown in figure 4.3. Aluminium heat shields are placed on top of heating elements to shield the chamber from excessive temperature fluctuations. Heating elements operate as either on or off, with the status of the heaters controlled by a custom baking program. The program maintains and slowly ramps the temperature within the baking volume by a maximum of 7°C per hour in 1°C steps. Twenty K-type thermocouples are mounted around the baking volume and inside the chamber to monitor the temperature. Two of these thermocouples are set as control for the baking program. If the control temperature exceeds the temperature set point, the heating elements are turned off. If the control

temperature is below the set point, the heaters turn on. Several mechanisms prevent excess thermal gradients during bake-out. The temperature set point will not increase if any temperature reading is 10°C above or below the average temperature, or if the rate of temperature increase is above 7°C per hour. The baking program runs on a Raspberry Pi which can be remotely accessed to monitor and control the bake-out. A block diagram of the baking setup is shown in figure 4.3. Temperature readings from the thermocouples are relayed to the Raspberry Pi by two TC08 modules each capable of holding 8 thermocouples. RE-72 modules located outside the baking volume relay the program commands to the heating elements.

Testing of the baking setup was conducted in Edinburgh and STFC Daresbury. In Edinburgh the insulating capability of jacket was proven with temperatures up to 80°C achieved and maintained. The procedure to ramp the temperature was also determined. Increasing the temperature set point by 5°C produced excessive thermal gradients within the baking volume. A temperature increase of 1°C was determined to provide the greatest control of the bake-out temperature. Testing in Edinburgh consisted of only the insulating jacket, heaters and a small vacuum chamber. Subsequent testing at Daresbury was conducted with the CARME detection chamber. The thermodynamics within the baking volume were greatly affected by the introduction of the chamber. The chamber blocks direct heating of the upper baking volume. Efficient airflow and heat shields on top of the heating elements are required to linearly ramp the temperature and maintain thermodynamic equilibrium within the baking volume. Figure 4.4 shows the temperature plot for the Daresbury bake-out tests. Temperatures were able to be linearly increased with minimal thermal gradients across the chamber. A temperature of 140°C was achieved and maintained for 48 hours. The reduction in temperature following bake-out is not controlled by the bake-out program. The temperature set point is manually reduced and required testing to minimise thermal gradients. Temperature reductions between 5°C and 10°C were determined to be sufficient to minimise temperature gradients.

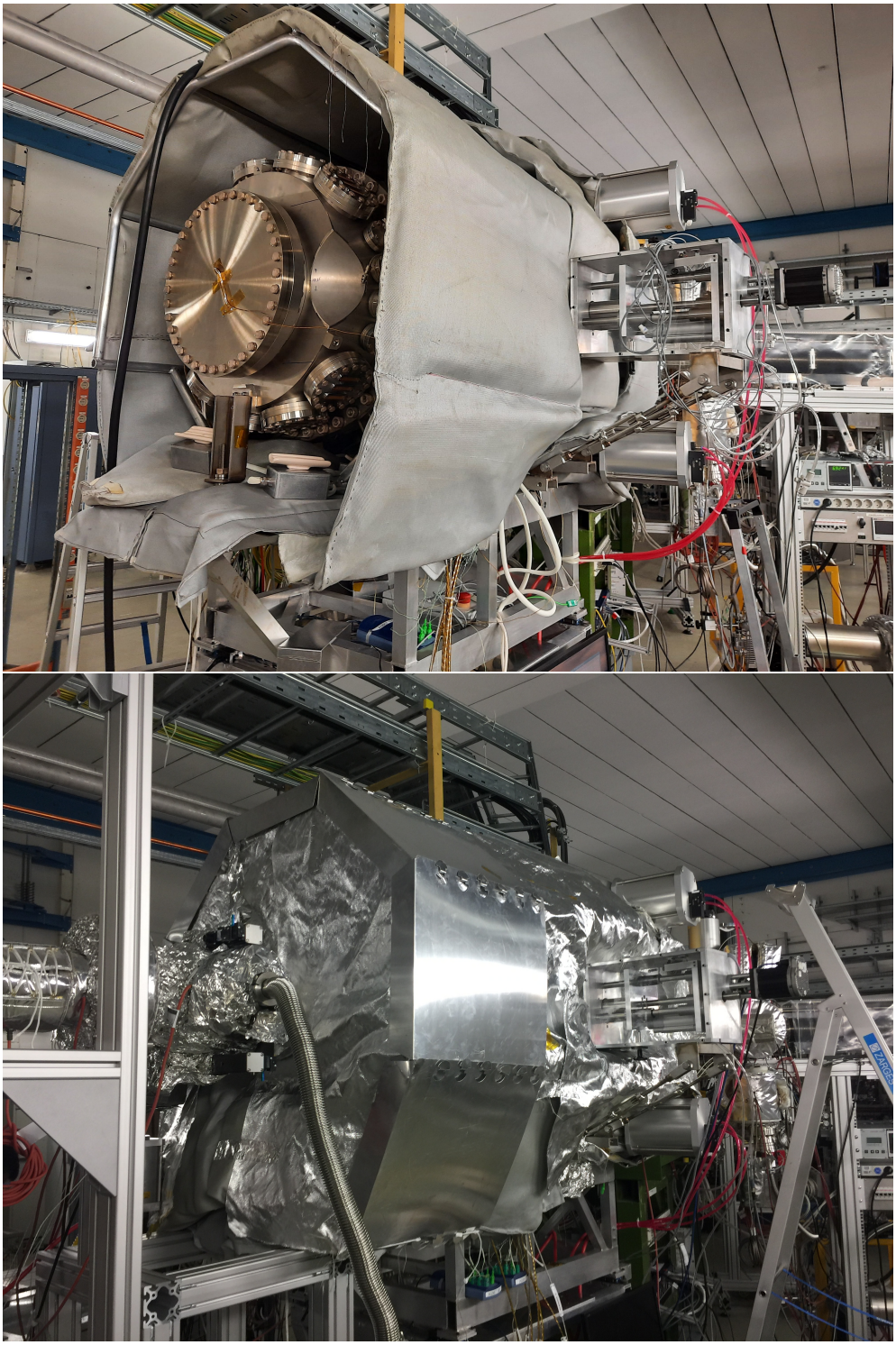

Figure 4.2: Image of the insulating jacket partially mounted around the CARME detection chamber at the CRYRING (top) and the full insulating jacket and aluminum outer shell mounted during XHV testing in the CRYRING (bottom). Ceramic heating elements provide the heating power to the baking volume. Non bakeable components (Motors and VAT vacuum valves) protrude from the baking volume.

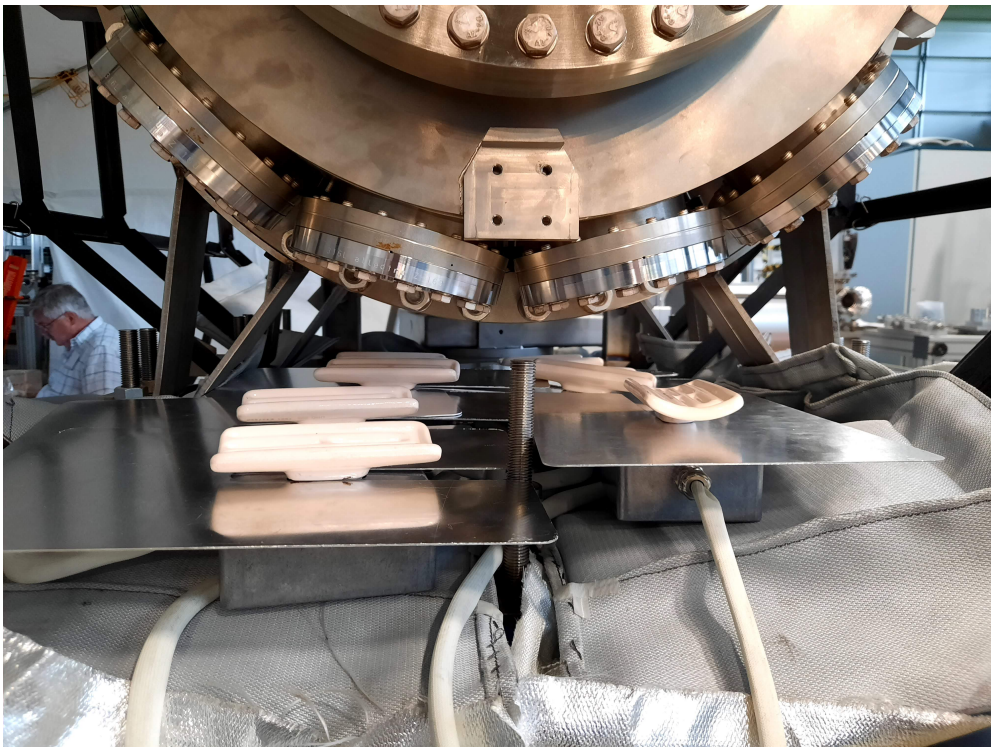

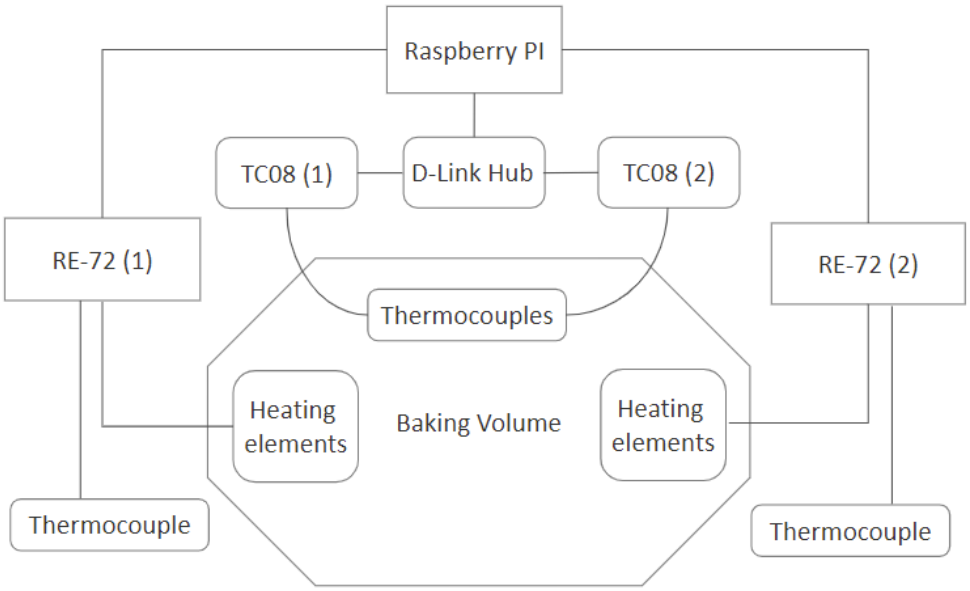

Figure 4.3: Image of the ceramic heating elements inside the baking volume (top). Thin stainless steel shields are placed on under the heating elements to insulate the bottom of the chamber and prevent damage to heating electrical components. Additional shields (not shown) can also be placed above the heating elements to prevent excess heating to bottom of the chamber. Block diagram of the baking setup (bottom). Components inside the baking volume are heated to temperatures up to 125°C

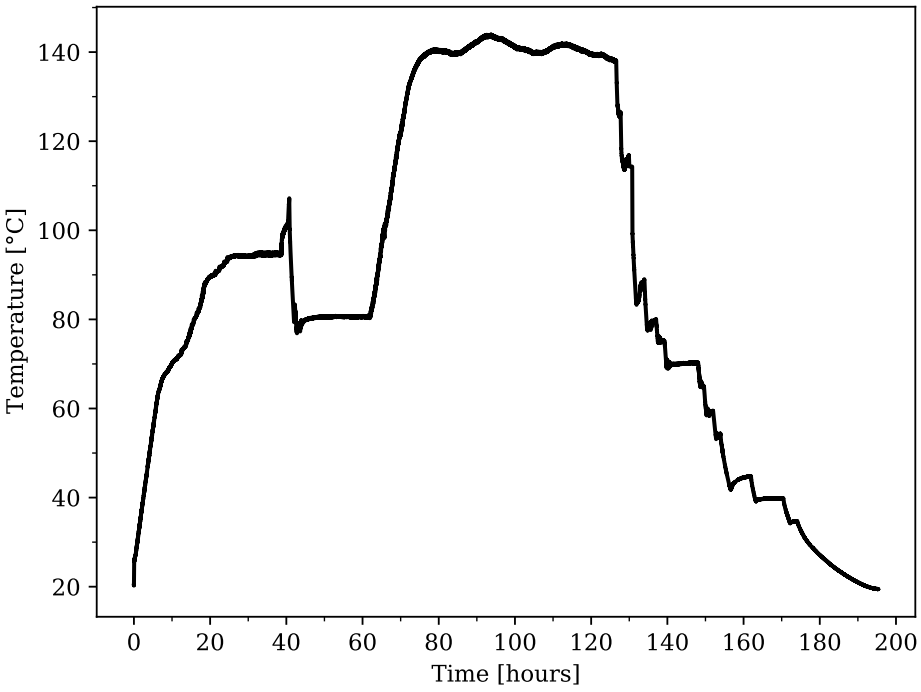

Figure 4.4: Temperature plot for initial bake-out testing conducted at Daresbury STFC. Temperature was linearly increased to ∼100°C. A bug in the baking code temporarily prevented an increase in the bake-out temperature before increasing to 140°C. Temperature was maintained for 48 hours before cooling.

4.4 XHV vacuum testing

4.4.1 Daresbury XHV testing

The procedures to achieve XHV vacuum conditions were tested at STFC Daresbury laboratory. All vacuum equipment (section 3.2.4) was installed on the CARME chamber, in addition to a leak detector and residual gas analyser (RGA) on the backing line. No other instrumentation or outgassing load was placed within the chamber volume. No thermo-couples to monitor internal temperatures were used in this phase of testing. The chamber was baked for two weeks at 140°C. NEG modules were activated after this baking period, in groups of 4-5 modules over a period of one week. The plot of the bake-out temperature and chamber pressure during and after the NEG activation procedure is shown in figure 4.5. The ion pressure gauge was not active until the activation procedure of the NEG modules. The large pressure increases at A, B and C show the staggered activation of NEG modules. The D2000 NEG modules have an in built thermo-couple and were activated at a temperature of 550°C (170 W power per

module). The UHV1400 NEG modules do not have an internal thermo-couple and were activated with a power of 200 W per module. NEG modules were held at half power following activation, to maintain the clean surface of the pumps, until time D in figure 4.5. The temperature set point in the baking program was maintained at 140°C throughout the NEG activation. The additional heating power of the NEG pumps increased the average chamber temperature to above 150°C during activation. Ion pumps were turned on in brief 30 second flashes during the cooling procedure. Once the chamber had cooled to room temperature an XHV pressure of 5×10^{-12} mbar was achieved. This pressure was maintained for several days before the system was re-pressurised with dry nitrogen for shipment to FAIR.

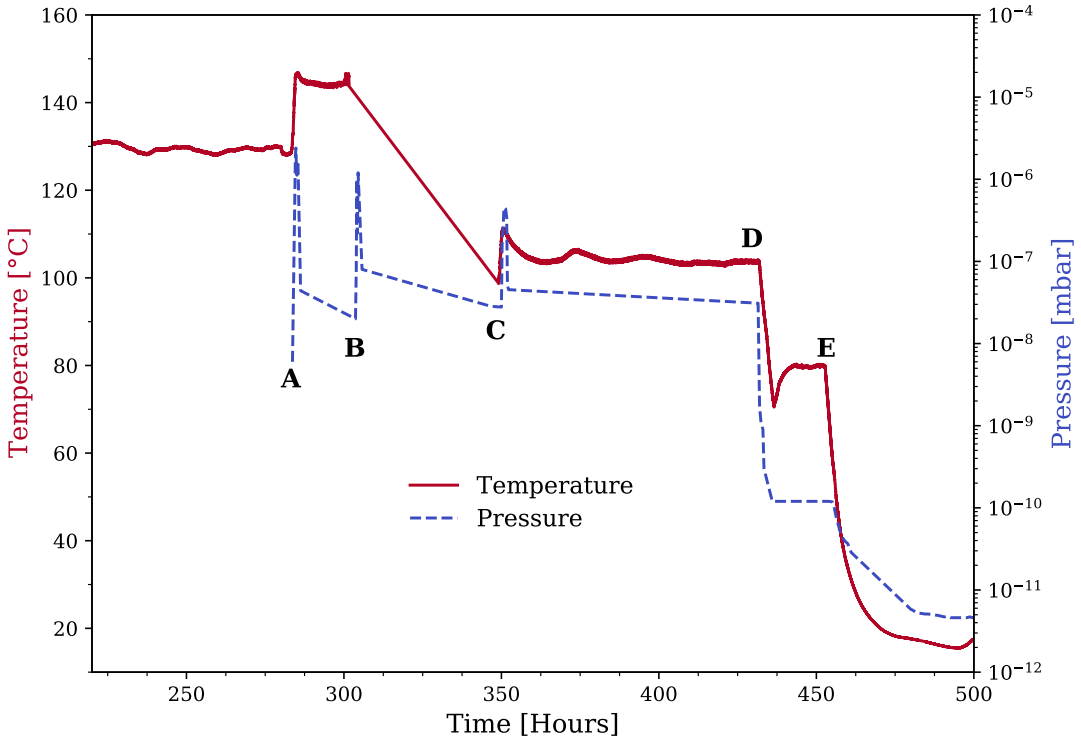

Figure 4.5: Bake-out temperature and chamber pressure plot against time during XHV commissioning with an empty vessel at STFC Daresbury. The temperature is taken as the average of all the chamber thermo-couples and the chamber pressure is read from the hot cathode gauge mounted on the chamber. The hot-cathode gauge was not active during bake-out before NEG activation. The chamber was baked for ∼280 hours before NEG activation. Activation of NEG modules (A,B,C) produces a significant pressure increase and an increase in the chamber temperature of ∼ 10°C. The temperature was reduced in two stages (D,E) after which a pressure of 5×10^{-12} mbar was achieved.

4.4.2 CRYRING XHV testing

The CARME detection chamber was installed on the CRYRING following vacuum testing at Daresbury. Vacuum testing was performed at CRYRING with a full vacuum load. All internal components (including the Kapton insulated cabling) excluding the silicon detectors were installed. Internal XHV compatible thermo-couples, one mounted to the Kapton insulated cabling and several others floating in the chamber, were used to monitor internal temperatures. The chamber was baked for a total of 8 days at a maximum temperature of 130°C. NEG modules were activated using the same procedure to the one used in Daresbury, with the baking temperature reduced to 110°C. The activation of NEG modules increased internal temperatures above 180°C. This temperature is far above the maximum temperature limit for the silicon detectors. Activation of the NEG modules was halted with alternate activation procedures tested to limit the internal temperatures. A plot of the internal temperature and the chamber pressure during the NEG activations is shown in figure 4.6. A, B and C correspond to the activation of different NEG modules at varying powers. Details of the NEG activation testing is given in reference [1]. The procedure determined for future activation of the NEG modules in CARME is outlined below.

- Activate the D2000 NEG modules individually at $\sim$ 400°C for 90 minutes
- Activate UHV1400 NEG modules one group (of two or three modules connected in series) at a time. UHV1400s close to the silicon detectors should be activated last.
- UHV1400s far from the detectors can be activated with power of 100-150 W per module and UHV1400s close to detectors can be activated with powers of 30-60 W of power per module.
- Power to NEG modules should be slowly increased to gauge the effect on internal temperatures.

Following the activation testing, the ion pumps were turned on and the temperature reduced by approximately 10°C per hour. A pressure of 9×10^{-12} mbar was achieved once the chamber had cooled to room temperature.

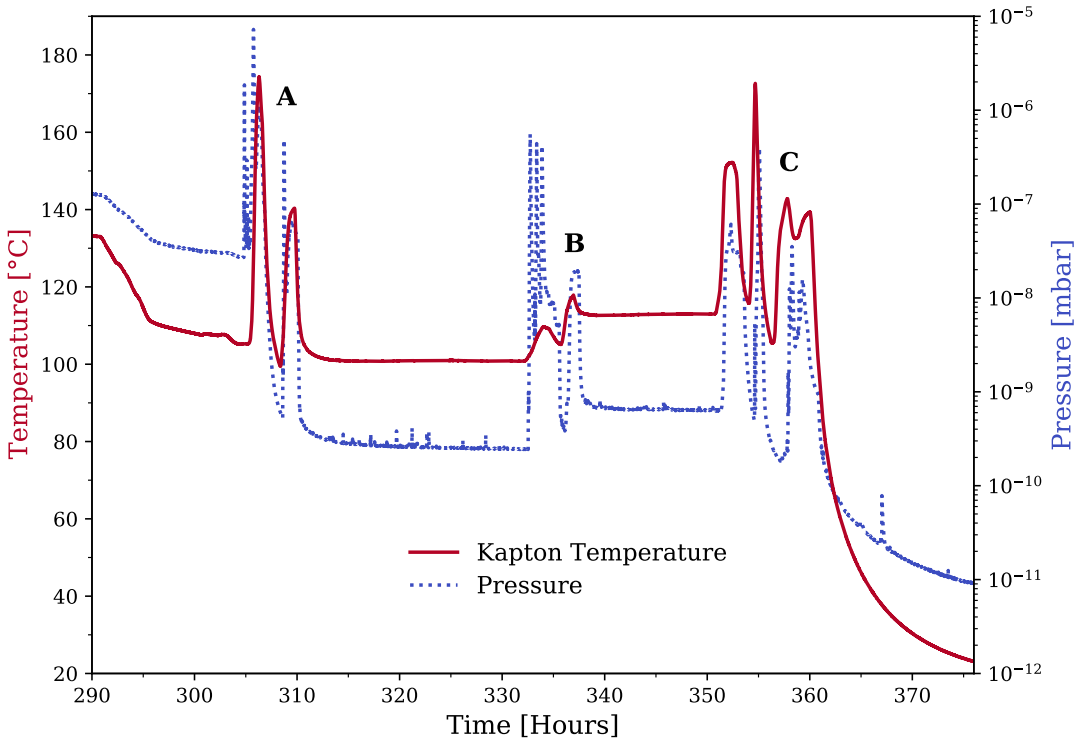

Figure 4.6: Plot of the chamber pressure (blue) and internal temperature of the Kapton cabling (red) during the activation testing of the NEG modules (no detectors inside the chamber). The initial activation of modules (A) produced temperatures above the maximum rating of the silicon detectors. B and C show the subsequent NEG activation testing. Following NEG activation, the chamber was cooled and a final pressure of 9×10^{-12} mbar was achieved.

4.5 CRYRING final vacuum

4.5.1 Achieving operational vacuum

The final pump down and bake-out cycle was performed following the installation of two silicon detectors in the chamber. Multiple heating wires wrapped around the body of the chamber provided the heating power for the bake-out due to an electrical fault in the CARME heating elements (see reference [1] for details). Each heating wire was independently controlled and could be set to individual temperature limits. Baking was not controlled by the automatic baking program during this bake-out cycle but temperatures were monitored using the program. Temperature set points were chosen to maintain a consistent temperature across the chamber. The chamber was baked at an average temperature of 125°C for approximately one week. The use of heating wire meant that heating of the chamber was not as evenly distributed as previous baking cycles. A plot of the temperature and pressure following the installation of all heating

elements is shown in figure 4.7. Temperature spikes (A,B,C) are caused by changes in the heating wire temperatures with pressure spikes responding to the temperature fluctuations. NEG modules were partially activated at a significantly lower temperature (150°C oppose to 500°C) midway through the baking period. Large increases in pressure are visible due to the initial activation of the NEG modules (D,E), but minimal affect on the temperature is observed. The full activation of the NEG modules (F,G) was performed using the procedure determined from the CRYRING XHV test. Following activation of NEG modules and cooling of the chamber, the final chamber pressure achieved was 3.5×10^{-11} mbar.

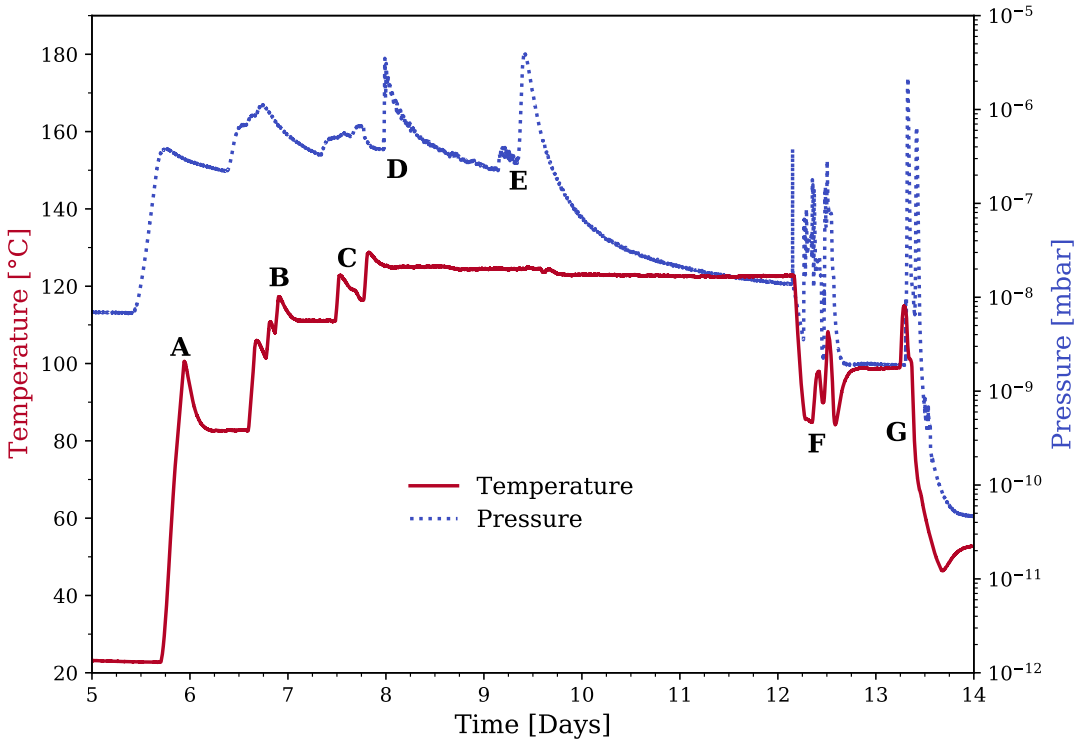

Figure 4.7: Temperature (red) and pressure (blue) plot for the bake-out cycle for which operational XHV was achieved. The plot shows the time from the fifth day, which is when consistent baking was achieved. The temperature was increased in steps (A,B,C) with initial NEG activation at points D and E. Final NEG activations were performed at F and G, afterwhich the chamber was cooled and a final pressure of 3.5×10^{-11} mbar was achieved.

4.5.2 Summary of vacuum commissioning

XHV pressures within the CARME chamber were produced with a full vacuum load and robust procedures for achieving XHV have been developed. The out-gassing rate of the chamber at XHV is estimated from the Daresbury XHV testing, using equation

2.8, to be approximately 4.5×10^{-12}mbar l/s cm^{-2}. This represents a total out-gassing load of $\leq 1.3\times10^{-7}$ mbar l/s. The out-gassing rate of the Kapton insulation was expected to be of the order of $\leq 1\times10^{-10}$ mbar l/s cm^{-2} [92, 93], representing a total outgassing load in CARME of $\leq 8\times10^{-7}$ mbar l/s. The pressure of 9×10^{-12} mbar achieved during the CRYRING XHV testing suggests a significantly lower out-gassing load of approximately 2.5×10^{-7} mbar l/s. The cleaning and baking procedures utilised, in addition to testing under XHV which has not previously been undertaken, may contribute to the lower outgassing rate of the Kapton cables. The final vacuum achieved with two detectors installed in CARME was above previous vacuum tests, however the production of vacuum was hampered by uneven heating of the chamber and very tight time constraints. Subsequent leak testing of the CARME and interaction chambers following the commissioning beam-time discovered several previously unknown leaks on the interaction chamber. These leaks were not found during installation due to the tight time constraints and are likely to have contributed to the higher vacuum pressure. It is expected pressures below 1×10^{-11} mbar will be achieved with detectors installed in the chamber with sufficient bake-out time, the use of the CARME heating elements and the removal of all vacuum leaks.

Chapter 5

Commissioning of CARME using ^{14}N(d, d)^{14}N Elastic Scattering

5.1 Commissioning introduction

The CARME array and the CRYRING gas-jet target were commissioned using a deuteron beam incident on a nitrogen gas target at beam energies of 1.5 MeV/u and 5.5 MeV/u. The commissioning and calibration of CARME primarily utilised the ^{14}N(d, d)^{14}N elastic scattering. This involved the energy calibration, detector position determination and separation of the different ring cycle phases. Only two of the four detectors that can be mounted in CARME were installed for the commissioning beam-time and only one of these, the top left detector in figure 3.5, was operational. However, this was sufficient to successfully commission the CARME array. This chapter describes this first experimental beam-time of the CARME array, in addition to the calibration and analysis procedures developed.

5.2 Operation of the gas-jet target

The CRYRING gas-jet target was first commissioned in the same experimental beam-time as CARME. A nitrogen target was used during the experimental beam-time. Hydrogen and helium targets were unable to be produced for the commissioning beam-time but will comprise the majority of the target species in future reaction measurements. The gas target is assumed to consist purely of ^{14}N due to the low natural abundance ($< 0.4\%$) of ^{15}N. The nitrogen gas, cooled to ~ 130 K, passed through the target nozzle producing the gas jet. The size of this jet in the interaction chamber was constrained to a diameter of ~ 1 mm by a series of four skimmers. After the interaction chamber, the gas-jet passes through three dump chamber sections where it was removed by several turbo-molecular pumps. A full description of the target setup is given in section 3.3.

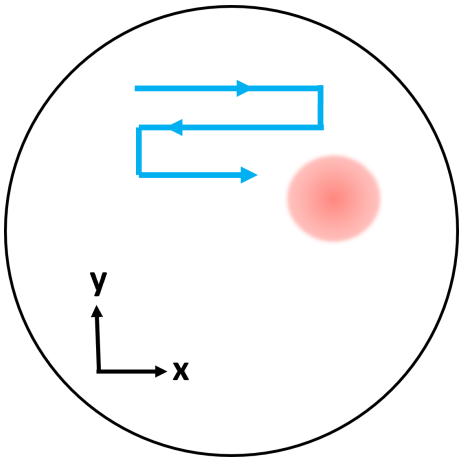

Figure 5.1: Schematic of the target inlet chamber with a top down view adapted from reference [88]. The nozzle was moved along the blue path until an increase in the pressure of the dump chambers was observed. The red region indicates the region where the nozzle is aligned with the skimmers.

To produce the target jet in the interaction chamber, the target nozzle required alignment with the skimmers in the inlet chamber. The target nozzle is mounted to a translator system to allow for movement in the x and y directions. To align the target nozzle, the position of the nozzle was scanned across the range of motion of the translator in small increments. When the nozzle was aligned, a large pressure increase was observed in the target inlet and dump chamber sections. Figure 5.1 shows a schematic with a top down view of the target inlet chamber. The nozzle was moved across the blue path until the nozzle was aligned. Small adjustments to the alignment of the target nozzle were required throughout the experimental period. Once sufficient target

densities were achieved, the ion beam was tuned to overlap with the target jet using the elastic scattering rate as a reference. The target density is calculated from the pressure in the target dump sections using equation 3.1

$$n = \frac{4}{\pi kT} \frac{1}{v\Delta x} \sum_{i=1}^{n} (S_{\mathrm{i}} \Delta p_{\mathrm{i}})$$

The target density throughout the experimental period is shown in figure 5.2.

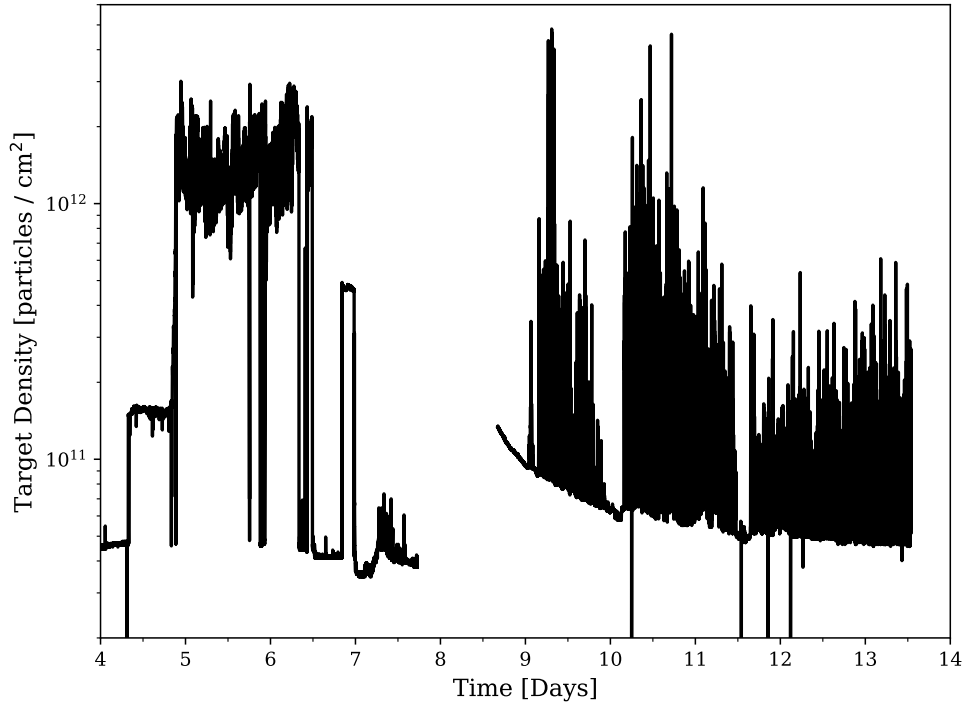

Figure 5.2: Plot of the target density throughout the experimental period. Target densities between 1×10^{11} and 1×10^{12} atoms/cm^2 were produced at periods throughout the experimental beam time. The target section was vented to atmosphere to remove a blockage within the target nozzle during the period not plotted around day 8.

The desired target density was at least 1×10^{12} atoms/cm^2. For the majority of the beam time, the target density was significantly below this. Large fluctuations in the target density were also observed throughout the beam-time, with fluctuations up to an order of magnitude observed within a single ring cycle. These issues were caused by blockages formed from frozen residual gases in the target nozzle. In order to minimise blockages and maximise the target density, the target was operated differently from the operation of the similar target setup used in the ESR. The recommended operating

temperature for a nitrogen target is $\sim$ 131-135 K. To increase the target density, the temperature was lowered to 95 K, with periodic increases to 125 K. The reduction in temperature facilitates the formation of clusters in the target jet (see section 3.3), which increases the target density. The periodic temperature increases were required to prevent the freezing of residual gases within the nozzle. Even so, blockages were a regular occurrence throughout the beam time. Blockages may also be the cause of the requirement to regularly re-align the target nozzle with the skimmers during the beam time. When blockages could not be removed following the procedure outlined above, the cryostat temperature was temporarily increased to 300 K to melt the frozen material. During days 6-9 (see figure 5.2), a blockage could not be removed by increasing the temperature. The blockage was physically removed from the nozzle, which required venting of the target setup and removal of the nozzle. The nozzle was then cleaned before re-installation in the target setup. A larger nozzle will be used for future measurements to prevent the formation of blockages.

In order to operate for a sustained period, gas from the target setup must not significantly increase the pressure in the ring. During the beam-time, sustained and significant pressure increases were observed. In the ring section CARME is installed, the pressure increased from $\sim 1\times10^{-11}$ mbar to $\sim 1\times10^{-10}$ mbar, and at one point above 1×10^{-9} mbar. This pressure increase triggered the closing of gate valves to the CARME ring section, temporarily halting the beam-time. The large pressure increase observed is due to insufficient pumping speed in the target section. To prevent significant pressure increases in future measurements, additional turbo-molecular pumps are to be installed in the target section. Furthermore, gate valves are to be installed on the target nozzle which only allow gas into the interaction chamber when beam is circulating in the ring. These improvements will prevent excessive pressure increases and enable higher target densities.

5.3 Testing and calibration using elastic scattering

5.3.1 Energy calibration

The energy calibration requires determination of the ADC offset and the gain for each DSSD strip. The ADC offset is the difference between ADC channel zero and the ADC channel which corresponds to an event of zero energy. The gain (keV/ch) is the ADC response to energy deposition, which is nominally 0.7 keV/ch. The ADC offset is determined by a pulser walk-through. A pulser walk-through involves the input of pulser signals with a precisely known ratio of amplitudes (see figure 5.3).

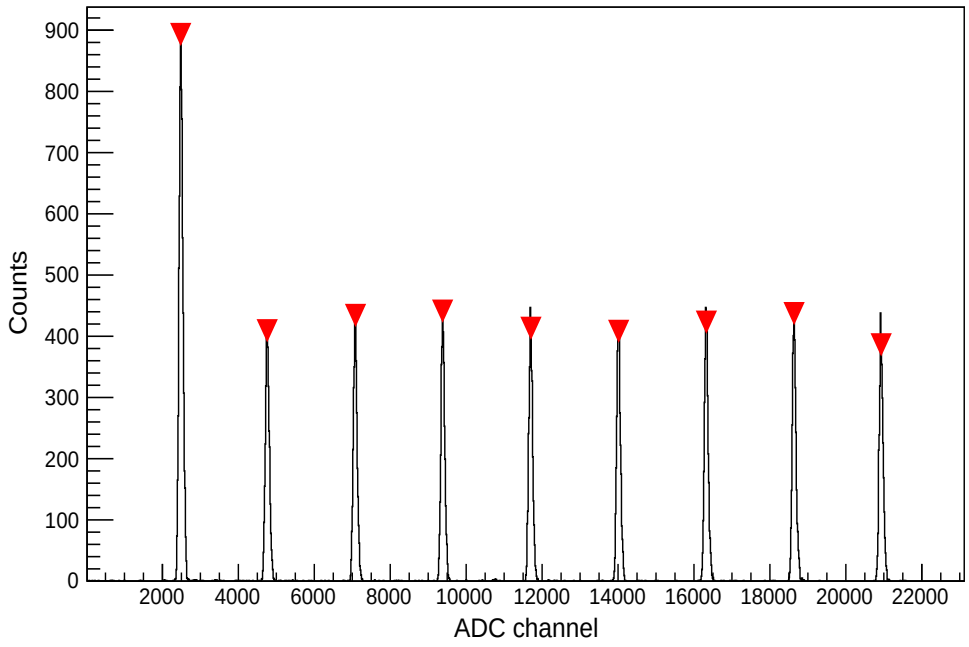

Figure 5.3: Plot of a pulser walk-through used to determine the ADC offset for one channel. The pulser peaks in black are input at a precisely known ratio of amplitudes. The red triangles represent the peak centroids which are used in a linear fit to determine the ADC offset

A linear fit is performed on the centroid positions of the peaks to determine the zero point offset for each channel. The gain is determined using a linear fit between the ADC offset and a peak of known energy. The Rutherford scattering peak for a beam energy of 1.5 MeV/u was used as the reference peak for the gain calibration. The scattering peak used in the calibration is shown in figure 5.4. The change in the energy of this peak across the $\sim$ 7 degree angular range of the detector is $\sim$ 5 keV. This is significantly below the energy resolution ($\sim$ 150 keV) so that the position of the pixels

was not required prior to the energy calibration. The poor energy resolution is the result of electronic noise in the system, which was not optimised due to time restraints during the installation phase. The Rutherford peak at a beam energy of 5.5 MeV/u was not used as a second known reference peak for the gain calibration due to a large number of missing y strips on the detector for those experimental runs. The missing strips during the higher beam energy runs is discussed in appendix A. To constrain the energy calibration at higher energies, a global linear fit was performed using the elastic scattering peak and the peak from alpha particles produced in the ^{14}N(d, α)^{12}C reaction to the first excited state (E_x = 4.44 MeV, see chapter 6).

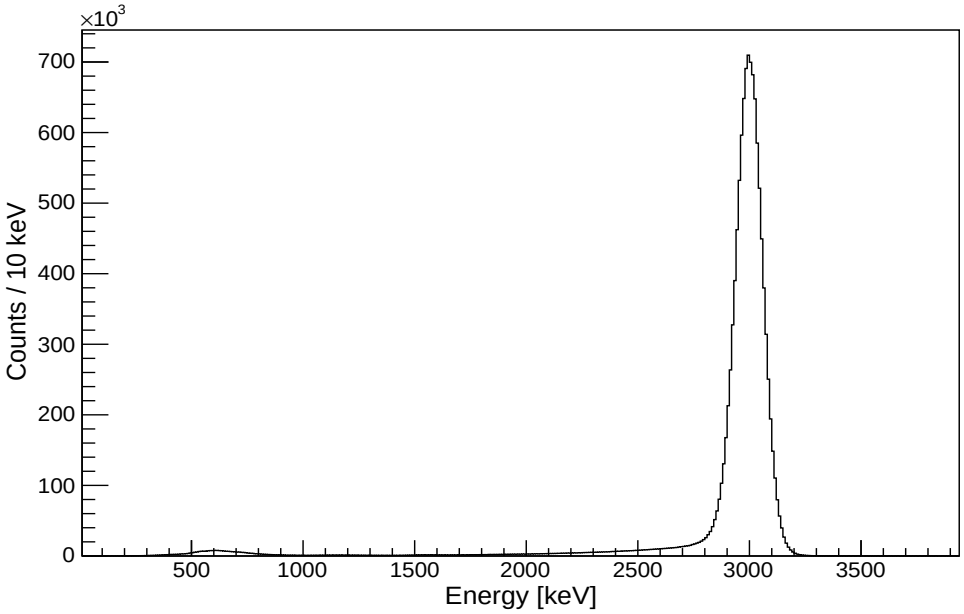

Figure 5.4: Energy histogram of events for all angles across the detector at a beam energy of 1.5 MeV/u. The Rutherford peak can be seen at 3 MeV. Rutherford scattering is the dominant process and accounts for the majority of detected events.

The energy of an event is determined for the front and back (x and y) of the DSSD. These energies are then matched, with events which have an energy difference between the front and back of the DSSD ($|E_y - E_x|$) greater than a set threshold discarded to remove noise events. This threshold is dependent on the energy resolution of the x and y strips. The mean energy width (full width half maximum) of the x and y strips was 180 keV and 140 keV respectively. As a result, a threshold of 200 keV was used for the energy matching procedure. The energy of an event would normally be taken as the average of the x and y energies. In order to not significantly reduce the energy resolution, the energy of the y strip was used as the energy of the event.

5.3.2 Normalisation of the differential cross section to Rutherford scattering

Rutherford scattering was the dominant process observed in this commissioning beamtime. In addition to aiding in the energy calibration, Rutherford scattering is used to normalise the differential cross section. The differential cross section for storage ring measurements is given by

$$\frac{d\sigma}{d\Omega} = \frac{\mathrm{N}_d}{\mathrm{N}_B \mathrm{N}_T \eta f_0 d\Omega} \tag{5.1}$$

where $\mathrm{N_d}$ is the number of detected particles across a solid angle of $\mathrm{d}\Omega$, N_B is the beam intensity, N_T is the number of target nuclei per unit area, η is the intrinsic detection efficiency and f_0 is the revolution frequency. The differential cross section can be simplified by combining the beam intensity, target density, revolution frequency and detection efficiency into a single normalisation parameter represented by α_n. The differential cross section can then be written as

$$\frac{d\sigma}{d\Omega} = \alpha_n \frac{\mathrm{N}_d}{d\Omega} \tag{5.2}$$

The differential cross section was calculated for discrete angular bins. The size and number of these bins is dependent on the total number of counts in the specific peak of interest. The majority of peaks contain $<<$ 100 counts, so that only one angular bin (the whole detector) was used in the analysis. Nearly 1000 counts were observed from the $^{14}\mathrm{N(d, p_5)}^{15}\mathrm{N}$ reaction (see chapter 6) so that five angular bins could be used in the analysis of this state. The normalisation parameter α_n is determined from the total number of Rutherford scattering counts across each angular bin by

$$\alpha_n = \frac{\mathrm{N}_{ruth}}{\mathrm{T}\, d\Omega \, \left(\frac{d\sigma}{d\Omega}\right)_{ruth}} \tag{5.3}$$

where N_{ruth} is the total number of Rutherford counts, $\left(\frac{d\sigma}{d\Omega}\right)_{ruth}$ is the Rutherford differential cross section, $\mathrm{d}\Omega$ is the total solid angle coverage and T is the total time.

The Rutherford scattering differential cross section in the centre of mass frame is given by the relation

$$\frac{d\sigma}{d\Omega} = \left(\frac{\mathrm{Z}_1 \, \mathrm{Z}_2 \, \alpha \, \hbar \, c}{4 \, \mathrm{E} \sin^2(\theta/2)} \right)^2 \tag{5.4}$$

where Z_1 and Z_2 are the atomic numbers of the incident and target nuclei, α is the fine structure constant ($\sim$1/137), $\hbar c \sim 197$ MeV·fm, E is the kinetic energy of the incident particle, and θ is the deflection angle. The Rutherford scattering peak can be seen at 3 MeV in an energy histogram of all events in figure 5.4. The high angular dependence of the Rutherford scattering angular distribution can be seen in the count rate across the detector in figure 5.5.

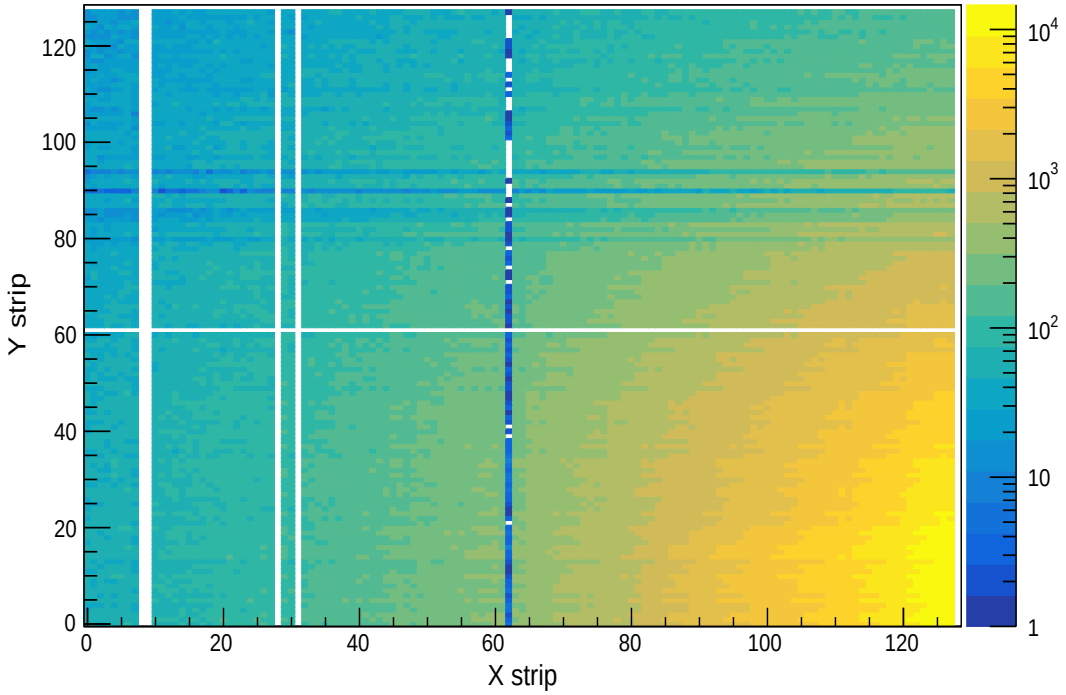

Figure 5.5: Histogram of the number of events per pixel across the detector for events in the Rutherford peak (2800 $\leq$ E $\leq$ 3200 keV). The bottom right of the detector (y strip 0 and x strip 128) is closest to the beam.

The uncertainty in the normalisation parameter is from the uncertainty on the number of Rutherford counts, estimated as $\sqrt{N_{ruth}}$, and from the uncertainty in the position of the detector. The uncertainty in the detector position is determined in section 5.3.3.

The uncertainty resulting from the detector position dominates for angular bins close to the beam due to the high angular dependence of the Rutherford scattering cross

section and high number of counts. For angular bins far from the beam, the number of Rutherford counts is lower and the uncertainty in the number of counts dominates. The total uncertainty of the normalisation parameter for all experimental runs was below 2%, with uncertainties as low as 0.15% for runs with a well defined detector position and a high number of counts.

The solid angle coverage is determined by the number of active detector pixels and the position of those pixels on the detector. The number of pixels in each angular bin is not constant across the detector and is dependent on the detector position. The pixel coverage for different angular bins when the detector was positioned 33 mm from the beam is shown in figure 5.6. The solid angle coverage per pixel is also not constant across the detector. Pixels at larger angles cover less solid angle than those at lower angles. The solid angle is therefore calculated for each pixel on the detector.

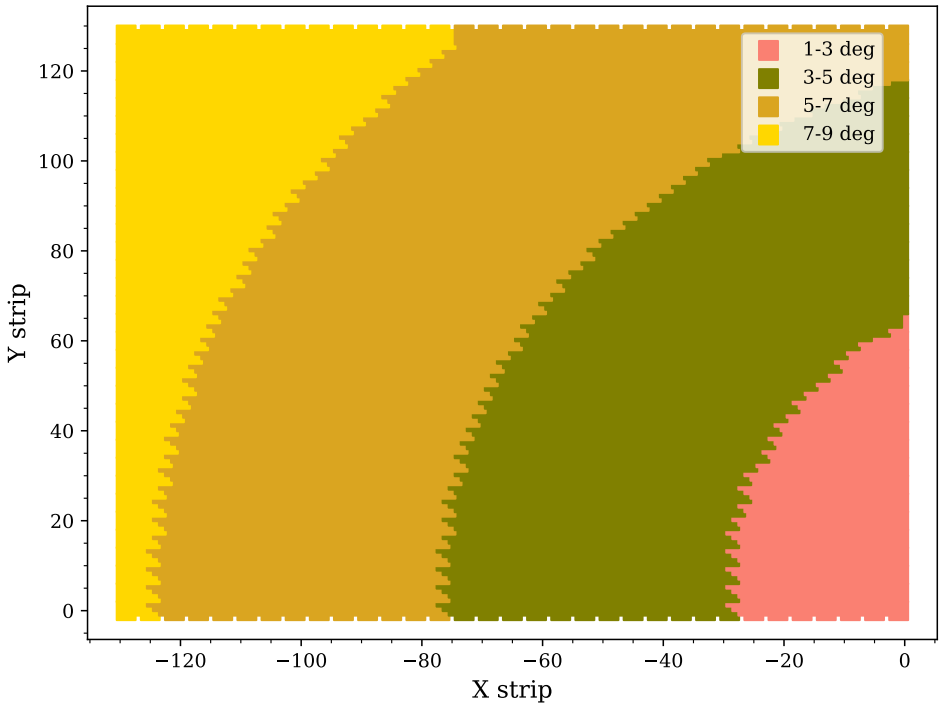

Figure 5.6: Plot of the pixel coverage per angular bin on the detector when positioned 33 mm from the beam. The colour of each pixel indicates the angular range the pixel falls within. The majority of pixels fall within the angular range 5-7 degrees (lab), while few pixels are within the angular range 1-3 degrees (lab). The pixel coverage is dependent on the detector position and requires calculation for each experimental run

Due to the large distance between the detector and the interaction point (> 1 metre) and the small size of each pixel (< 1 mm), the solid angle coverage of each pixel can be approximated by

$$d\Omega = \frac{dA}{R^2 + Z^2} \tag{5.5}$$

where dA is the area of the pixel, R is the distance of the pixel from the beam which is calculated from its x and y coordinates on the detector, and Z is the distance from the detector from the interaction point. All pixels in an angular bin are then summed together to give the total solid angle coverage.

5.3.3 Position calibration

The beam interacts with the target in the interaction chamber approximately 1 metre from the moving detectors, but the position of the detectors relative to this interaction point is not known. A graphic of the CARME moving detectors, location of the beam and the relative x, y, z directions is shown in figure 5.7.

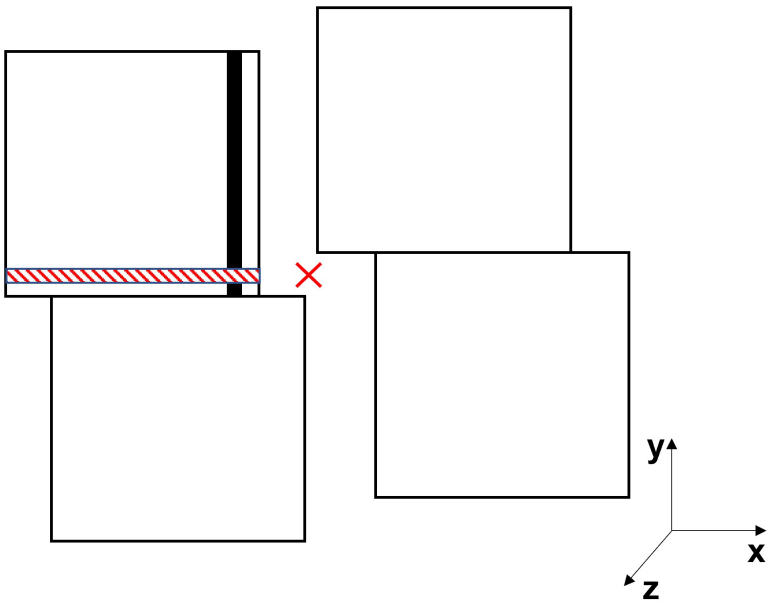

Figure 5.7: Sketch of the four moving DSSDs in CARME. The beam goes through the gap left by the detectors (red cross). Single y (red stripe) and x (black) strips are highlighted in the functional (top left) detector currently mounted in CARME. The Rutherford count rate across the strips close to the x and y strips highlighted in the figure are used to determine the position of the detector.

The detectors can move in the x direction. The relative x position of the detectors is measured by a string potentiometer, but the absolute distance of the detectors from the circulating beam, which may move between experimental runs due to beam focusing, is not known. The y and z positions are constant and determined by mechanical mounting constraints. The CARME detectors have high angular resolution due to the high segmentation of the DSSD and distance from the interaction point. The high angular resolution and the well known, highly angular dependent Rutherford scattering rate provides a robust method to determine the detector position in the x and y plane. The z position can then be determined using a peak of known angle once the x and y positions have been determined. The position of the functional detector was determined for each experimental run as part of the commissioning process.

X position

The Rutherford count rate in each pixel across a single y strip (e.g. the red strip in figure 5.7) is used to determine the x position of the detector from the beam. The energy of the events considered for the calibration is limited to only those inside the Rutherford peak ($2800 \leq \mathrm{E} \leq 3200$ keV). The y strips which are approximately level (in y) with the beam are used, so that any variance in the pixel angle is from the x direction. At the distance of the detectors from the interaction point ($\sim$1 metre) each strip covers an angle of $\sim$0.04 degrees (lab). The Rutherford scattering angular distribution is used as a fitting function for the total number of counts across the strip. Fitting is performed for a range of detector positions, with the χ^2 variable calculated for each fit. The detector position is determined by finding the fitting function which best describes the experimental data (where χ^2 is minimised). Figure 5.8 shows the Rutherford fitting function to the experimental data for the optimal detector position (a) and the χ^2 plot (b). The uncertainty in the detector position is estimated by the position change at ${\chi^2}_{\mathrm{min}} + 1$. The uncertainty for each strip is dependent on the number of counts across the strip. Experimental runs where the total number of counts across the strip is $>$ 100,000 yield an uncertainty of $\sim$0.2 mm per strip. Runs where the total number of counts is $\sim$10,000 yield an uncertainty of $\sim$1 mm per strip.

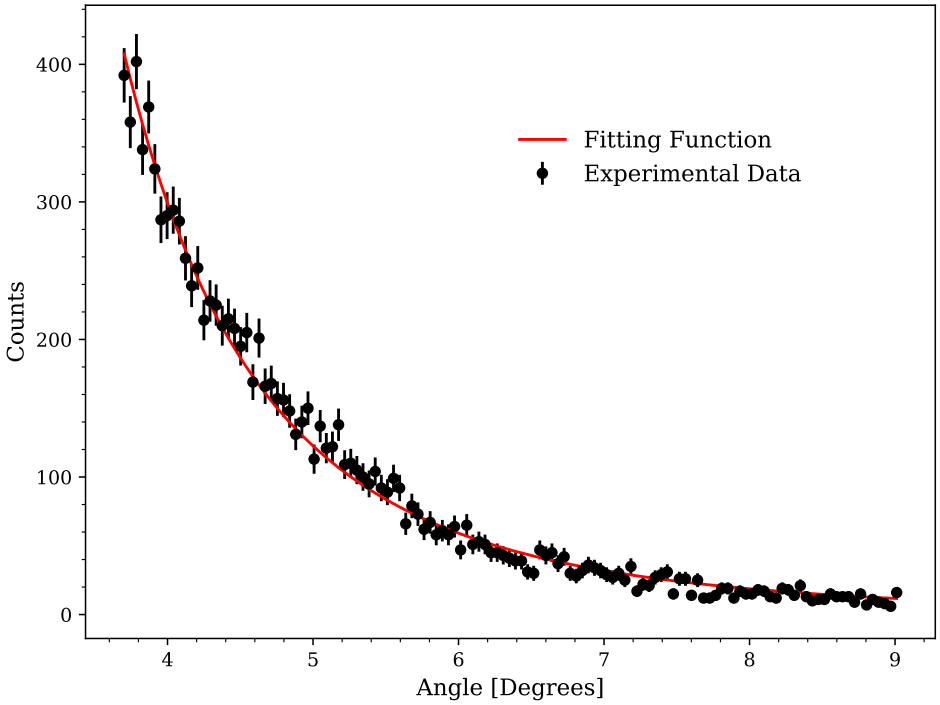

(a)

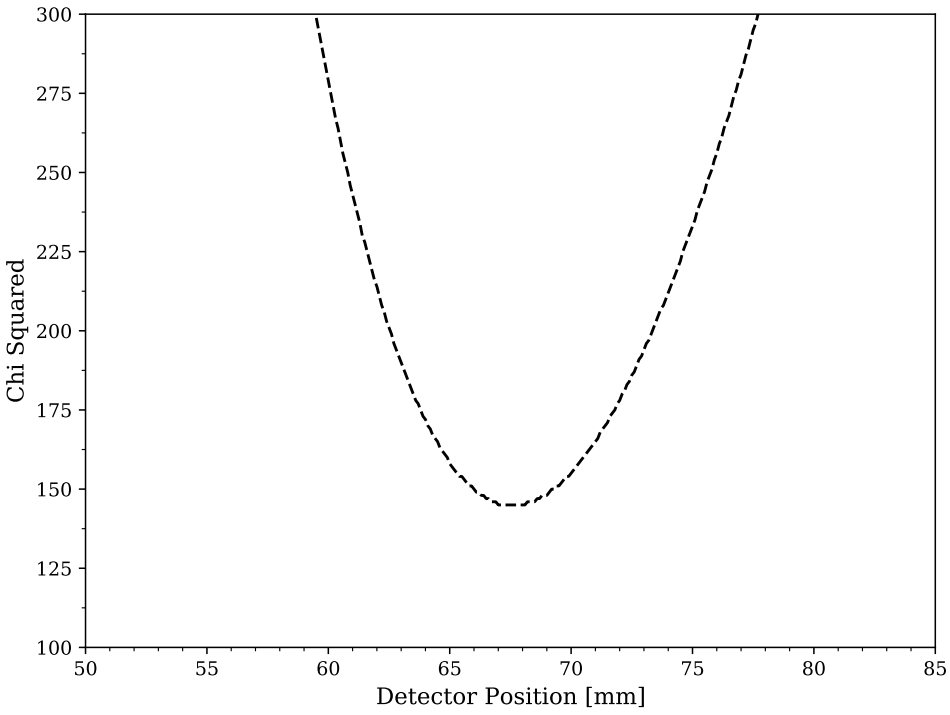

(b)

Figure 5.8: The top plot (a) shows the number of counts in the Rutherford peak ($2800 \leq \mathrm{E} \leq 3200$ keV) across a single y strip. In red is the Rutherford fitting function when χ^2 is minimised. The bottom plot (b) shows the χ^2 variable for fitting functions using different detector positions. The detector position is determined by the position where χ^2 is minimised.

This procedure is performed for the five y strips closest to where the detector is level with the beam in y. The final position and uncertainty are calculated using the weighted average of all five strips. The calculated x positions for each run were consistent with the potentiometer measurements between different experimental runs within < 5 mm. Differences between the position determined from the Rutherford scattering and the potentiometer values, outside of the calculated uncertainties, are likely from changes in the beam position for different experimental runs.

Y position

The detector position is offset from the centre of the CARME chamber. In design drawings the offset is approximately 7 mm. This offset results in an expected maximum in the Rutherford scattering distribution for the y strip which is level with the beam. Figure 5.9 shows the total number of counts for the y strips across the detector (black) and the expected Rutherford distribution calculated using the x position determined in the previous section and assuming the y position is the same as in design drawings (red). Note the red curve is **not** fit to the experimental data. The experimental data shows significant fluctuations in the number of counts across the y strips. This is not observed in the number of counts across the x strips. Issues with the y strips were apparent throughout the experimental beam-time and are explored further in appendix A. The expected Rutherford distribution is consistent with the experimental data for the majority of the y strips. The y strips corresponding to the maximum number of counts in the experimental data (y strips 5-15) is consistent with the expected Rutherford distribution. The maxima in the number of counts is consistent for all experiment runs, such that the interaction point is not thought to vary significantly in y. The y position of the detector used in calculations of the angle of events is that of the design drawings.

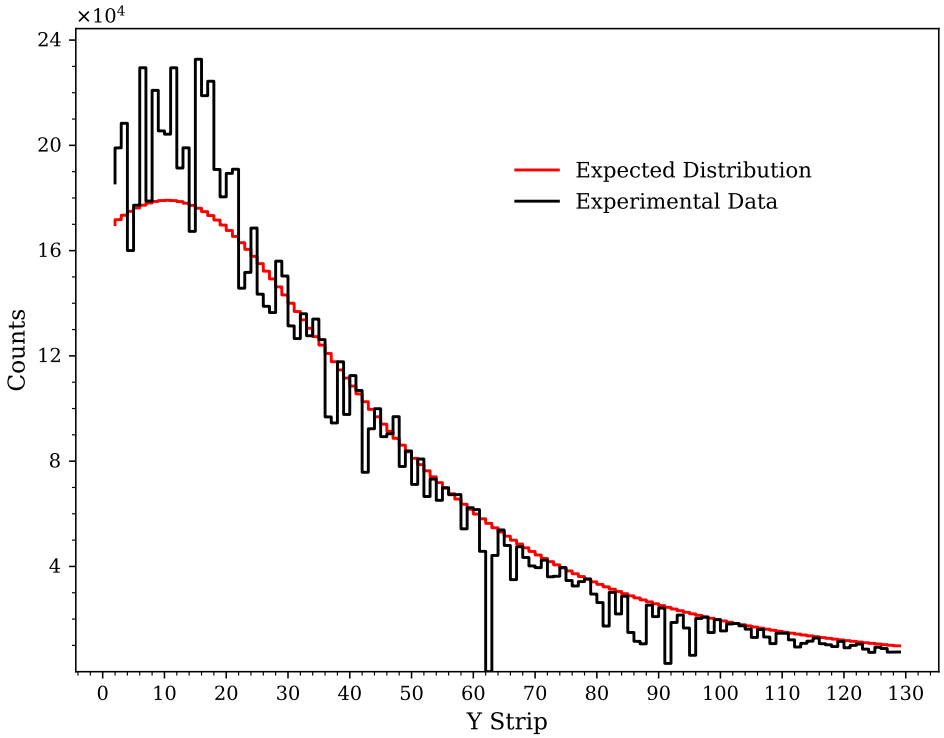

Figure 5.9: Plot of the number of counts in the Rutherford peak ($2800 \leq E \leq 3200$ keV) across the y direction on the detector. In red is the expected Rutherford distribution calculated using the x position determined in the previous section and the y position in design drawings. This distribution is not fit to the experimental data. The detector is positioned in the chamber so that it is offset from the centre of the chamber (by 7 mm in design drawings). This offset leads to a maximum in the Rutherford distribution at the centre point of the chamber. The observed maximum in the experimental data (strips 5-15) is consistent with the offset in the design drawings of 7 mm.

Z position

The z position (distance between the target and the detectors) could not be determined experimentally in this beam-time. Future measurements which will primarily be performed in inverse kinematics, could use the well defined maximum emission angle of forward focused recoil particles from the reaction to constrain the z position experimentally. In this work, the z position is taken from design drawings and is 1056 mm. The uncertainty in the z position is directly proportional to the uncertainty in the angle of the detected events. Due to the large distance between the detectors and the position of the target (> 1 m), the difference between the design drawings and the actual distance on the ring would have to be several centimetres to present a significant uncertainty. This level of difference is mechanically unrealistic, and the uncertainty in the z position is not considered further.

5.4 Phases of the ring cycle

The storage ring operational cycle consists of four distinct phases; beam injection, electron cooling, interaction between the cooled beam and the target and dumping of the beam (where the beam no longer circulates around the ring). The detectors move in response to the ring cycle phases. During the beam injection and cooling phases, the detectors are held at a position far from the circulating beam. When the beam has been cooled, the detectors move closer to the beam for the measurement to be performed. When the beam is to be dumped from the ring, the detectors are moved back away from the circulating beam. A signal is sent to the data acquisition system whenever the detectors begin or stop moving. This results in four movement signals for each ring cycle. Figure 5.10 shows these signals from the detector movement for the end of one cycle and the beginning of the next cycle. These signals allow for accurate separation of each phase of the ring cycle.

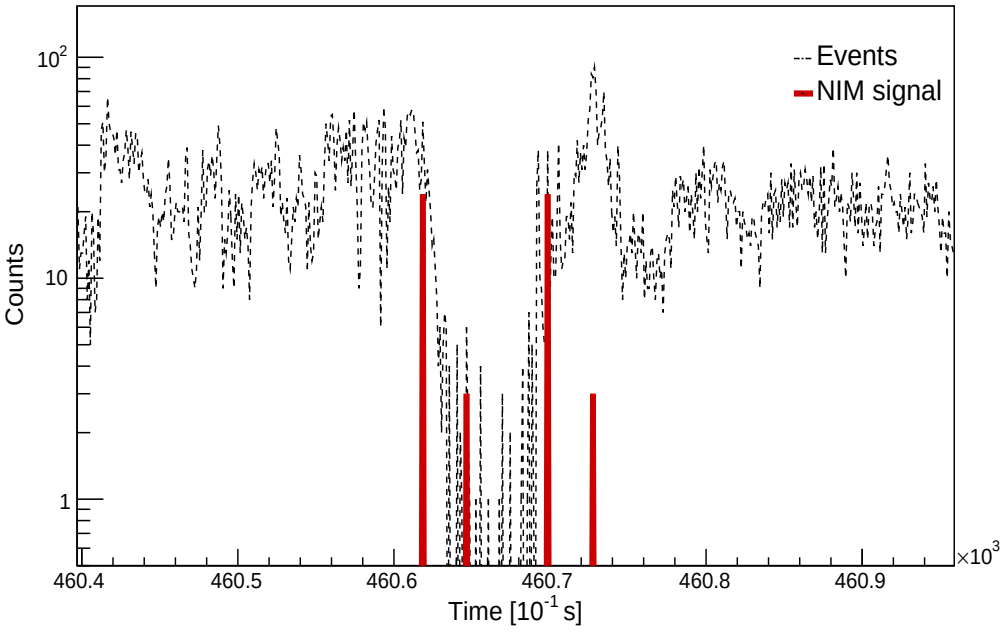

Figure 5.10: Plot of the count rate (black) against time for a time period in-between two ring cycles. The four signals (red) are input into the DAQ when the detector begins/stops movement. The first two signals correspond to the start and stop of the movement away from the beam. The third and fourth signals correspond to the start and stop of the movement towards the beam. Only events when the detector is static, and cooled beam is incident on the target are considered for analysis. This corresponds to the period before the first signal and after the fourth signal.

Separation of the ring phases is required to consider only the time period when a cooled beam is incident on the target. The process of separating the runs into distinct time

periods was complicated by the loss of some of the signals throughout the beam-time. The signals were generated by the motor system, but not always recorded by the DAQ. The signal that corresponds to the start of the detector movement towards the beam was always recorded in the DAQ. The time periods of each phase of the ring cycle are consistent throughout an experimental run, which coupled with the start of movement signal, allowed effective separation of each time period. Signals were only generated when the detector was moving. Therefore, for experimental runs where the detector was static, a different method for separation of the ring phases was required. An effective gauge of the ring cycle available for when the detector was static is the Rutherford scattering rate. Only when the beam is incident on the target will Rutherford scattering be observed. A noise spike is also observed when beam is injected into the ring which was also used as a reference point. The Rutherford scattering rate, coupled with the regular time period for the ring cycle provided a robust method for separation of the different ring phases. However, this method relied on a Rutherford scattering rate significantly above the background level. If the Rutherford scattering rate was similar to the background level, the different ring phases were unable to be separated. Several time periods were discarded due to an insufficient Rutherford scattering rate to effectively separate the ring phases.

The structure of events in the ring cycle for experimental runs where the detector was moving and where the detector was static are shown in figure 5.11. The x axis corresponds to the time in the ring cycle each event was detected, while the y axis corresponds to the energy of the event. The total time of the ring cycle for both runs was approximately 70 seconds. The first 2.5 s of the ring cycle corresponds to movement of the detector towards the beam in the moving detector run, and cooling of the beam in the static detector run. The time period between approximately 2.5 and 60 s corresponds to the measurement period where cooled beam is incident on the target. The detector is stationary in both runs during this period. The beam is dumped from the ring after approximately 60 s before re-injection 5-10 s later depending on whether the detector was static or moving. Low energy noise (< 1 MeV) is observed at times of the detector movement (0 s and 60 s) and at the point of beam injection and during the beam cooling phase (0 s and 70 s). High energy events (> 3 MeV) are observed in both the static and moving runs when the beam is dumped from the ring at ~ 60 s.

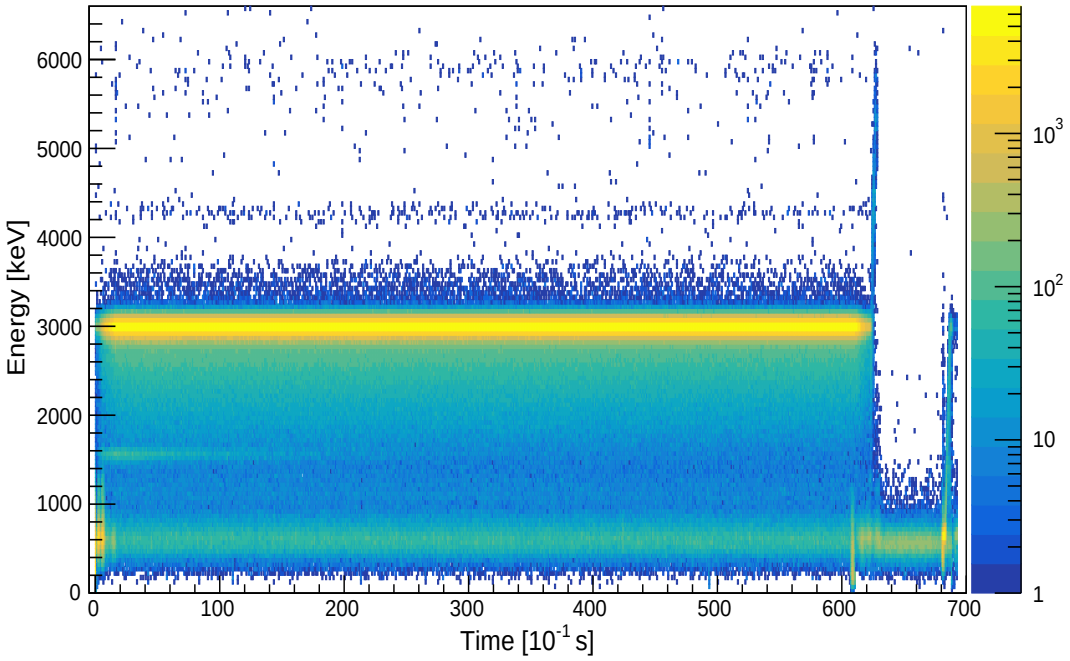

(a)

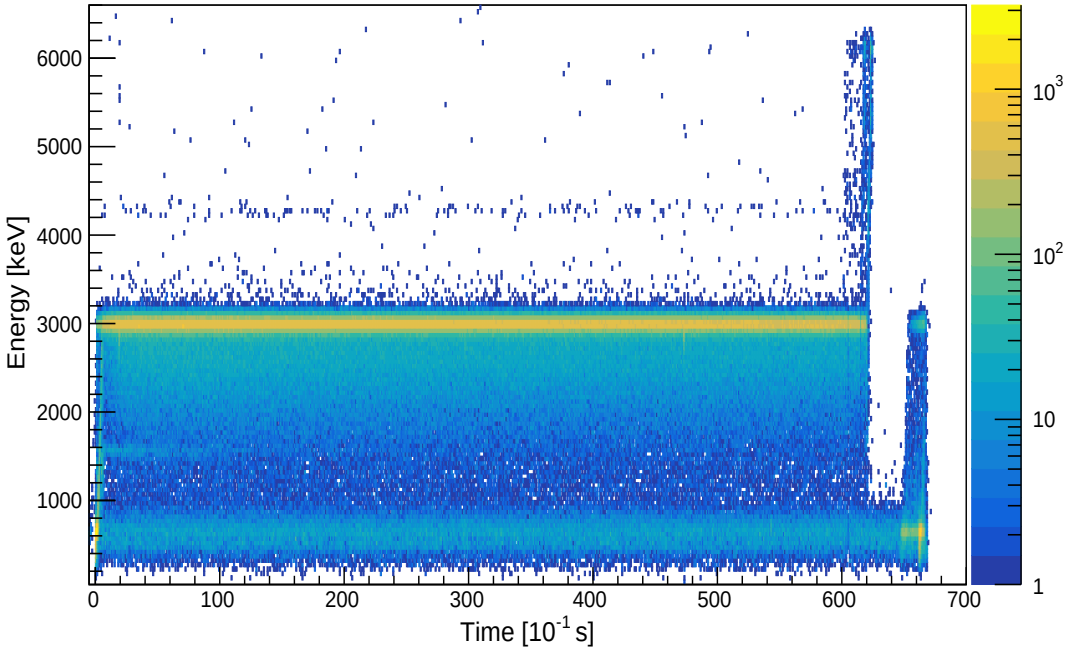

(b)

Figure 5.11: Energy against time plot for experimental runs where the detector moves in and out of the beam axis at the start and end of each ring cycle (a) and where the detector is stationary throughout the run (b). The histograms contain all events from the respective runs, with the x axis corresponding to the time in the ring cycle the event occurred. In (a), t=0 is when the detector begins moving towards the beam. In (b), t=0 is when the beam is being cooled. The time period between approximately 2.5 and 60 s corresponds to the measurement period where the detector is stationary and cooled beam is incident on the target. The beam is dumped from the ring at $\sim$ 60 s before re-injection 5-10 s later.

Energy spectra for the separated periods in the moving detector experimental run are shown in figure 5.12 for the periods where the detector was static and figure 5.13 for the periods where the detector was moving. In figure 5.12, the period where the beam was circulating in the ring, which comprises $\sim$ 60 s per cycle, is shown in black and when the beam is not circulating, which comprises $\sim$ 5 s per cycle is shown in red. In figure 5.13, the period where the detector is moving in towards the beam is shown in blue, and the period where the detector is moving out away from the beam is shown in green. Both movement phases occur for $\sim$ 2.5 s per ring cycle.

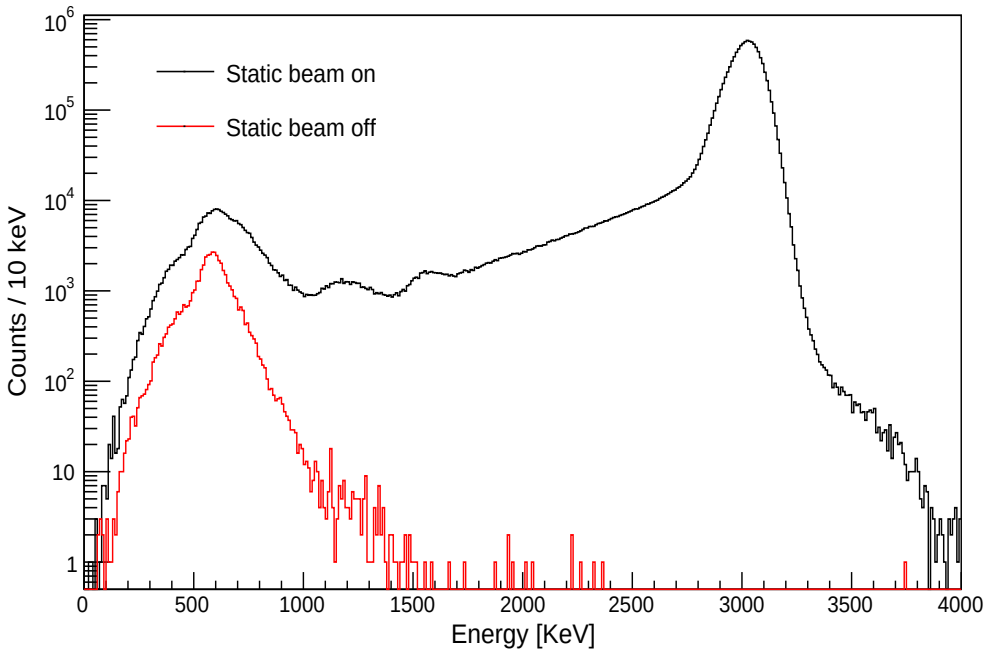

Figure 5.12: Energy spectra for separated periods within the ring cycle for a moving detector experimental run. This experimental run is the same as shown in the top plot in figure 5.11. The black plot corresponds to the period where the detector is static and beam is circulating in the ring ($\sim$ 60 s per cycle), the red plot corresponds to the period where the detector is static and beam is not in the ring ($\sim$ 5 s per cycle). The plot contains 1040 ring cycles in total.

The broad, low energy, electronic noise peak at $\sim$ 600 keV is common to all ring phases and appears across all detector strips. A smaller noise peak at $\sim$ 1200 keV is also visible in all ring phases. The source of this noise is a single strip on the edge of the detector. A peak at $\sim$1500 keV is also visible for early phases in the ring cycle (moving in and static beam on) but not in later phases. The time dependence of this peak can be seen in figure 5.11, as the number of events decreases over time. The mechanism

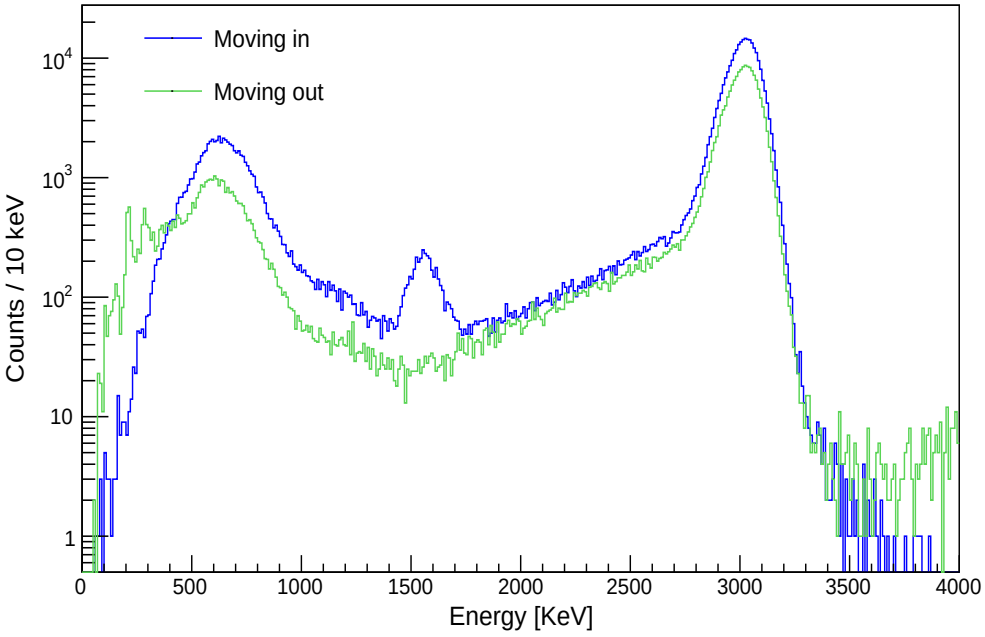

Figure 5.13: Energy spectra for separated periods within the ring cycle for a moving detector experimental run. This experimental run is the same as shown in the top plot in figure 5.11. The blue plot corresponds to the period where the detector was moving in towards the beam ($\sim$ 2.5 s per cycle), and the green plot corresponds to the period where the detector was moving out away from the beam ($\sim$ 2.5 s per cycle). The plot contains 1040 ring cycles in total.

for the production of events in this peak is not known, but the events are limited to 10 y strips on the edge of the detector so are likely the result of electronic noise. The Rutherford scattering peak at 3 MeV is only observed for periods where the beam is in the ring. The magnitude of the scattering, when normalised in time, is similar for all ring phases. The scattering peak is slightly lower in the moving out phase as the beam is dumped from the ring during this period. The number of events in the tail of the Rutherford peak, energies $\lessapprox$ 2800 keV, is greater than expected from purely Rutherford scattering. A continuum of non-Rutherford events is observed across the majority of the detector. This continuum is explored further in the next section.

5.5 Continuum of events below the elastic peak

The continuum of events below the elastic peak is observed in all the 1.5 MeV/u beam energy runs. Figure 5.14 shows the distribution of these non-Rutherford events across the detector, below an energy of 2800 keV, in comparison to the distribution of events in the Rutherford scattering peak (2800 $\leq$ E $\leq$ 3200 keV).

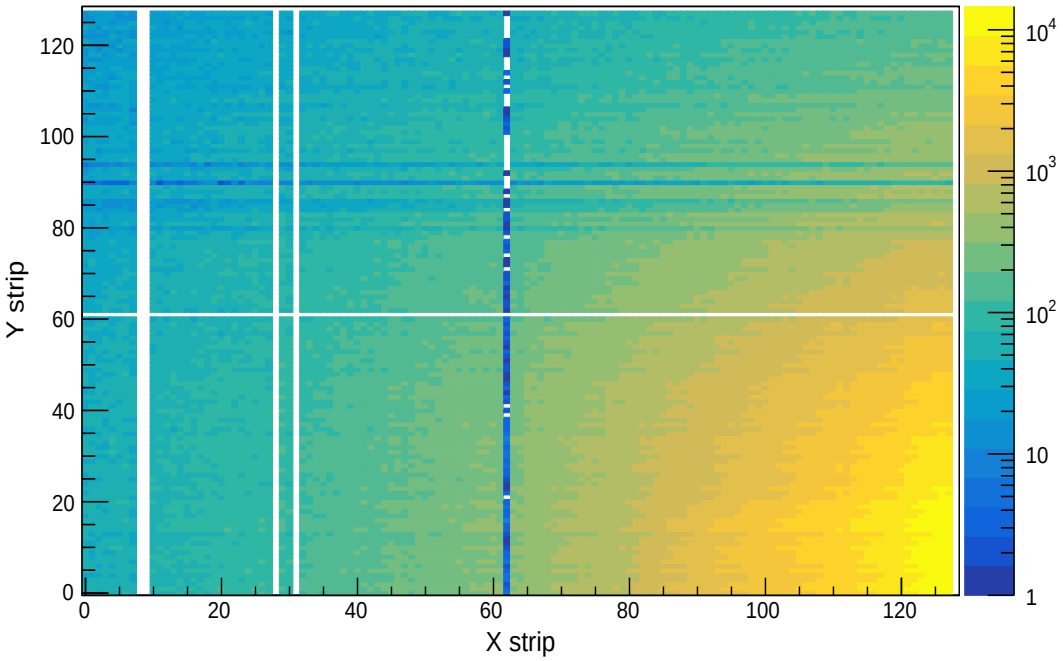

(a)

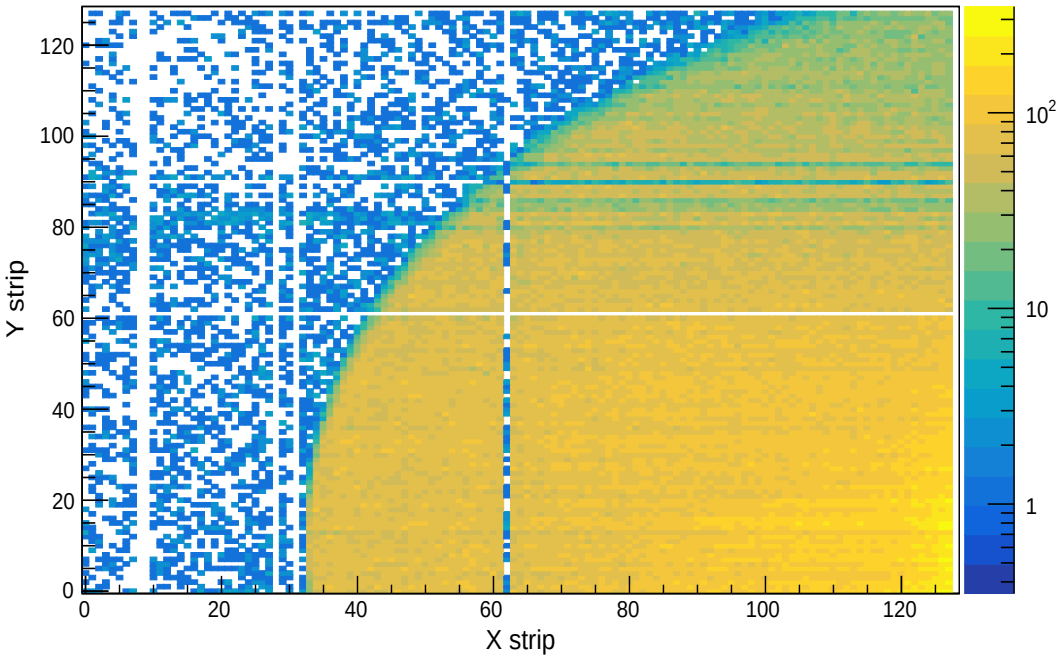

(b)

Figure 5.14: Histogram of the number of events per pixel across the detector for events in the Rutherford peak, in the energy range 2800-3200 keV (a) and events below the Rutherford peak in the energy range 1700-2800 keV (b). The bottom right of the detector (y strip 0 and x strip 128) is closest to the beam.

The distribution of events in the Rutherford scattering peak across the detector, in the top plot of figure 5.14, varies smoothly across the detector. In contrast, the events below 2800 keV do not follow the Rutherford scattering angular distribution but have a circular distribution on the detector with a definitive boundary. At the boundary, the number of observed events drops by an order of magnitude. The position of this boundary from the beam is $\sim$ 100 mm in x and varies between 50-100 mm in y depending on the experimental run. Inside the boundary region, the majority of events below the Rutherford peak are from this unknown source. This can be seen in figure 5.15 which shows energy histograms for a cluster of 400 pixels just inside the circular distribution, x strips 40-60 in figure 5.14, and just outside the circular distribution in x strips 10-30.

The proximity in energy of these events to the Rutherford scattering peak and distribution across the majority of the detector can present a significant challenge to the normalisation of the differential cross section. The number of counts in the low energy tail (<2800 keV) of the Rutherford scattering peak is estimated by considering the percentage of these counts compared to the total number of counts. Outside of the circular distribution, events below 2800 keV typically account for $\sim$2% of all events. Inside, events below 2800 keV can account for up to 20% of all events, depending on the specific experimental run. The difference between the actual number of counts in the low energy tail and this 2% benchmark is subtracted from the total number of counts in the spectrum, to remove the contribution to the total number of counts from this source. A proportion of the counts in the energy spectrum at energies above 2800 keV will originate from the unknown non Rutherford process. The number of these events above 2800 keV is obscured by the Rutherford peak and cannot be determined reliably. The number of these events is not estimated in this work.

These events also present a significant background for the detection of particles with energies below the Rutherford scattering peak. This will affect future experiments aiming to measure reactions with negative Q-values or elastic scattering at backward centre of mass angles performed in inverse kinematics.

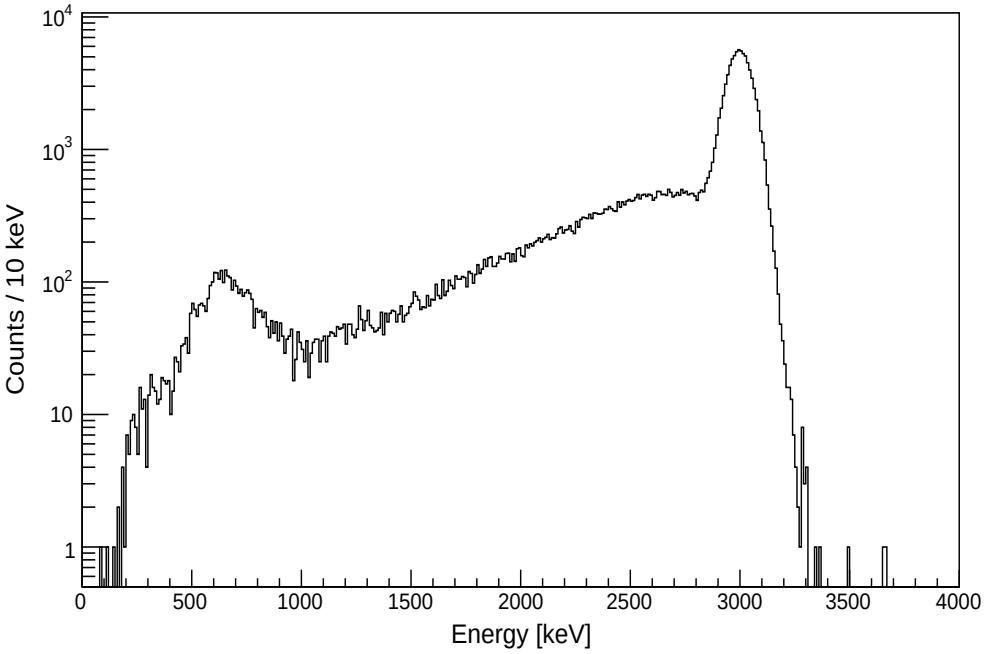

(a)

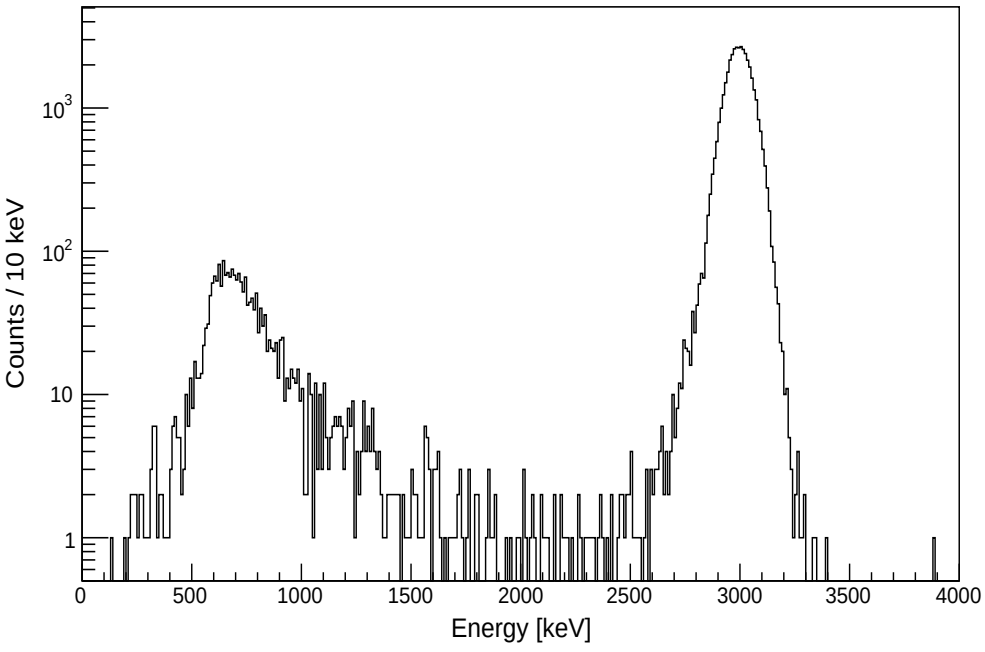

(b)

Figure 5.15: Energy histograms of an area of 400 pixel inside (a) and outside (b) of the circular distribution of events observed in figure 5.14. Events inside the distribution are from x strips 40-60 and y strips 0-20. Events outside the distribution are from x strips 10-30 and y strips 0-20. A large hump below $\sim$2800 keV is observed in the energy spectra of the pixels inside the circular distribution.

The production mechanism of these events is not known, however at energies below the Rutherford peak these events dominate the total event rate. The number of counts per x strip for different energies close to the Rutherford peak is shown in figure 5.16.

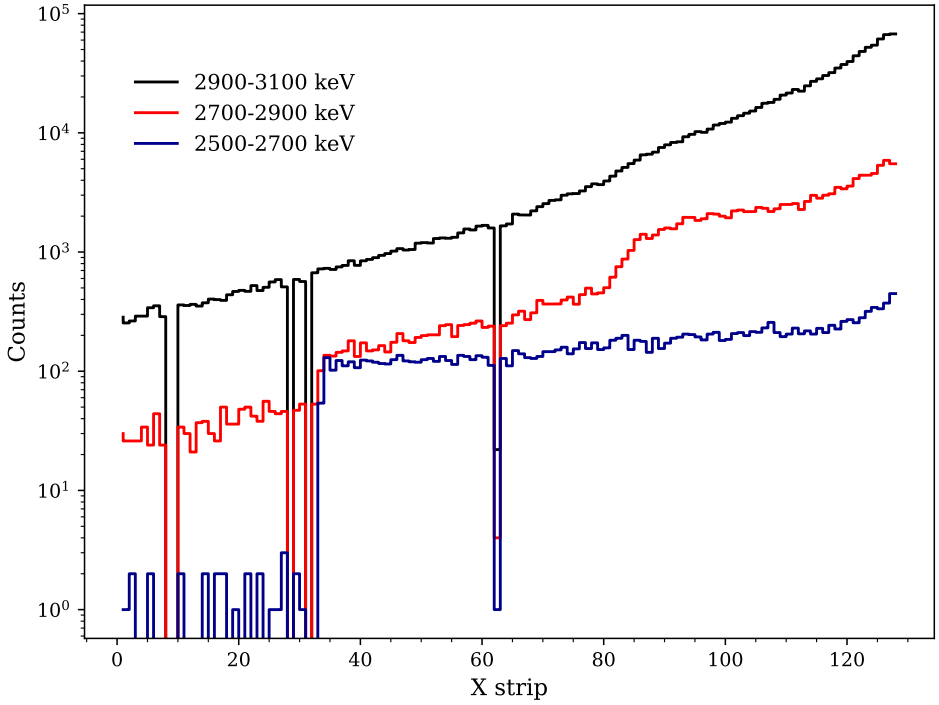

Figure 5.16: Plot of the number of counts in each x strip across five y strips for different energy ranges at a beam energy of 1.5 MeV/u. At $\sim$ 3 MeV, Rutherford scattering is the dominant process and the rate across the detector decreases according to the Rutherford angular distribution. Rutherford scattering continues to dominate at energies of 2700-2900 keV, but two humps in the distribution can be observed at x strips 35 and 85. At lower energies (2600-2800 keV), the number of events across the detector is approximately constant until $\sim$ strip 35 where the number of events drops by two orders of magnitude.

The transition from where the number of counts is Rutherford dominated to where the number of counts is dominated by this unknown source can be seen as the energy range of events is decreased. Rutherford scattering dominates for energies between 2900 and 3100 keV, no other contributions can be observed. In the energy range 2700-2900 keV, two humps in the Rutherford distribution can be observed. In the energy range 2500-2700 keV, no contributions apart from the very edge of the detector can be observed from Rutherford scattering. The hump at $\sim$ strip 85 is also no longer visible. This

hump was also not observed for other experimental runs positioned further from the beam. The rate across the strips is approximately constant until $\sim$ strip 35 where the number of counts decreases by two orders of magnitude. This decrease is what is observed as the circular boundary in figure 5.14.

The mechanism by which events in the low energy tail of the Rutherford scattering peak are produced is not well understood. The hump at $\sim$ strip 85 could be explained by a beam halo striking the detector. The constant number of events that produce the circular distribution with a defined boundary cannot be explained by a beam halo due to the size of the beam pipe. The distance of this boundary from the beam is $\sim$ 100 mm whereas the beam pipe has a diameter of only 50 mm. Other potential mechanisms include blow up of the beam from the multiple scattering interaction with the target [94] or from single scattering of beam particles off residual gas molecules within the whole of the ring section. Blow up of the beam from multiple scattering can be excluded as the target density was not sufficient to produce the required emittance increase. Single scattering events off residual gas molecules may contribute somewhat, but the flat angular distribution and observed sharp drop in the number of counts at the boundary cannot be explained by this mechanism. An isotropic nuclear reaction with a negative Q-value could explain the flat angular distribution, but the sharp drop in the number of counts cannot be explained. Lastly, the DSSD is very sensitive to any light. Light produced anywhere in the ring by vacuum gauges, windows or interactions between the beam and the target [88] could be reflected around the ring to be incident on the detector. Again, the sharp drop in the number events cannot be explained by this mechanism.

This continuum of events below the Rutherford peak is not observed in the 5.5 MeV/u beam energy experimental runs. Figure 5.17 shows an energy histogram for a group of 2000 pixels at a beam energy of 5.5 MeV/u, in which these events below the Rutherford peak are not observed.

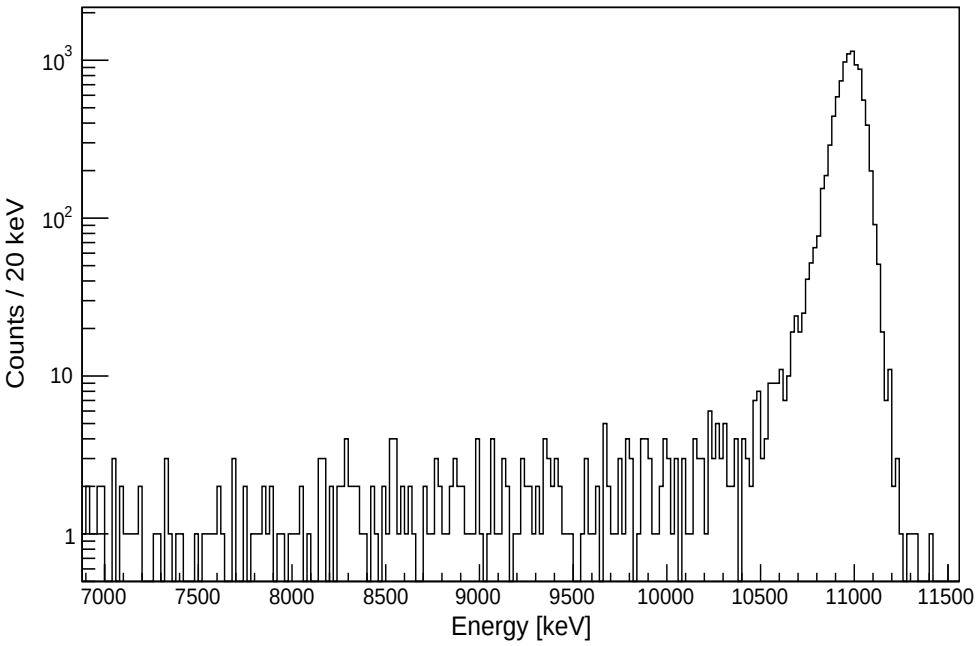

Figure 5.17: Energy histograms of an area of 2000 pixels on the detector for an experimental run at a beam energy of 5.5 MeV/u. Events are from x strips 60-100 and y strips 0-50. Many of the y strips inside this range were inactive, see appendix A for further details. No evidence of events below the Rutherford scattering peak seen in lower beam energy runs are observed.

Chapter 6

Measurement of the ^{14}N(d, p)^{15}N and ^{14}N(d, α)^{12}C reactions

6.1 Introduction

The ^{14}N(d, p)^{15}N and ^{14}N(d, α)^{12}C reactions have been studied using CARME. The excitation energies and cross sections for all states identified have been measured and compared to previous measurements in order to commission the CARME system. The ^{14}N(d, p)^{15}N transfer reaction was of the most interest, as transfer reactions provide a key tool for probing nuclear states of interest and will form part of the future scientific programme for CARME. One such measurement is the inverse kinematic study of the ^{30}P(d, p)^{31}P reaction discussed in chapter 1. The ^{14}N(d, p)^{15}N state with the highest number of counts has been modelled by DWBA calculations, and the spectroscopic factor has been extracted. This spectroscopic factor has been compared to previous experimental studies and theoretical calculations.

6.2 Identification of observed states

Figure 6.1 shows the energy spectrum above the elastic scattering peak, integrated across all detector angles ($\sim$ 2-11 degrees in the laboratory frame), at a beam energy of 1.5 MeV/u. Several states from the positive Q-value ^{14}N(d, p)^{15}N (Q = 8.61 MeV) and ^{14}N(d, α)^{12}C (Q = 13.57 MeV) reactions are identified and labelled with their known excitation energies, which are taken from the NuDAT database [95].

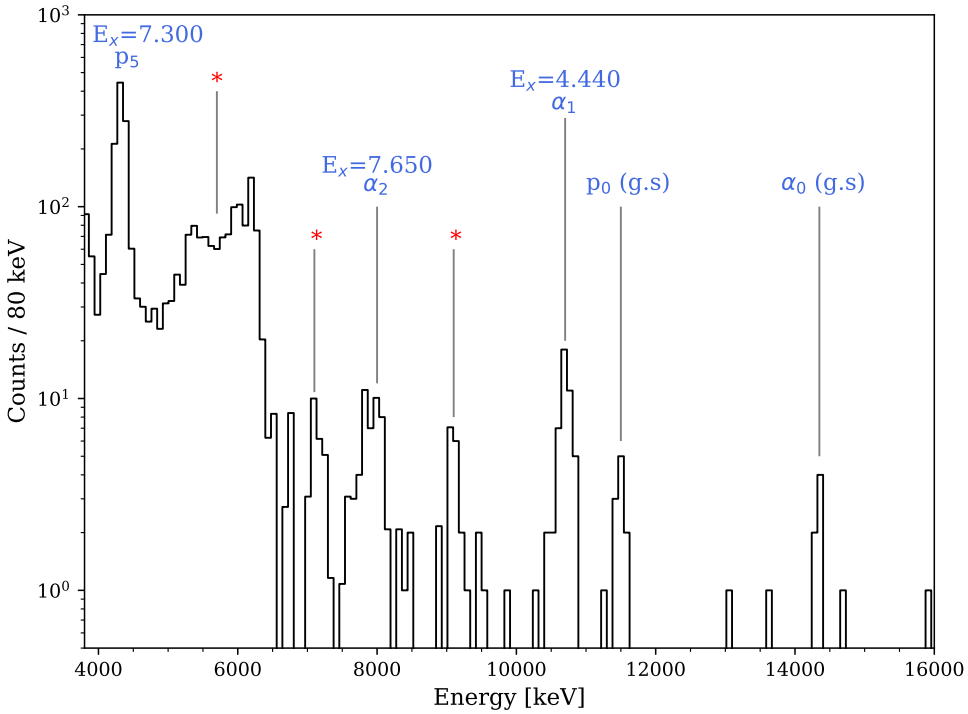

Figure 6.1: Energy spectrum above the elastic scattering peak, integrated across all detector angles (2-11 degrees in the laboratory frame), at a beam energy of 1.5 MeV/u. Several states from the positive Q-value ^{14}N(d, p)^{15}N and ^{14}N(d, α)^{12}C reactions which could be identified are labelled in addition to their known excitation energies, which are taken from the NuDAT database [95]. Structures labelled with a red star are background contributions from low angle scattering events, see text for details.

The excitation energies of different ^{14}N(d, p)^{15}N and ^{14}N(d, α)^{12}C states identified is given in table 6.1. The ^{14}N(d, α_1)^{12}C reaction is not included in the table because it was used in the energy calibration procedure (see chapter 5). The uncertainty in the excitation energy is estimated from the standard error in the mean of each peak ($\sigma/\sqrt{n}$) combined with the uncertainty from the energy calibration. However, this may under represent the uncertainty as the total bin width is 80 keV.

Reaction	J^π	Excitation Energy [a] [keV]	Excitation Energy [b] [keV]
^{14}N(d, p_0)^{15}N	$\frac{1}{2}-$	91 ± 51	0.00
^{14}N(d, p_5)^{15}N	$\frac{3}{2}+$	7312 ± 24	7300.83 ± 0.02
^{14}N(d, α_0)^{12}C	0+	33 ± 61	0.00
^{14}N(d, α_2)^{12}C	0+	7659 ± 40	7654.07 ± 0.19

Table 6.1: Table of states for the ^{14}N(d, p)^{15}N and ^{14}N(d, α)^{12}C reactions, in addition to the spin-parity (J^π) of the final states populated in the reaction. The excitation energy [a] determined in this work is compared to the excitation energy [b] taken from the NuDat database [95]. The uncertainty in the excitation energy is estimated from the standard error in the mean of each peak combined with the uncertainty from the energy calibration.

The energy spectrum shown is integrated across all detector angles, including the lowest angles (< 3 degrees). Events at these low angles contain background events from processes such as elastic scattering, which appear prominently in the spectrum. Prominent features in the spectrum which are observed primarily at these low angles are labelled with a red star. The broad structure labelled between ~ 5 and 6 MeV is thought to primarily be made up of pile up from two elastically scattered deuterons, each with an energy of ~ 3 MeV, although several proton and alpha states which could not be resolved from the background are also present in this region. Two peaks at 7 and 9 MeV are labelled in this manner as they are mostly observed at low angles below 3 degrees, and cannot be explained by any known excited states. The peak at 9 MeV is also thought to be explained by pile up, in this case, of three elastically scattered deuterons. The full integrated spectrum is shown here to clearly highlight each of the identified states, in addition to the scattering background that can be present. The cross section calculations and excitation energy determinations do not include these low angle background contributions. Further discussion of background events is given in appendix B.

6.2.1 Cross section of observed (d, α) states

Cross sections have been determined for the (d, α) states identified in figure 6.1, and compared to previous experimental measurements. The number of observed counts for all states was very low due to the low target density and limited amount of beam-time. Therefore, the cross section was integrated across all detector angles.

The ^{14}N(d, α_0)^{12}C reaction

Figure 6.2 shows the differential cross section determined in this work, in addition to the angular distributions determined by Ishimatsu [96] at beam energies of 2.49, 2.74 and 3.02 MeV, and the angular distributions determined by Gomes [97] for beam energies of 2.4 and 2.7 MeV. Note that the measurements by Gomes are an average of multiple measurements performed at a range of beam energies.

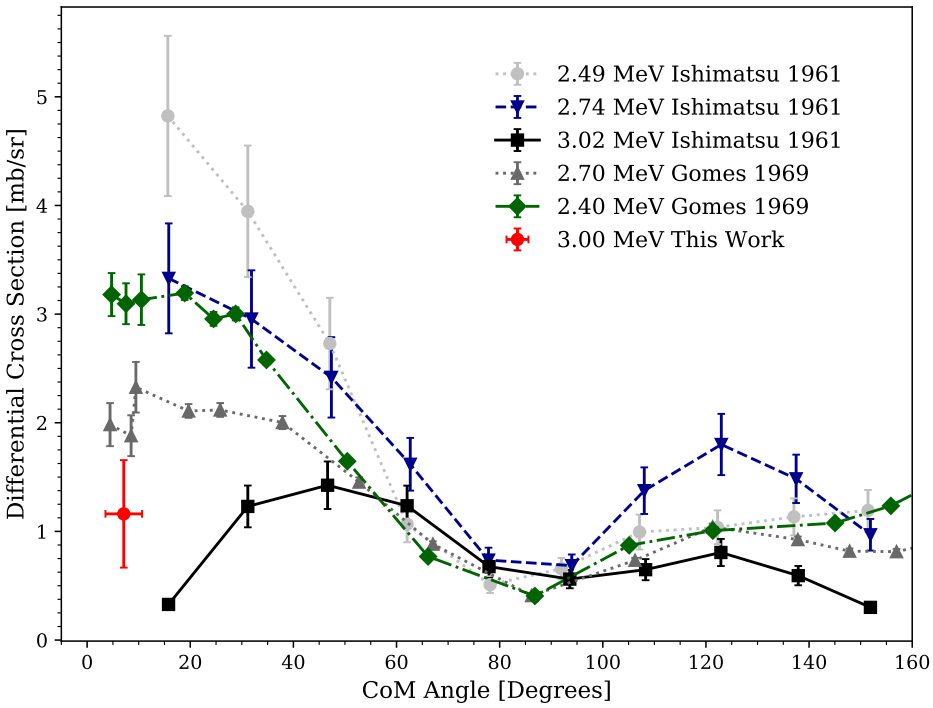

Figure 6.2: Plot of the angular distributions determined by Ishimatsu [96] at beam energies of 2.49, 2.74 and 3.02 MeV and by Gomes [97] at beam energies of 2.4 and 2.7 MeV for the ^{14}N(d, α_1)^{12}C reaction. The differential cross section determined in this work at a beam energy of 3 MeV is shown in red.

The angular distributions determined by Ishimatsu and Gomes are largely symmetrical around 90 degrees, with a forward peak which decreases in magnitude as the beam energy is increased. A similar angular distribution was also observed at slightly lower

beam energies by Mansour [98]. The reaction primarily proceeds by the compound nucleus mechanism. The forward peak in the angular distribution at low energies has be suggested to be the result of resonances in the ^{16}O compound nucleus [96, 98]. Our measurement is in the same angular range as some of the measurements by Gomes, although at a slightly higher beam energy. The differential cross section determined in our work is consistent with those of Ishimatsu and Gomes, considering the slightly different angular and energy ranges of these previous measurements, and the decrease in the cross section as the beam energy is increased.

The ^{14}N(d, α_1)^{12}C reaction

Figure 6.3 shows the differential cross section determined in this work, in addition to the angular distributions determined by Gomes [97] for beam energies ranging from 2 to 2.7 MeV. The angular distributions determined by Gomes are approximately symmetric about 90 degrees, which suggests the reaction proceeds predominately by the compound nucleus mechanism. Our measurement is at a lower angle and a higher beam energy, but appears consistent with the previous measurements by Gomes.

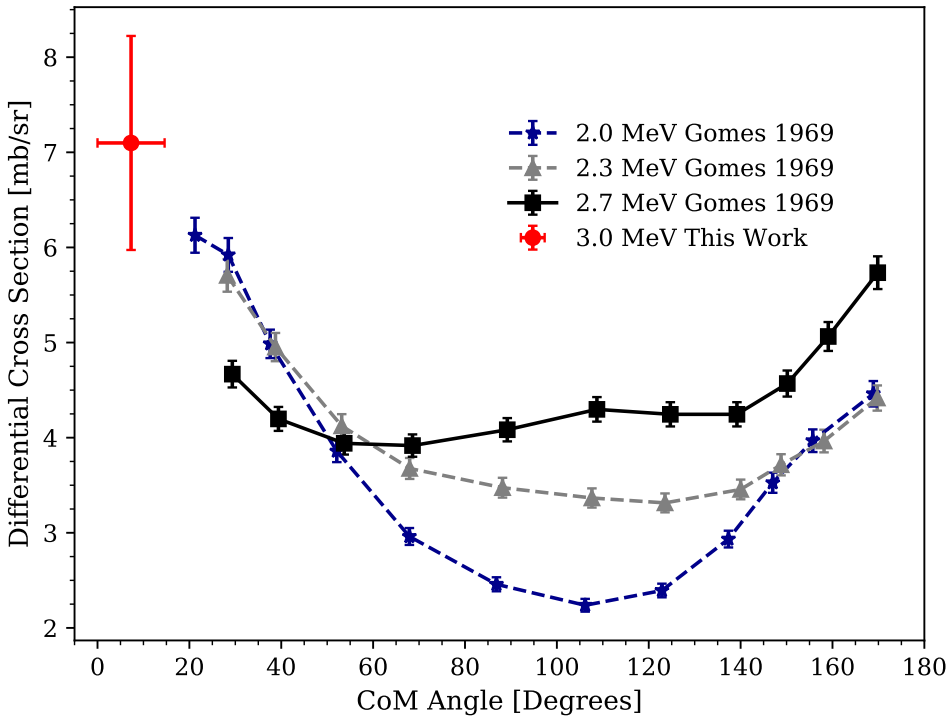

Figure 6.3: Plot of the angular distributions determined by Gomes [97] at beam energies of 2.0, 2.3 and 2.7 MeV for the ^{14}N(d, α_1)^{12}C reaction. The differential cross section determined in this work at a beam energy of 3 MeV is shown in red.

The ^{14}N(d, α_2)^{12}C reaction

Figure 6.4 shows the differential cross section determined in this work, in addition to the angular distributions determined by Gomes [97] at beam energies of 2.4 and 2.7 MeV and by Mansour [98] at beam energies of 2.2 and 2.4 MeV.

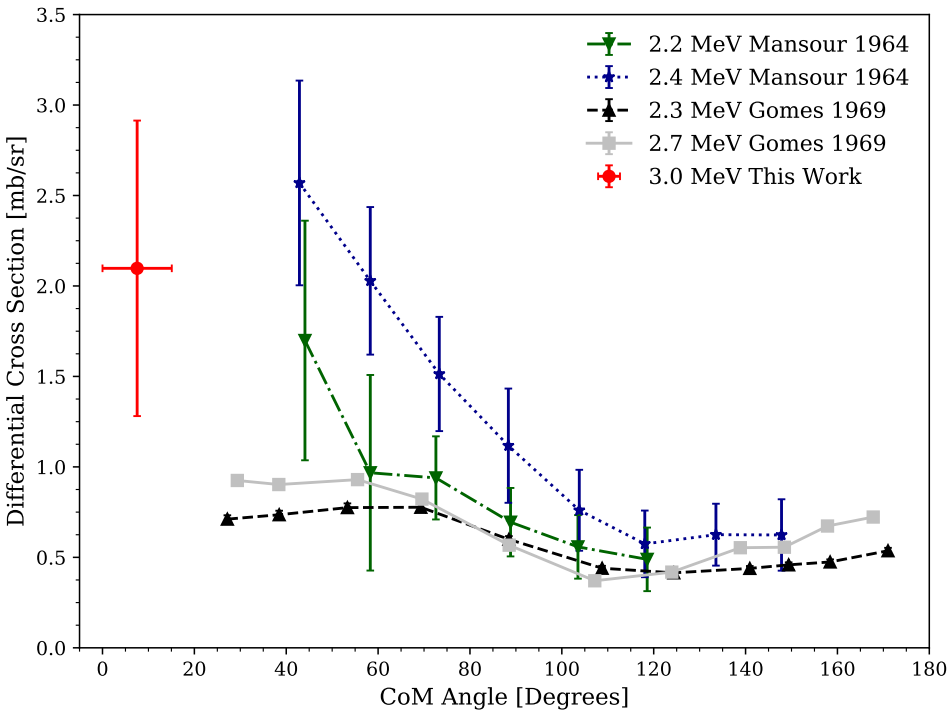

Figure 6.4: Plot of the angular distributions determined by Mansour [98] at a beam energy of 2.2 and 2.4 MeV and by Gomes [97] at beam energies of 2.4 and 2.7 MeV for the ^{14}N(d, α_2)^{12}C reaction. The differential cross section determined in this work at a beam energy of 3 MeV is shown in red.

The measurements by Gomes suggest an approximately isotropic distribution. The measurements by Mansour carry very large uncertainties but show a forward peak in the angular distribution at beam energies greater than 2.2 MeV, which may be the result of some direct component to the reaction mechanism. Below this beam energy, the measurements by Mansour show an isotropic distribution. The differential cross section determined in our measurements also carries a large uncertainty and is at a lower angle than previous measurements, but appears consistent with the higher cross section reported by Mansour.

6.3 The ^{14}N(d, p)^{15}N transfer reaction

This section presents the cross section determined in this work for the ^{14}N(d, p)^{15}N reaction to the ground state and to the fifth excited state. The cross sections have been compared to previous measurements, and the spectroscopic factor has been extracted for the $\ell = 0$ transfer reaction to the fifth excited state.

6.3.1 The ^{14}N(d, p$_0$)^{15}N reaction

Similar to the (d, α) reactions, very few counts were observed for the reaction to the ground state, and therefore the cross section was integrated across all detector angles. Figure 6.5 shows the differential cross section determined in this work, in addition to the angular distributions determined by Gallmann [99] at a beam energy of 3.5 MeV and by Beaumeveille [100] at a beam energy of 3 MeV.

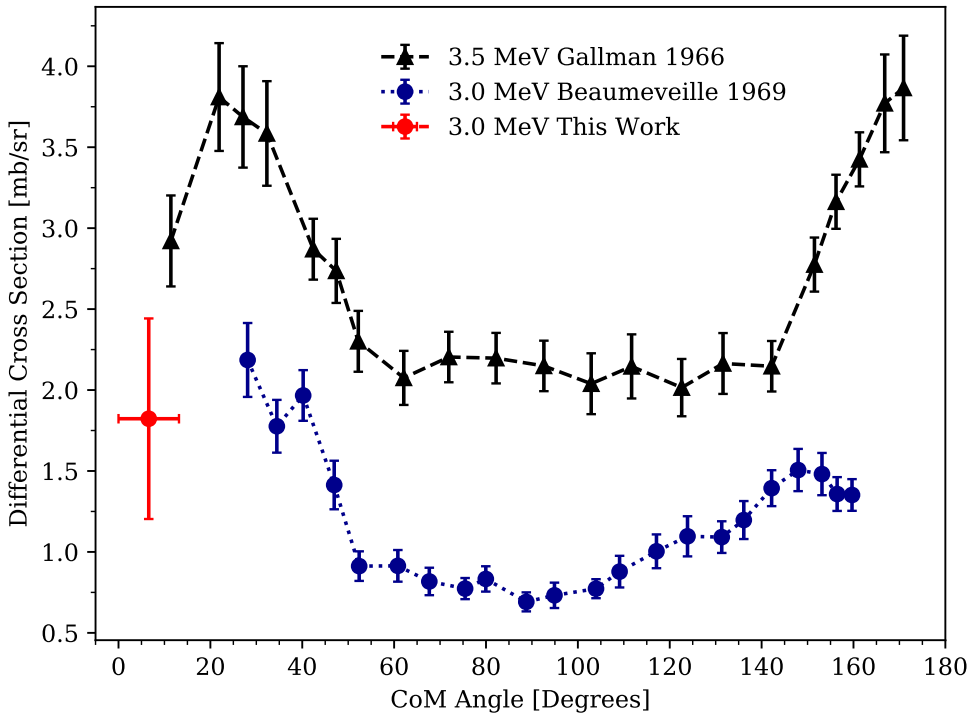

Figure 6.5: Plot of the angular distributions determined by Gallmann [99] at a beam energy of 3.5 MeV and by Beaumeveille [100] at a beam energy of 3 MeV for the ^{14}N(d, p$_0$)^{15}N reaction. The differential cross section determined in this work at a beam energy of 3 MeV is shown in red.

The angular distributions determined in the previous measurements are approximately symmetric with peaks at forward and backward angles. The angular distribution was

best fit by Gallmann when considering both the direct and compound reaction mechanisms. A study at lower beam energies by Valek [101] also found significant contributions from both the direct and compound reaction mechanisms. The cross section determined by Gallmann is larger than that of Beaumeveille, which is true across the range beam energies measured by both studies which are not shown in the plot. Our measurement is at a lower angle than those of both Gallmann and Beaumeveille, but is consistent with both the previous measurements.

6.3.2 The ^{14}N(d, p$_5$)^{15}N reaction

The ^{14}N(d, p$_5$)^{15}N reaction was shown in previous experimental studies to have the highest cross section of all the (d, p) states at similar energies to those measured using CARME. This was seen in our measurement, as the number of counts from the ^{14}N(d, p$_5$)^{15}N reaction was at least an order of magnitude greater than any other state observed. Previous measurements by Gomes [97] and Beaumeveille [100] were in the same approximate angular and energy range as our measurements, which in addition to the high number of counts, made this reaction ideal for the commissioning of CARME.

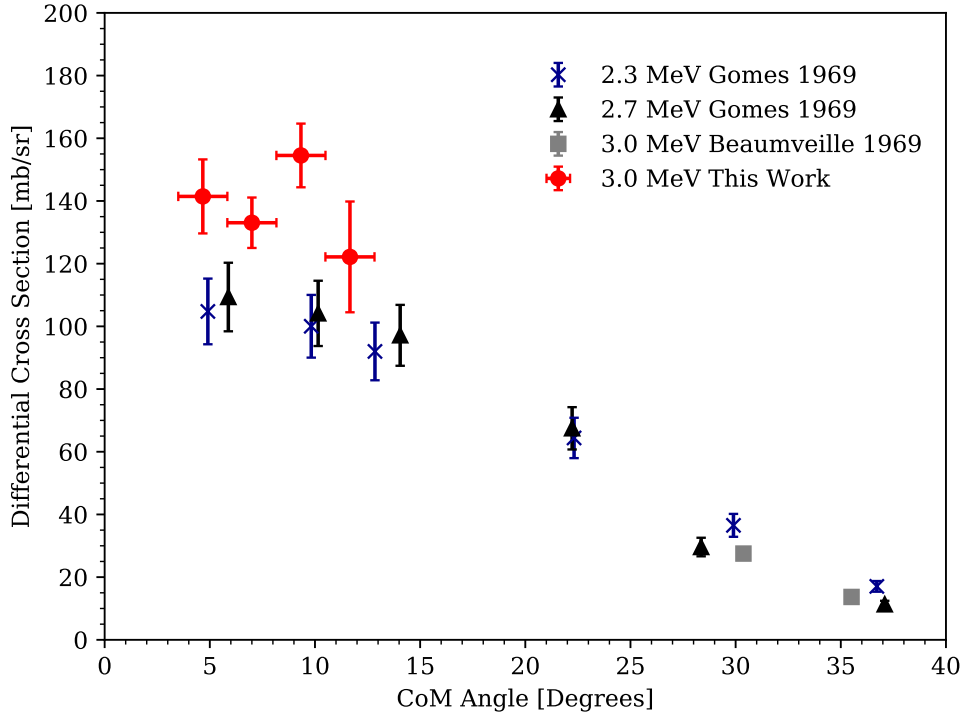

Figure 6.6: Plot of the angular distributions determined by Gomes [97] at beam energies of 2.3 and 2.7 MeV and by Beaumeveille [100] at a beam energy of 3 MeV for the ^{14}N(d, p$_5$)^{15}N reaction. The differential cross section determined in this work at a beam energy of 3 MeV is shown in red.

Figure 6.6 shows the differential cross section determined in this work at various angles below 11 degrees, in addition to the angular distributions determined by Gomes [97] at beam energies of 2.3 and 2.7 MeV and by Beaumeveille [100] at a beam energy of 3 MeV. The angular distribution has a very large forward peak, which was shown to increase in magnitude at higher beam energies across the energy range studied by Gomes (1-3.1 MeV). Gomes modelled the angular distribution of the reaction using DWBA and Hauser-Feshbach calculations, and determined the direct $\ell = 0$ transfer dominated the reaction mechanism. The compound mechanism was estimated to contribute less than 1 % to the cross section in the forward peak [97]. The uncertainty in our measurements is dominated by the statistical uncertainty for each data point, and ranges from 6 - 15 % depending on the number of counts observed. Our measurements appear consistent with those of Gomes, considering the uncertainty in both measurements and the higher beam energy used in our measurement.

6.3.3 Extraction of the spectroscopic factor

The spectroscopic factor has previously been reported in experimental studies for a range of different beam energies [97, 100–102] and by theoretical calculations by MacFarlane [103]. The spectroscopic factors reported by these studies is given in table 6.2.

Reference	Spectroscopic factor
Gomes [a] [97]	0.72
Gomes [b] [97]	0.70
Beaumeveille [100]	0.89
Valek [101]	0.72
Philips [101]	0.89
MacFarlane [103]	0.64

Table 6.2: Table of spectroscopic factors determined in previous studies. Spectroscopic factors reported by Gomes [97], Beaumeveille [100], Valek [101] and Phillips [102] are from experimental studies. The spectroscopic factor reported by MacFarlane [103] is from a theoretical calculation. Superscripts a and b denote the two different potentials (D3+P2) and (D4+P1) used in the DWBA calculations by Gomes.

To extract the spectroscopic factor from our experimental measurements, finite-range DWBA calculations were performed using the nuclear reaction code Fresco [104] for the direct $\ell = 0$ transfer. Hauser-Feshbach calculations were not performed as the compound contribution to the cross section is negligible. Fresco requires inputs for the relevant nuclear physics of the reaction, such as the spin parity of the initial and final states and the angular momentum transfer required to populate that state, in addition to the potentials involved in the reaction. Five potentials are required for the Fresco calculation; the entrance channel potential (^{14}N + d), the exit channel potential (^{15}N + p), the potential of the transferred neutron into the final state (^{14}N + n), the core-core potential (^{15}N + p), and the potential inside the deuteron (p + n). The first four of these potentials are often described by a Coulomb potential, a volume potential consisting of both real and imaginary components, a surface potential consisting of an imaginary component, and a spin orbit potential with a real component. The non-Coulomb potentials are described by the Woods-Saxon potential shape. The potential of the deuteron is described by the Reid soft-core potential [105]. The optical model parameters (OMP) which describe each of these potentials are determined from experimental scattering data. The OMP parameters used in this Fresco calculation, and which are described in table 6.3, were obtained from the OMP reference input parameter library [106], where parameters were calculated using data from references [107–110]. The parameters used are similar to those employed by Gomes [97], Beaumeveille [100] and Valek [101].

V_v	r_v	a_v	W_v	r_{wv}	a_{wv}	W_D	r_D	a_D	V_{so}	r_{so}	a_{so}	r_c
94.0	1.15	0.65	1.30	1.35	0.61	10.7	1.40	0.68	3.60	0.97	1.01	1.30
61.0	1.06	0.65	1.60	1.37	0.77	5.00	1.37	0.77	6.00	1.06	0.78	1.25
47.4	1.25	0.68	0.00	1.39	0.45	4.40	1.26	0.51	7.00	1.31	0.66	1.30
51.9	1.16	0.75	1.30	1.37	0.77	5.00	1.37	0.77	6.00	1.06	0.78	1.25

Table 6.3: Optical model potential (OMP) parameters used in Fresco DWBA calculations for the entrance channel (^{14}N + d), exit channel (^{15}N + p), transferred neutron (^{14}N + n), and the core-core (^{15}N + p) potentials. V [MeV], r [fm] and a [fm] describe the depth, radius and diffuseness of the Woods-Saxon potential. The sub-scripts v, D and so correspond to the real and imaginary volume potential, the imaginary surface potential and the real spin-orbit potential respectively. The radius of the Coulomb potential is described by r_c. OMP parameters for each potential have been obtained from the OMP reference input parameter library [106].

Figure 6.7 shows the cross section of our measurements at a beam energy of 3 MeV using CARME, the angular distribution of the $\ell = 0$ transfer calculated using Fresco and fit to our experimental measurements, in addition to the measurements by Gomes at a beam energy of 2.7 MeV and by Beaumeveille at a beam energy of 3 MeV.

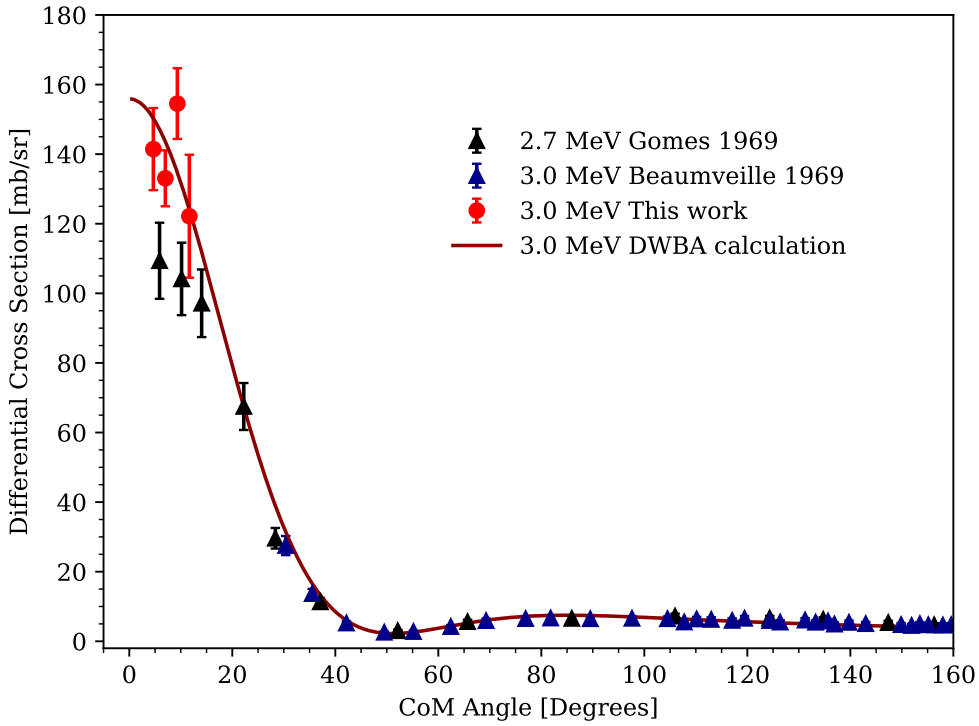

Figure 6.7: Plot of the angular distribution for the ^{14}N(d, p$_5$)^{15}N reaction. The differential cross section at several angles determined in this work at a beam energy of 3 MeV is shown in red. Measurements by Gomes [97] at average beam energies of 2.3 and 2.7 MeV and by Beaumeveille at a beam energy of 3 MeV are also shown.

The spectroscopic factor extracted from the comparison between our experimental measurements and the Fresco DWBA calculation, using equation 1.6, is $C^2S = 0.66$. The uncertainty resulting from the χ^2 fitting ($\chi^2 + 1$) to the experimental data is ~ 5 %. This spectroscopic factor is in good agreement with the spectroscopic factors reported by Gomes (0.72, 0.70), Valek (0.72) and Macfarlane (0.64), and is slightly lower than those by Beaumeveille (0.89) and Phillips (0.89).

In the Fresco calculation conducted in this work, the parameters of each potential were varied to estimate the impact on the calculated cross section. The entrance and exit channels were found to be important in producing the correct shape for the angular distribution, but had only a small effect on the magnitude of the cross section. The neutron potential was found to have no impact on the shape of the angular distribution,

but did significantly influence the magnitude of cross section. This dependence of the cross section on the neutron potential was also reported by Gomes [97]. In particular, the the cross section was found to have a large dependence on the volume radius r_v and diffuseness a_v parameters in the neutron potential. A representation of the impact of changing the radius parameter has on the cross section is shown in figure 6.8. In the plot, the volume radius r_v was varied by 5 %, while all other potential parameters were fixed. A 5 % difference in the volume radius parameter was chosen as this is the level of difference between the two neutron potentials considered by Valek [101], and the difference between different parameter sets in the OMP database.

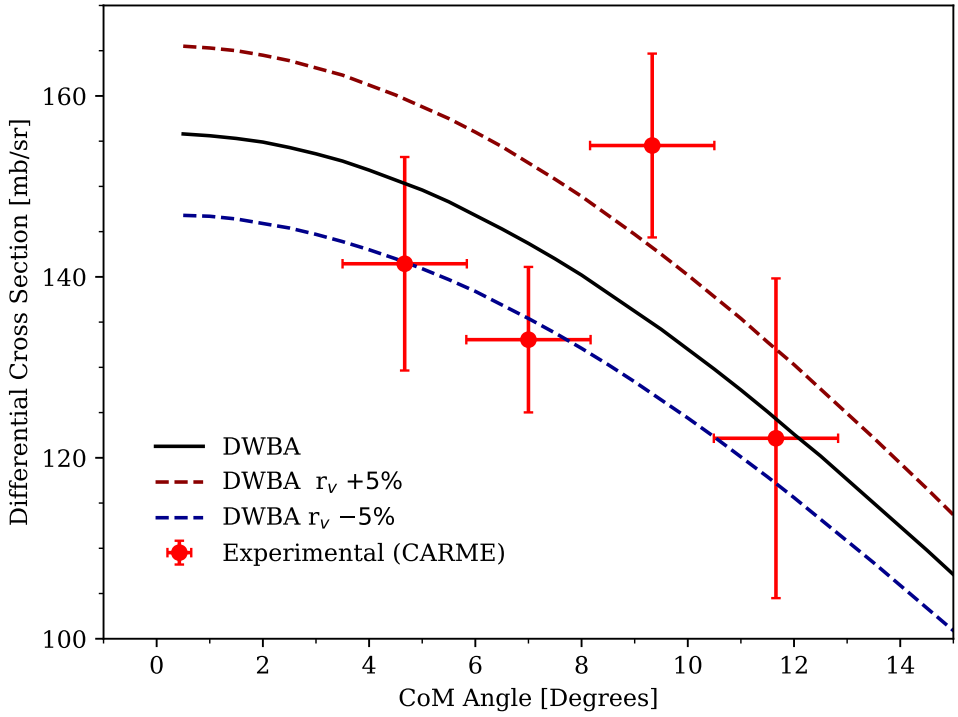

Figure 6.8: Plot of the angular distribution calculated using Fresco for the ^{14}N(d, p$_5$)^{15}N reaction. Experimental measurements determined in this work are shown in red. The angular distribution for potential parameters described in table 6.3 is shown in black. The dashed lines show where the volume radius parameter r_v in the ^{14}N + n potential has been increased (red) and decreased (blue) by 5%.

The 5 % change in the volume radius parameter in the neutron potential results in a change in the cross section of approximately 6%. The cross section has a similar dependence on the volume diffuseness parameter, but the variation of this parameter in previous calculations or from different parameter sets in the OMP database is significantly smaller than for the volume radius parameter.

Chapter 7

Conclusions and Summary

For many stellar scenarios, high precision nuclear reaction measurements are required to further improve our understanding. Many of these measurements are extremely challenging to perform using conventional methodologies. CARME is a new charged particle detection array designed to perform these measurements in storage rings, at the low energies (∼MeV) relevant for stellar scenarios. CARME utilises highly segmented double sided silicon strip detectors (DSSDs) which are positioned at low angles. This enables CARME to perform high precision, high resolution measurements of many nuclear reactions not possible with other methodologies.

This thesis described the commissioning and development of CARME from a bare vacuum chamber to a fully commissioned reaction measurement array. CARME was commissioned using a deuteron beam incident on a ^{14}N target. The ^{14}N(d, p)^{15}N and the ^{14}N(d, α)^{12}C reactions were measured, the first nuclear reactions measured on the CRYRING, with differential cross sections for various states determined and compared to literature. The spectroscopic factor was determined for the ^{14}N(d, p$_5$)^{15}N reaction, which is consistent with values determined by Gomes [97], Valek [101] and theoretical predictions by MacFarlane [103], validating the CARME system. Experimental and analysis procedures for storage ring measurements using CARME have been developed. These include experimental procedures for the production of XHV vacuum conditions with DSSDs and internal cabling installed, and the safe operation of moving detectors synchronous with the storage ring cycle.

Further work is ongoing to improve the experimental setup and implement the lessons learned from the commissioning beam time. This includes the installation of additional detectors and the reduction of the noise within the system. Following this work, CARME will be well placed to perform an array of different reaction measurements with implications for a wide range of stellar scenarios. In 2024, the resonant elastic scattering of ^{15}O on a helium gas target will be conducted to probe the ^{19}Ne compound nucleus relevant for the production of ^{18}F in novae. CARME is also part of an exciting collaboration with the FISIC experiment at the CRYRING. This collaboration would see CARME and FISIC perform the first direct measurement of a bare ion reaction, which has direct implications for all low energy reaction measurements.

Appendix A

High energy experimental runs

Measurements were performed at beam energies of 1.5 MeV/u and 5.5 MeV/u. Data gathered during experimental runs at the higher beam energy are not presented in the main body of this thesis due to the technical challenges experienced during and the limited conclusions that could be extracted from these runs.

A.1 Technical challenges

In the experimental runs performed at 5.5 MeV/u, the detector suffered from two major technical challenges which limited the data that could be gathered. The first of these was the challenge of separating the different phases of the ring cycle. The high energy runs were the first to be performed using CARME, and therefore the detectors were kept stationary, which resulted in no movement signals to allow for the separation of the different ring phases. Unlike with the stationary runs performed at the lower beam energy, the Rutherford scattering rate was not sufficient to separate the different phases due to the low target density. This resulted in the majority of the data gathered during these runs being unable to be further analysed due to the overwhelming noise from all the different phases of the ring cycle.

The second issue was that many of the y strips on the detector were non-functional throughout the high energy experimental runs. No data was recorded from these strips and no data was observed in the live histograms in the MIDAS data acquisition system. The five x strips closest to the beam also suffered some electronics issue, as the count rate in these strips is not consistent with the Rutherford scattering observed in the

remaining strips. The final experimental run at the higher beam energy was abruptly halted by a crash of the data acquisition system. The system was reset for the subsequent runs at a lower beam energy of 1.5 MeV/u, in which the previously inactive y strips were active. Figure A.1 shows a plot of the total number of counts for each pixel during at 5.5 MeV/u, in which the many inactive strips can be seen.

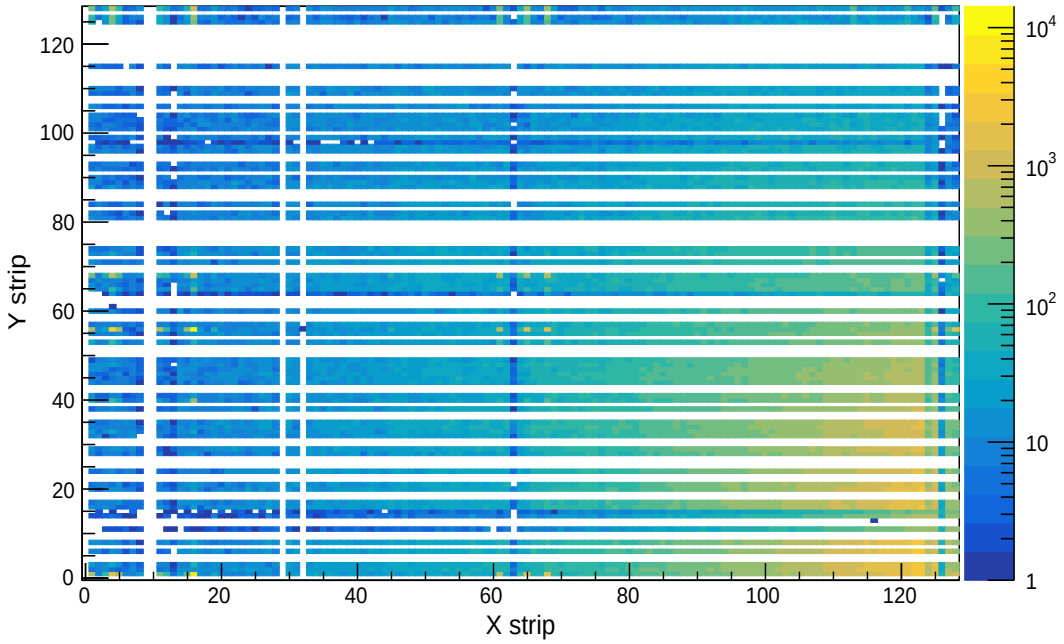

Figure A.1: Histogram of the total recorded counts per pixel at the start of the beam time where many y strips were non-functional. Data for these strips was missing from live histograms in the MIDAS data acquisition system. The bottom right of the detector (y strip 0 and x strip 128) is closest to the beam. The majority of the observed counts are from Rutherford scattering, which decreases with distance from the beam.

The cause of the inactive strips, and the subsequent re-activation of these strips is not fully understood, but may have been caused by an issue with the internal cabling. This is as unexplained behaviour was also observed during pulser walk-throughs performed after the experimental period. Multiple pulser walk-throughs were performed before and after a movement cycle of the detector. The ADC offset and gain parameters are characteristics of the electronics and should not change over time. However, the ADC offsets for some of the channels, corresponding to the y strips, were observed to be affected by the movement cycle. The change in the ADC offset was $<$50 keV, and any change in the ADC offsets is not expected to affect the energy of detected events due to the energy matching of the x and y energies. A number of channels were also

observed to become non-functional following the movement cycle. The reason for this is not understood, but significant bending of the internal cabling is one possible cause. Strain reliefs were installed, but upon inspection of the internal components following the commissioning beam-time, many of the strain reliefs were found to have become dislodged and no longer provided any strain relief. The remaining strain reliefs are also thought to have provided a negligible effect on constraining the movement of the cabling.

A.2 5.5 MeV/u Energy spectrum

An energy spectrum for the high beam energy runs, above the elastic scattering peak is shown in figure A.2. Peaks which correspond to the first three excited states from the ^{14}N(d, α)^{12}C reaction and the fifth excited state from the ^{14}N(d, p)^{15}N reaction have been labelled with their known excitation energies which are taken from the NuDAT database [95]. Cross sections for these states are not presented due to the technical issues experienced during these runs.

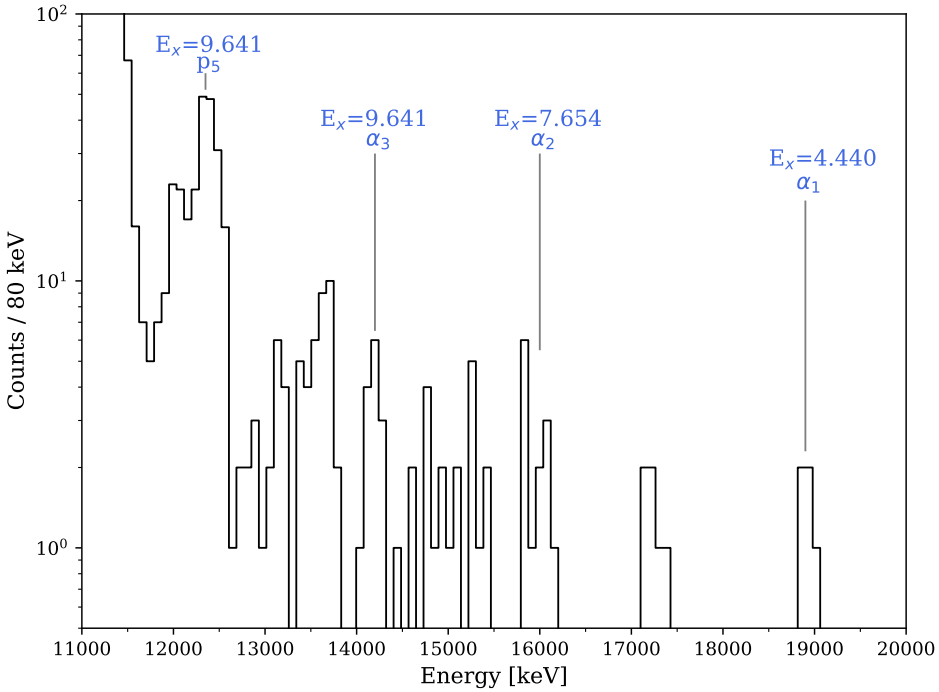

Figure A.2: Energy spectrum above the elastic scattering peak, integrated across all detector angles (2-11 degrees in the laboratory frame), at a beam energy of 5.5 MeV/u. Peaks which correspond to the first three excited states from the ^{14}N(d, α)^{12}C reaction and the fifth excited state from the ^{14}N(d, p)^{15}N reaction have been labelled with their known excitation energies which are taken from the NuDAT database [95].

Appendix B

Background events

Several background runs were conducted prior to the beam time in order to characterise the background level. Figure B.1 shows the background rate determined from a combined run time of $\sim$ 94 hours, in the energy range from 2 to 20 MeV.

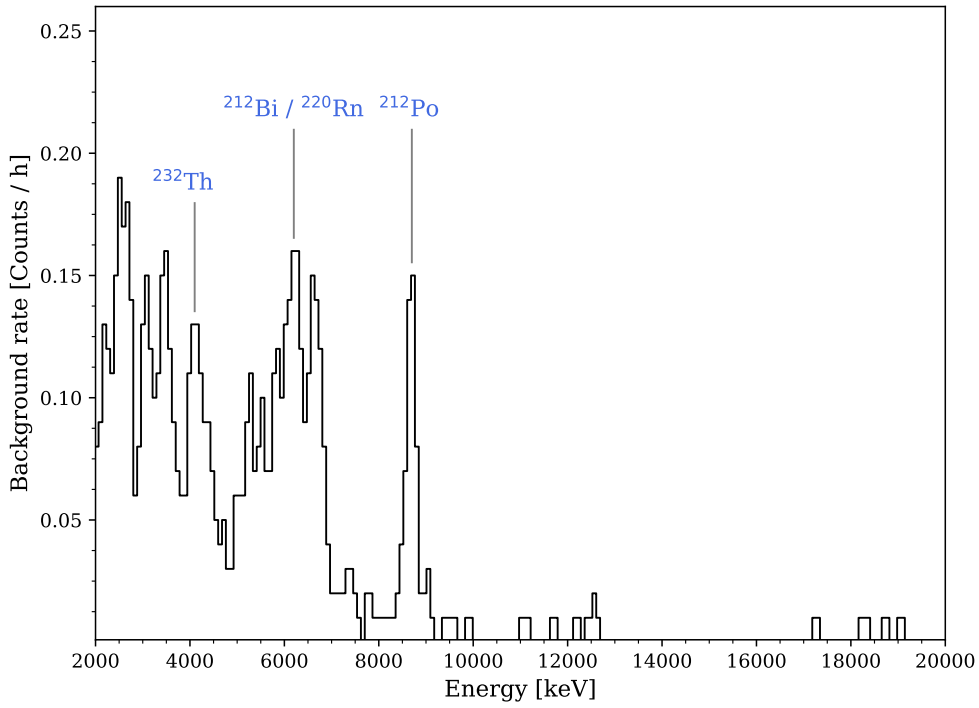

Figure B.1: Energy spectrum of the background rate obtained from a combined background run time of ~94 hours, in the energy range from 2 to 20 MeV. The main contribution to the background rate is from the alpha decay of radioactive elements in the thorium and uranium decay series. Several prominent peaks corresponding to radioactive elements in the thorium series are labelled.

These runs were conducted while no beam was circulating in the ring and when the ring dipole magnets were inactive, and therefore may underestimate the background experienced during the beam time. Several peaks were observed in the background spectrum below 9 MeV, but above 10 MeV very few counts were observed. The main contribution to the rate in the background runs is from the decay of radioactive elements within materials close to the silicon detectors or from within the detectors themselves. Th peak at 8.8 MeV from the decay of ^{212}Po is a clear sign of thorium decay series elements [111]. Other elements from the thorium decay series such as ^{232}Th, ^{212}Bi and ^{220}Rn were also identified in the background spectrum. Peaks in the energy range of the uranium decay series elements were also present in the background.

In addition to the background level characterised in figure B.1, an additional level of background was observed during the beam time at very low angles on the edge of the detector. This background was either not observed, or observed at a much reduced rate at higher angles. Figure B.2 shows a comparison between energy spectra for events between 1 and 3 degrees in the laboratory frame (top plot), and events between 5 and 7 degrees (bottom plot) for the same experimental run. Approximately 1400 pixels are contained within the 1-3 degree angular range compared to 6800 pixels in the 5-7 degree angular range. The number of pixels in each of these angular ranges can be visualised in figure 5.6. Despite the larger number of pixels, the number of counts for structures which have been labelled with a red star in the top plot, are significantly reduced or not present at all in the higher angular range. These structures are thought to be from elastic scattering, which is much reduced at higher angles. The broad structure between 5 and 6 MeV and the peak at 9 MeV, is thought to be from the pile up of two and three scattered deuterons respectively. The origin of the 7 MeV peak is unknown, but it is likely from some scattering process due to only being observed at low angles. In addition to the features highlighted with a red star, at low angles some additional counts are also observed at energies corresponding to states of interest. In particular, additional counts were observed in the same energy range as the p_5 and α_2 states. The cross section for the p_5 state in the 1-3 degree angular range is approximately twice as large as expected. Due to the increased background at very low angles, these counts were not included in the cross section and excitation energy calculations.

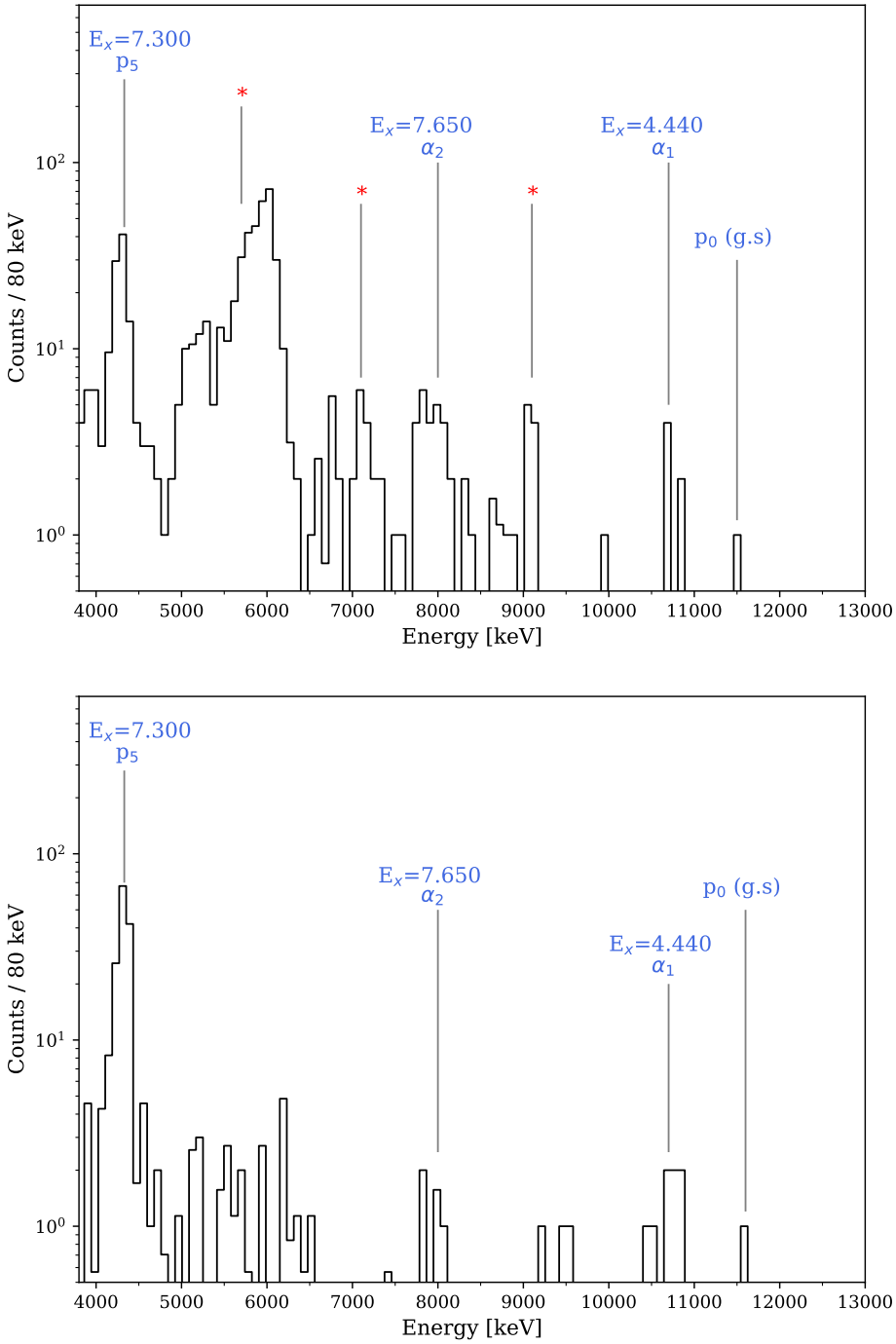

Figure B.2: Energy spectra in the 1-3 degree (top) and 5-7 degree (bottom) angular ranges, above the elastic scattering peak, at a beam energy of 1.5 MeV/u. Several states from the ^{14}N(d, p)^{15}N and ^{14}N(d, α)^{12}C reactions are labelled in addition to their known excitation energies, which are taken from the NuDAT database [95]. Peaks labelled with a red star are background contributions from low angle scattering events. The number of events from these low angle scattering events are greatly reduced at higher angles.

Bibliography

[1] C.G. Bruno et al. "CARME — The CRYRING Array for Reaction MEasurements: A new approach to study nuclear reactions using storage rings". In: *Nuclear Instruments and Methods in Physics Research Section A: Accelerators, Spectrometers, Detectors and Associated Equipment* 1048 (2023), p. 168007. ISSN: 0168-9002. DOI: https://doi.org/10.1016/j.nima.2022.168007. URL: https://www.sciencedirect.com/science/article/pii/S0168900222012992.

[2] Masa-aki Hashimoto. *Big Bang Nucleosynthesis, Thermonuclear History in the Early Universe*. 2nd ed. Springer, 2018.

[3] Christian Iliadis. *Nuclear physics of stars*. 2nd Edition. Wiley, 2015.

[4] Jennifer A. Johnson. "Populating the periodic table: Nucleosynthesis of the elements". In: *Science* 363.6426 (2019), pp. 474–478. DOI: 10.1126/science.aau9540. eprint: https://www.science.org/doi/pdf/10.1126/science.aau9540. URL: https://www.science.org/doi/abs/10.1126/science.aau9540.

[5] Stan Woosley and Thomas Janka. "The physics of core-collapse supernovae". In: *Nature Physics* 1.3 (Dec. 2005), pp. 147–154. ISSN: 1745-2481. DOI: 10.1038/nphys172. URL: https://doi.org/10.1038/nphys172.

[6] A. Burrows and D. Vartanyan. "Core-collapse supernova explosion theory". In: *Nature* 589.7840 (Jan. 2021), pp. 29–39. ISSN: 1476-4687. DOI: 10.1038/s41586-020-03059-w. URL: https://doi.org/10.1038/s41586-020-03059-w.

[7] R. M. Bionta et al. "Observation of a neutrino burst in coincidence with supernova 1987A in the Large Magellanic Cloud". In: *Phys. Rev. Lett.* 58 (14 Apr. 1987), pp. 1494–1496. DOI: 10.1103/PhysRevLett.58.1494. URL: https://link.aps.org/doi/10.1103/PhysRevLett.58.1494.

[8] K. Hirata et al. “Observation of a neutrino burst from the supernova SN1987A”. In: *Phys. Rev. Lett.* 58 (14 Apr. 1987), pp. 1490–1493. DOI: 10.1103/PhysRevLett.58.1490. URL: https://link.aps.org/doi/10.1103/PhysRevLett.58.1490.

[9] Matthieu Renaud et al. “The signature of 44Ti in Cassiopeia a Revealed by IBIS/ISGRI on INTEGRAL”. In: *The Astrophysical Journal* 647 (Dec. 2008). DOI: 10.1086/507300.

[10] Brian Grefenstette et al. “The distribution of radioactive ^{44}Ti in Cassiopeia A”. In: *The Astrophysical Journal* 834 (Dec. 2016). DOI: 10.3847/1538-4357/834/1/19.

[11] Siegert, Thomas et al. “Revisiting INTEGRAL/SPI observations of 44Ti from Cassiopeia A”. In: *A&A* 579 (2015), A124. DOI: 10.1051/0004-6361/201525877. URL: https://doi.org/10.1051/0004-6361/201525877.

[12] S. A. Grebenev et al. “Hard-X-ray emission lines from the decay of 44Ti in the remnant of supernova 1987A”. In: *Nature* 490.7420 (Oct. 2012), pp. 373–375. ISSN: 1476-4687. DOI: 10.1038/nature11473. URL: https://doi.org/10.1038/nature11473.

[13] S. E. Boggs et al. “44Ti gamma-ray emission lines from SN1987A reveal an asymmetric explosion”. In: *Science* 348.6235 (2015), pp. 670–671. DOI: 10.1126/science.aaa2259. eprint: https://www.science.org/doi/pdf/10.1126/science.aaa2259. URL: https://www.science.org/doi/abs/10.1126/science.aaa2259.

[14] Clarisse Tur, Alexander Heger, and Sam M. Austin. “PRODUCTION OF 26Al, 44Ti, AND 60Fe IN CORE-COLLAPSE SUPERNOVAE: SENSITIVITY TO THE RATES OF THE TRIPLE ALPHA AND 12C(α, γ)16O REACTIONS”. In: *The Astrophysical Journal* 718.1 (June 2010), p. 357. DOI: 10.1088/0004-637X/718/1/357. URL: https://dx.doi.org/10.1088/0004-637X/718/1/357.

[15] Georgios Magkotsios et al. “TRENDS IN 44Ti AND 56Ni FROM CORE-COLLAPSE SUPERNOVAE”. In: *The Astrophysical Journal Supplement Series* 191.1 (Oct. 2010), p. 66. DOI: 10.1088/0067-0049/191/1/66. URL: https://dx.doi.org/10.1088/0067-0049/191/1/66.

[16] L.-S. The et al. “Nuclear Reactions Governing the Nucleosynthesis of 44Ti”. In: *The Astrophysical Journal* 504.1 (Sept. 1998), p. 500. DOI: 10.1086/306057. URL: https://dx.doi.org/10.1086/306057.

[17] V. Margerin et al. “Study of the Ti44(α,p)V47 reaction and implications for core collapse supernovae”. In: *Physics Letters B* 731 (2014), pp. 358–361. ISSN: 0370-2693. DOI: https://doi.org/10.1016/j.physletb.2014.03.003. URL: https://www.sciencedirect.com/science/article/pii/S0370269314001580.

[18] T. Al-Abdullah et al. “The Feasibility of direct measurement of the 44Ti(α, p)47V and 40Ca(α, p)43Sc reactions in forward kinematics at astrophysically relevant temperatures”. In: *The European Physical Journal A* 50.9 (Sept. 2014), p. 140. ISSN: 1434-601X. DOI: 10.1140/epja/i2014-14140-8. URL: https://doi.org/10.1140/epja/i2014-14140-8.

[19] A. A. Sonzogni et al. “The 44Ti(α,p) Reaction and its Implication on the 44Ti Yield in Supernovae”. In: *Phys. Rev. Lett.* 84 (8 Feb. 2000), pp. 1651–1654. DOI: 10.1103/PhysRevLett.84.1651. URL: https://link.aps.org/doi/10.1103/PhysRevLett.84.1651.

[20] S. Starrfield, C. Iliadis, and W. R. Hix. “The Thermonuclear Runaway and the Classical Nova Outburst”. In: *Publications of the Astronomical Society of the Pacific* 128.963 (Apr. 2016), p. 051001. DOI: 10.1088/1538-3873/128/963/051001. URL: https://dx.doi.org/10.1088/1538-3873/128/963/051001.

[21] Keegan J. Kelly et al. “NUCLEAR MIXING METERS FOR CLASSICAL NOVAE”. In: *The Astrophysical Journal* 777.2 (Oct. 2013), p. 130. DOI: 10.1088/0004-637X/777/2/130. URL: https://dx.doi.org/10.1088/0004-637X/777/2/130.

[22] Jordi José et al. In: 612.1 (Sept. 2004), p. 414. DOI: 10.1086/422569. URL: https://dx.doi.org/10.1086/422569.

[23] Sachiko Amari et al. “Presolar Grains from Novae”. In: *The Astrophysical Journal* 551.2 (Apr. 2001), pp. 1065–1072. DOI: 10.1086/320235. URL: https://dx.doi.org/10.1086/320235.

[24] Jordi José, Alain Coc, and Margarita Hernanz. “Synthesis of Intermediate-Mass Elements in Classical Novae: From Si to Ca”. In: *The Astrophysical Journal* 560.2 (Oct. 2001), p. 897. DOI: 10.1086/322979. URL: https://dx.doi.org/10.1086/322979.

[25] Christian Iliadis et al. “The Effects of Thermonuclear Reaction-Rate Variations on Nova Nucleosynthesis: A Sensitivity Study”. In: *The Astrophysical Jour-*

nal Supplement Series 142.1 (Sept. 2002), p. 105. DOI: 10.1086/341400. URL: https://dx.doi.org/10.1086/341400.

[26] D. G. Jenkins et al. "Reevaluation of the ^{30}P(p,γ)^{31}S astrophysical reaction rate from a study of the $T = 1/2$ mirror nuclei, ^{31}S and ^{31}P". In: *Phys. Rev. C* 73 (6 June 2006), p. 065802. DOI: 10.1103/PhysRevC.73.065802. URL: https://link.aps.org/doi/10.1103/PhysRevC.73.065802.

[27] C. Wrede et al. "Measurements of ^{31}S energy levels and reevaluation of the thermonuclear resonant ^{30}P$(p,\gamma)^{31}$S reaction rate". In: *Phys. Rev. C* 79 (4 Apr. 2009), p. 045803. DOI: 10.1103/PhysRevC.79.045803. URL: https://link.aps.org/doi/10.1103/PhysRevC.79.045803.

[28] A. Parikh et al. "Improving the ^{30}P(p,γ)^{31}S rate in oxygen-neon novae: Constraints on J^{π} values for proton-threshold states in ^{31}S". In: *Phys. Rev. C* 83 (4 Apr. 2011), p. 045806. DOI: 10.1103/PhysRevC.83.045806. URL: https://link.aps.org/doi/10.1103/PhysRevC.83.045806.

[29] D. T. Doherty et al. "Key Resonances in the ^{30}P$(p,\gamma)^{31}$S Gateway Reaction for the Production of Heavy Elements in ONe Novae". In: *Phys. Rev. Lett.* 108 (26 June 2012), p. 262502. DOI: 10.1103/PhysRevLett.108.262502. URL: https://link.aps.org/doi/10.1103/PhysRevLett.108.262502.

[30] D. T. Doherty et al. "Level structure of ^{31}S: From low excitation energies to the region of interest for hydrogen burning in novae through the ^{30}P(p,γ)^{31}S reaction". In: *Phys. Rev. C* 89 (4 Apr. 2014), p. 045804. DOI: 10.1103/PhysRevC.89.045804. URL: https://link.aps.org/doi/10.1103/PhysRevC.89.045804.

[31] A. Kankainen et al. "Measurement of key resonance states for the P30(p,γ)S31 reaction rate, and the production of intermediate-mass elements in nova explosions". In: *Physics Letters B* 769 (2017), pp. 549–553. ISSN: 0370-2693. DOI: https://doi.org/10.1016/j.physletb.2017.01.084. URL: https://www.sciencedirect.com/science/article/pii/S0370269317301338.

[32] M. B. Bennett et al. "Detailed study of the decay ^{31}Cl$(\beta\gamma)^{31}$S". In: *Phys. Rev. C* 97 (6 June 2018), p. 065803. DOI: 10.1103/PhysRevC.97.065803. URL: https://link.aps.org/doi/10.1103/PhysRevC.97.065803.

[33] K. Setoodehnia et al. "Level structure of ^{31}S via ^{32}S$(p,d)^{31}$S". In: *Phys. Rev. C* 102 (4 Oct. 2020), p. 045806. DOI: 10.1103/PhysRevC.102.045806. URL: https://link.aps.org/doi/10.1103/PhysRevC.102.045806.

[34] T. Budner et al. "Constraining the ^{30}P(p, γ)^{31}S Reaction Rate in ONe Novae via the Weak, Low-Energy, β-Delayed Proton Decay of ^{31}Cl". In: *Phys. Rev. Lett.* 128 (18 May 2022), p. 182701. DOI: 10.1103/PhysRevLett.128.182701. URL: https://link.aps.org/doi/10.1103/PhysRevLett.128.182701.

[35] B. Alex Brown, W. A. Richter, and C. Wrede. "Shell-model studies of the astrophysical rapid-proton-capture reaction ^{30}P$(p,\gamma)^{31}$S". In: *Phys. Rev. C* 89 (6 June 2014), p. 062801. DOI: 10.1103/PhysRevC.89.062801. URL: https://link.aps.org/doi/10.1103/PhysRevC.89.062801.

[36] M. Bouhelal and F. Haas. "Shell-model study of 31S at excitations relevant to the thermonuclear 30P(p,γ)31S reaction rate". In: *The European Physical Journal Plus* 131.7 (July 2016), p. 226. ISSN: 2190-5444. DOI: 10.1140/epjp/i2016-16226-0. URL: https://doi.org/10.1140/epjp/i2016-16226-0.

[37] M. B. Bennett et al. "Isospin Mixing Reveals ^{30}P$(p,\gamma)^{31}$S Resonance Influencing Nova Nucleosynthesis". In: *Phys. Rev. Lett.* 116 (10 Mar. 2016), p. 102502. DOI: 10.1103/PhysRevLett.116.102502. URL: https://link.aps.org/doi/10.1103/PhysRevLett.116.102502.

[38] Margarita Hernanz et al. "Gamma-Ray Emission from Novae Related to Positron Annihilation: Constraints on its Observability Posed by New Experimental Nuclear Data". In: *The Astrophysical Journal* 526.2 (Oct. 1999), p. L97. DOI: 10.1086/312372. URL: https://dx.doi.org/10.1086/312372.

[39] M. Hernanz and J. José. "γ-rays from classical novae: expectations from present and future missions". In: *New Astronomy Reviews* 48.1 (2004). Astronomy with Radioactivities IV and Filling the Sensitivity Gap in MeV Astronomy, pp. 35–39. ISSN: 1387-6473. DOI: https://doi.org/10.1016/j.newar.2003.11.005. URL: https://www.sciencedirect.com/science/article/pii/S1387647303002665.

[40] Kahl, D., José, J., and Woods, P. J. "Uncertainties in the 18F(p,a)15O reaction rate in classical novae". In: *A&A* 653 (2021), A64. DOI: 10.1051/0004-6361/202140339. URL: https://doi.org/10.1051/0004-6361/202140339.

[41] D. Kahl et al. "s-wave resonances for the 18F(p,α)15O reaction in novae". In: *The European Physical Journal A* 55.1 (Jan. 2019), p. 4. DOI: 10.1140/epja/i2019-12682-9. URL: https://doi.org/10.1140/epja/i2019-12682-9.

[42] D.W. Bardayan et al. “Destruction of 18F via 18F(p,α) 15O burning through the Ec.m.=665 keV resonance”. In: *Physical Review C - Nuclear Physics* 63 (June 2001), pp. 658021–658026.

[43] D. Bardayan et al. “Strength of the 18F(p,α)15O Resonance at Ec.m.=330 keV”. In: *Physical Review Letters* 89 (Dec. 2002). DOI: 10.1103/PhysRevLett.89.262501.

[44] C. E. Beer et al. “Direct measurement of the 18F(p,α)15O reaction at nova temperatures”. English. In: *Physical Review C* 83.4 (Apr. 2011). ISSN: 2469-9985. DOI: 10.1103/PhysRevC.83.042801.

[45] D. J. Mountford et al. “Resonances in ^{19}Ne with relevance to the astrophysically important ^{18}F(p,α)^{15}O reaction”. In: *Phys. Rev. C* 85 (2 Feb. 2012), p. 022801. DOI: 10.1103/PhysRevC.85.022801. URL: https://link.aps.org/doi/10.1103/PhysRevC.85.022801.

[46] M. Hall et al. “Key ^{19}Ne states identified affecting γ-ray emission from ^{18}F in novae”. In: (Jan. 2019).

[47] J. E. Riley et al. “Sub-threshold states in ^{19}Ne relevant to ^{18}F$(p,\alpha)^{15}$O”. In: *Phys. Rev. C* 103 (1 Jan. 2021), p. 015807. DOI: 10.1103/PhysRevC.103.015807. URL: https://link.aps.org/doi/10.1103/PhysRevC.103.015807.

[48] D. Torresi et al. “Evidence for $^{15}\mathrm{O} + \alpha$ resonance structures in ^{19}Ne via direct measurement”. In: *Phys. Rev. C* 96 (4 Oct. 2017), p. 044317. DOI: 10.1103/PhysRevC.96.044317. URL: https://link.aps.org/doi/10.1103/PhysRevC.96.044317.

[49] J. C. Dalouzy et al. “Discovery of a New Broad Resonance in ^{19}Ne: Implications for the Destruction of the Cosmic γ-Ray Emitter ^{18}**F**”. In: *Phys. Rev. Lett.* 102 (16 Apr. 2009), p. 162503. DOI: 10.1103/PhysRevLett.102.162503. URL: https://link.aps.org/doi/10.1103/PhysRevLett.102.162503.

[50] J.B Marion and F.C Young. *Nuclear Reaction Analysis*. North-Holland Publishing Company, 1968.

[51] D W Bardayan. “Transfer reactions in nuclear astrophysics”. In: *Journal of Physics G: Nuclear and Particle Physics* 43.4 (Feb. 2016), p. 043001. DOI: 10.1088/0954-3899/43/4/043001. URL: https://dx.doi.org/10.1088/0954-3899/43/4/043001.

[52] Ian J. Thompson and Filomena M. Nunes. *Nuclear Reactions for Astrophysics: Principles, Calculation and Applications of Low-Energy Reactions*. Cambridge University Press, 2009. DOI: 10.1017/CBO9781139152150.

[53] GSI Helmholzzentrum fur scherionforschung GmbH. *[Image]*. Accessed 10/2022. URL: gsi.de/en/researchaccelerators/accelerator_facility.

[54] Jörg Eichler and Thomas Stöhlker. "Radiative electron capture in relativistic ion–atom collisions and the photoelectric effect in hydrogen-like high-Z systems". In: *Physics Reports* 439.1 (2007), pp. 1–99. ISSN: 0370-1573. DOI: https://doi.org/10.1016/j.physrep.2006.11.003. URL: https://www.sciencedirect.com/science/article/pii/S037015730600442X.

[55] Markus Steck and Yuri A. Litvinov. "Heavy-ion storage rings and their use in precision experiments with highly charged ions". In: *Progress in Particle and Nuclear Physics* 115 (2020), p. 103811. ISSN: 0146-6410. DOI: https://doi.org/10.1016/j.ppnp.2020.103811. URL: https://www.sciencedirect.com/science/article/pii/S0146641020300582.

[56] M. Lestinsky et al. "Physics book: CRYRING@ESR". In: *European Physical Journal Special Topics* 225.5 (Sept. 2016). DOI: 10.1140/epjst/e2016-02643-6.

[57] M. Grieser et al. "Storage ring at HIE-ISOLDE. Technical design report". In: *European Physical Journal Special Topics* 207 (May 2012), pp. 1–117. DOI: 10.1140/epjst/e2012-01599-9.

[58] David J. Morrissey and Brad M. Sherrill. "In-Flight Separation of Projectile Fragments". In: *The Euroschool Lectures on Physics with Exotic Beams, Vol. I*. Ed. by Jim Al-Khalili and Ernst Roeckl. Berlin, Heidelberg: Springer Berlin Heidelberg, 2004, pp. 113–135. ISBN: 978-3-540-44490-9. DOI: 10.1007/978-3-540-44490-9_4. URL: https://doi.org/10.1007/978-3-540-44490-9_4.

[59] V.P. Shevelko et al. "Lifetimes of relativistic heavy-ion beams in the High Energy Storage Ring of FAIR". In: *Nuclear Instruments and Methods in Physics Research Section B: Beam Interactions with Materials and Atoms* 421 (2018), pp. 45–49. ISSN: 0168-583X. DOI: https://doi.org/10.1016/j.nimb.2018.02.012. URL: https://www.sciencedirect.com/science/article/pii/S0168583X1830096X.

[60] A. S. Schlachter et al. “Electron capture for fast highly charged ions in gas targets: An empirical scaling rule”. In: *Phys. Rev. A* 27 (6 June 1983), pp. 3372–3374. DOI: 10.1103/PhysRevA.27.3372. URL: https://link.aps.org/doi/10.1103/PhysRevA.27.3372.

[61] H. J. Assenbaum, K. Langanke, and C. Rolfs. “Effects of electron screening on low-energy fusion cross sections”. In: *Zeitschrift für Physik A Atomic Nuclei* 327.4 (Dec. 1987), pp. 461–468. ISSN: 0939-7922. DOI: 10.1007/BF01289572. URL: https://doi.org/10.1007/BF01289572.

[62] J. Glorius et al. “Approaching the Gamow Window with Stored Ions: Direct Measurement of ^{124}Xe(p,γ) in the ESR Storage Ring”. In: *Phys. Rev. Lett.* 122 (9 Mar. 2019), p. 092701. DOI: 10.1103/PhysRevLett.122.092701. URL: https://link.aps.org/doi/10.1103/PhysRevLett.122.092701.

[63] Helmut Poth. “Electron cooling: Theory, experiment, application”. In: *Physics Reports* 196.3 (1990), pp. 135–297. ISSN: 0370-1573. DOI: https://doi.org/10.1016/0370-1573(90)90040-9. URL: https://www.sciencedirect.com/science/article/pii/0370157390900409.

[64] Vsevolod Kamerdzheiv. *Introduction to electron cooling [Image]*. 2015. URL: indico.cern.ch/event/357886/contributions/849347/attachments/1148562/1647628/EC.pdf.

[65] V.Baglin. *Vacuum systems lecture 2*. 2018. URL: https://indico.cern.ch/event/683638/contributions/2801664/attachments/1563481/2536247/Lecture_2_Vacuum_Systems_-_V_Baglin_-_JUAS_2018_-_13_feb_2018_with_complementary_info_.pdf.

[66] Karl Jousten and C. Benjamin Nakhosteen. *Handbook of Vacuum Technology*. 2nd. John Wiley and Sons Incorporated, 2016.

[67] J.M Lafferty. *Foundations of Vacuum Science and Technology*. John Wiley and Sons Incorporated, 1998. ISBN: 9780471175933.

[68] John. F O’Hanlon. *A User’s Guide to Vacuum Technology*. 3rd. John Wiley and Sons Incorporated, 2003.

[69] Y Blumenfeld, T Nilsson, and P Van Duppen. “Facilities and methods for radioactive ion beam production”. In: *Physica Scripta* 2013.T152 (Jan. 2013), p. 014023. DOI: 10.1088/0031-8949/2013/T152/014023. URL: https://dx.doi.org/10.1088/0031-8949/2013/T152/014023.

[70] P. Van Duppen. "Isotope Separation On Line and Post Acceleration". In: *The Euroschool Lectures on Physics with Exotic Beams, Vol. II*. Ed. by Jim Al-Khalili and Ernst Roeckl. Berlin, Heidelberg: Springer Berlin Heidelberg, 2006, pp. 37–77. ISBN: 978-3-540-33787-4. DOI: 10.1007/3-540-33787-3_2. URL: https://doi.org/10.1007/3-540-33787-3_2.

[71] H. Moeini et al. "First feasibility experiment for the EXL project with prototype detectors at the ESR storage ring". In: *Nuclear Instruments and Methods in Physics Research Section A: Accelerators, Spectrometers, Detectors and Associated Equipment* 634.1 (2011), pp. 77–84. ISSN: 0168-9002. DOI: https://doi.org/10.1016/j.nima.2011.01.036. URL: https://www.sciencedirect.com/science/article/pii/S0168900211000878.

[72] M. Mutterer et al. "Experimental techniques for in-ring reaction experiments". In: *Physica Scripta* 2015.T166 (2015). DOI: 10.1088/0031-8949/2015/T166/014053. URL: https://iopscience.iop.org/article/10.1088/0031-8949/2015/T166/014053.

[73] M von Schmid et al. "Investigation of the nuclear matter distribution of ^{56}Ni by elastic proton scattering in inverse kinematics". In: *Physica Scripta* T166 (Nov. 2015), p. 014005. DOI: 10.1088/0031-8949/2015/t166/014005. URL: https://doi.org/10.1088/0031-8949/2015/t166/014005.

[74] M. von Schmid et al. "Matter radius of the doubly-magic ^{56}Ni measured in a storage ring". In: *The European Physical Journal A* 59.4 (Apr. 2023), p. 83. ISSN: 1434-601X. DOI: 10.1140/epja/s10050-023-00967-z. URL: https://doi.org/10.1140/epja/s10050-023-00967-z.

[75] J.C. Zamora et al. "First measurement of isoscalar giant resonances in a stored-beam experiment". In: *Physics Letters B* 763 (2016), pp. 16–19. ISSN: 0370-2693. DOI: https://doi.org/10.1016/j.physletb.2016.10.015. URL: https://www.sciencedirect.com/science/article/pii/S037026931630586X.

[76] J. C. Zamora et al. "Nuclear-matter radius studies from ^{58}Ni(α,α) experiments at the GSI Experimental Storage Ring with the EXL facility". In: *Phys. Rev. C* 96 (3 Sept. 2017), p. 034617. DOI: 10.1103/PhysRevC.96.034617. URL: https://link.aps.org/doi/10.1103/PhysRevC.96.034617.

[77] K. Yue et al. "Measurement of ^{58}Ni$(p,p)^{58}$Ni elastic scattering at low momentum transfer by using the HIRFL-CSR heavy-ion storage ring". In: *Phys. Rev. C* 100

(5 Nov. 2019), p. 054609. DOI: 10.1103/PhysRevC.100.054609. URL: https://link.aps.org/doi/10.1103/PhysRevC.100.054609.

[78] Bo Mei et al. "First measurement of the ^{96}Ru$(p,\gamma)^{97}$Rh cross section for the p process with a storage ring". In: *Phys. Rev. C* 92 (3 Sept. 2015), p. 035803. DOI: 10.1103/PhysRevC.92.035803. URL: https://link.aps.org/doi/10.1103/PhysRevC.92.035803.

[79] "Proton capture on stored radioactive ^{118}Te ions". In: *Proceedings of Nuclear Physics in Astrophysicss X* (Geneva, Switzerland). Submitted. Geneva, Switzerland: epj web of conferences, 2022.

[80] DT Doherty et al. "Nuclear transfer reaction measurements at the ESR—for the investigation of the astrophysical 15O (α, γ) 19Ne reaction". In: *Physica Scripta* 2015.T166 (2015), p. 014007.

[81] A. Gruber et al. "Internal gas-jet target for the ESR at GSI". In: *Nuclear Instruments and Methods in Physics Research Section A: Accelerators, Spectrometers, Detectors and Associated Equipment* 282.1 (1989), pp. 87–93. ISSN: 0168-9002. DOI: https://doi.org/10.1016/0168-9002(89)90114-9. URL: https://www.sciencedirect.com/science/article/pii/0168900289901149.

[82] Carlo Giulio Bruno et al. "For the Design, Construction and Commissioning of an In-ring Spectrometer for Nuclear Reaction Studies at CRYRING". In: 2018. URL: https://www.semanticscholar.org/paper/For-the-Design$%5C%$2C-Construction-and-Commissioning-of-Bruno-Davinson/9d57e0c7851ac2b7cd55fdfa401d5

[83] Davide Braga et al. "AIDA: A 16-channel amplifier ASIC to read out the Advanced Implantation Detector Array for experiments in nuclear decay spectroscopy". In: *2011 2nd International Conference on Advancements in Nuclear Instrumentation, Measurement Methods and their Applications*. 2011, pp. 1–5. DOI: 10.1109/ANIMMA.2011.6172853.

[84] O. Hall et al. "The Advanced Implantation Detector Array (AIDA)". In: *Nuclear Instruments and Methods in Physics Research Section A: Accelerators, Spectrometers, Detectors and Associated Equipment* (2023), p. 168166. ISSN: 0168-9002. DOI: https://doi.org/10.1016/j.nima.2023.168166. URL: https://www.sciencedirect.com/science/article/pii/S0168900223001560.

[85] O.Hall. "PhD Thesis". 2020.

[86] V. F. E. Pucknell and *et al.* Accessed 11/2022. URL: http://npg.dl.ac.uk/MIDAS/.

[87] H.T. Schmidt et al. "A design study for an internal gas-jet target for the heavy-ion storage ring CRYRING". In: *Hyperfine Interactions* 108 (June 1997), pp. 339–354. DOI: 10.1023/A:1012635418262.

[88] N.Petridis. "PhD Thesis". 2014.

[89] A. Täschner et al. "Determination of hydrogen cluster velocities and comparison with numerical calculations". In: *The Journal of Chemical Physics* 139.23 (2013), p. 234312. DOI: 10.1063/1.4848720. eprint: https://doi.org/10.1063/1.4848720. URL: https://doi.org/10.1063/1.4848720.

[90] N.Petridis et al. *Technical design report: The CRYRING internal jet target*. 2018. URL: https://edms.cern.ch/ui/file/2059586/1/The_CRYRING_Internal_Jet_Target__submitted_2018-02-23__-_public_2018-11-01.pdf.

[91] R. J. Reid. *Vacuum Systems, Procedures for cleaning of vacuum items*. 2003. URL: https://www2.ph.ed.ac.uk/~td/isol-srs/spc-003-Cleaning%20of%20Vacuum%20Items.pdf.

[92] V. Hauer K. Battes C. Day. "Outgassing behavior of different high-temperature resistant polymers". In: *Journal of Vacuum Science & Technology A: Vacuum, Surfaces and Films* 36 (2018). DOI: https://doi.org/10.1116/1.5001243.

[93] R.N Peacock. "Practical selection of elastomer materials for vacuum seals". In: *Journal of Vacuum Science & Technology* 17 (1980). DOI: https://doi.org/10.1116/1.570380.

[94] D Möhl. "Sources of emittance growth". In: (2006). DOI: 10.5170/CERN-2006-002.245. URL: https://cds.cern.ch/record/941314.

[95] National Nuclear Data Center. Accessed 10/2022. URL: https://www.nndc.bnl.gov/nudat3/.

[96] Toshiyuki Ishimatsu. "The N14(d, a)C12 Ground-State Reaction in the Energy Range of Deuteron from 1.5 to 3.0 MeV". In: *Journal of the Physical Society of Japan* 16.8 (1961), pp. 1529–1538. DOI: 10.1143/JPSJ.16.1529. eprint: https://doi.org/10.1143/JPSJ.16.1529. URL: https://doi.org/10.1143/JPSJ.16.1529.

[97] V. Gomes Porto et al. "Deuteron induced reactions on 14N". In: *Nuclear Physics A* 136.2 (1969), pp. 385–413. ISSN: 0375-9474. DOI: https://doi.org/10.1016/

0375-9474(69)90060-8. URL: https://www.sciencedirect.com/science/article/pii/0375947469900608.

[98] N.A. Mansour et al. "Studies of the (d, a) reaction on N14 in the deuteron energy range from 1 to 2.5 MeV". In: *Nuclear Physics* 59.2 (1964), pp. 241–252. ISSN: 0029-5582. DOI: https://doi.org/10.1016/0029-5582(64)90081-1. URL: https://www.sciencedirect.com/science/article/pii/0029558264900811.

[99] A. Gallmann, P. Fintz, and P.E. Hodgson. "Réactions (d, p) sur 11B, 12C, 14N et 16O à Ed ≤ 5.5 MeV". In: *Nuclear Physics* 82.1 (1966), pp. 161–181. ISSN: 0029-5582. DOI: https://doi.org/10.1016/0029-5582(66)90529-3. URL: https://www.sciencedirect.com/science/article/pii/0029558266905293.

[100] H. Beaumevieille et al. "Study of the 14N(d, d)14N and 14N(d, p)15N angular distributions and excited states of 15N". In: *Nuclear Physics* 125 (1969), pp. 568–584.

[101] A. Valek et al. "A study of the 14N(d, p)15N reaction at low bombarding energies". In: *Nuclear Physics A* 270.1 (1976), pp. 200–210. ISSN: 0375-9474. DOI: https://doi.org/10.1016/0375-9474(76)90135-4. URL: https://www.sciencedirect.com/science/article/pii/0375947476901354.

[102] G. W. Phillips and W. W. Jacobs. "Structure of ^{15}N and the ^{14}N$(d,p)^{15}$N Reaction". In: *Phys. Rev.* 184 (4 Aug. 1969), pp. 1052–1060. DOI: 10.1103/PhysRev.184.1052. URL: https://link.aps.org/doi/10.1103/PhysRev.184.1052.

[103] M. H. Macfarlane and J. B. French. "Stripping Reactions and the Structure of Light and Intermediate Nuclei". In: *Rev. Mod. Phys.* 32 (3 July 1960), pp. 567–691. DOI: 10.1103/RevModPhys.32.567. URL: https://link.aps.org/doi/10.1103/RevModPhys.32.567.

[104] Ian Thompson. *Fresco*. Accessed 05/2023. URL: http://www.fresco.org.uk/.

[105] Roderick V Reid. "Local phenomenological nucleon-nucleon potentials". In: *Annals of Physics* 50.3 (1968), pp. 411–448. ISSN: 0003-4916. DOI: https://doi.org/10.1016/0003-4916(68)90126-7. URL: https://www.sciencedirect.com/science/article/pii/0003491668901267.

[106] Reference input parameter library. Accessed 05/2023. URL: https://www-nds.iaea.org/RIPL-3/.

[107] Haixia An and Chonghai Cai. “Global deuteron optical model potential for the energy range up to 183 MeV”. In: *Phys. Rev. C* 73 (5 May 2006), p. 054605. DOI: 10.1103/PhysRevC.73.054605. URL: https://link.aps.org/doi/10.1103/PhysRevC.73.054605.

[108] J. J. H. Menet et al. “Total-Reaction-Cross-Section Measurements for 30-60-MeV Protons and the Imaginary Optical Potential”. In: *Phys. Rev. C* 4 (4 Aug. 1971), pp. 1114–1129. DOI: 10.1103/PhysRevC.4.1114. URL: https://link.aps.org/doi/10.1103/PhysRevC.4.1114.

[109] M. B. Chadwick et al. “Calculation and Evaluation of Cross Sections and Kerma Factors for Neutrons up to 100 MeV on Carbon”. In: *Nuclear Science and Engineering* 123.1 (1996), pp. 17–37. DOI: 10.13182/NSE96-A24210. URL: https://doi.org/10.13182/NSE96-A24210.

[110] D.G. Madland. In: *OECD/NEA Spec Mtg* (1997), p. 129.

[111] Barakat Al-Bataina and Joachim Jänecke. “Alpha-particle emission from contaminants in counter materials”. In: *Nuclear Instruments and Methods in Physics Research Section A: Accelerators, Spectrometers, Detectors and Associated Equipment* 255.3 (1987), pp. 512–517. ISSN: 0168-9002. DOI: https://doi.org/10.1016/0168-9002(87)91220-4. URL: https://www.sciencedirect.com/science/article/pii/0168900287912204.